

Pt/Pt Alloy and Manganese Dioxides Based Oxygen Reduction Reaction Catalysts for

Low-Temperature Fuel Cells

by

Xuan Shi

A Dissertation Presented in Partial Fulfillment
of the Requirements for the Degree
Doctor of Philosophy

Approved July 2019 by the
Graduate Supervisory Committee:

Arunachalanadar Mada Kannan, Chair
Jingyue Liu
Changho Nam
Xihong Peng

ARIZONA STATE UNIVERSITY

August 2019

ABSTRACT

The fuel cell is a promising device that converts the chemical energy directly into the electrical energy without combustion process. However, the slow reaction rate of the oxygen reduction reaction (ORR) necessitates the development of cathode catalysts for low-temperature fuel cells. After a thorough literature review in Chapter 1, the thesis is divided into three parts as given below in Chapters 2-4.

Chapter 2 describes the study on the Pt and Pt-Me (Me: Co, Ni) alloy nanoparticles supported on the pyrolyzed zeolitic imidazolate framework (ZIF) towards ORR. The Co-ZIF and NiCo-ZIF were synthesized by the solvothermal method and then mixed with Pt precursor. After pyrolysis and acid leaching, the PtCo/NC and PtNiCo/NC were evaluated in proton exchange membrane fuel cells (PEMFC). The peak power density exhibited > 10% and 15% for PtCo/NC and PtNiCo/NC, respectively, compared to that with commercial Pt/C catalyst under identical test conditions.

Chapter 3 is the investigation of the oxygen vacancy (OV) effect in α -MnO₂ as a cathode catalyst for alkaline membrane fuel cells (AMFC). The α -MnO₂ nanorods were synthesized by hydrothermal method and heated at 300, 400 and 500 °C in the air to introduce the OV. The 400 °C treated material showed the best ORR performance among all other samples due to more OV in pure α -MnO₂ phase. The optimized AMFC electrode showed ~ 45 mW.cm⁻², which was slightly lower than that with commercial Pt/C (~60 mW.cm⁻²).

Chapter 4 is the density functional theory (DFT) study of the protonation effect and active sites towards ORR on α -MnO₂ (211) plane. The theoretically optimized oxygen adsorption and hydroxyl ion desorption energies were ~ 1.55 - 1.95 eV and ~ 0.98 - 1.45 eV, respectively, by Nørskov et al.'s calculations. All the configurations showed oxygen adsorption and hydroxyl ion desorption energies were ranging from 0.27 to 1.76 eV and 1.59 to 15.0 eV, respectively. The site which was close to two Mn ions showed the best oxygen adsorption and hydroxyl ion desorption energies improvement with the surface protonation.

Based on the results given in Chapters 1-4, the major findings are summarized in Chapter 5.

DEDICATION

To my mother Yan and father Junhui.

ACKNOWLEDGMENTS

I would like to thank my thesis advisor Prof. Kannan, who helped me start my research career towards the fuel cell cathode catalyst. In 2016, I joined his lab with no background in chemistry; and he patiently guided me step by step and trained me systematically in the experiment section. When some problem troubled me, he always encouraged me by saying, “Don’t worry, you will understand it.” His optimistic personality totally influenced my Ph.D. life, makes me more confident, so that I never give in to the troubles. Also, thanks to Dr. Nam, his engineering and MATLAB optimization class reinforced my mathematical background and gave me more perspectives to do my research. I would also thank Dr. Liu, who helped with quantum mechanics and opened the door for the material simulation. In addition, I have a special appreciation for Dr. Peng, who gave me the opportunity of starting my density functional theory (DFT) calculations for the fuel cell catalyst. She patiently answered my endless questions, even the most fundamental ones. At last, thanks to Dr. Zheng, for the help in doing research at the Council for Scientific and Industrial Research (CSIR) in South Africa. Then to my girlfriend Kehila, who has the same research goal: to make fuel cell work well. Pursuing a Ph.D. has been hard, but she is the best company to make the journey beautiful.

Also, I would like to thank my collaborators (Dr. Iqbal, Harshal, Salman, Gul, Noaman, Wasim, Kahlid, Abid, Saadia, Rehan, Kehila, Shahbaz, Afaf, Sheeraz and Grigoria) and my lab mates (Pavan, Umesh, Dr. Jyoti and Daryn) for the help and insightful discussions. Finally, I would like to thank USAID (US-Pakistan Centers for Advanced Studies), CSIR and USAID (Global Development Research) for the financial support. We acknowledge

the use of facilities within the Eyring Materials Center and High-performance Research Computing at Arizona State University, and the equipment at LANNBIO Cinvestav Mérida, Mexico.

TABLE OF CONTENTS

	Page
LIST OF TABLES	xi
LIST OF FIGURES	xii
CHAPTER	
1 INTRODUCTION	1
1.1 Background	1
1.2 The ORR Catalysts Based on Pt.....	10
1.3 The ORR Catalyst Based non-PGM Materials in Alkaline and Acidic Media ...	14
1.3.1 The ORR Catalyst Based on Manganese Oxides in Alkaline media.....	14
1.3.2 The ORR Catalyst Based on Me Supported on Nitrogen-doped Carbon (Me/NC) in Acidic media	17
1.4 The First Principles Theoretic Calculation with the Vienna Ab Initio Simulation Package (VASP).....	19
1.5 Objectives	22
1.5.1 Objective 1.....	23
1.5.2 Objective 2.....	24
1.5.3 Objective 3.....	24
1.6 Structure of the Dissertation	25
2 PLATINUM COBALT ALLOY AND PLATINUM NICKEL-COBALT ALLOY SUPPORTED ON THE NITROGEN DOPED CARBON DERIVED FROM COBALT-ZIF AND NICKEL COBALT-ZIF TOWARDS ORR IN PEMFC.....	26
2.1 Introduction	26

CHAPTER	Page
2.2 Experimental Section.....	27
2.2.1 Synthesis of Co-ZIF and NiCo-ZIF Particles	27
2.2.2 Synthesis of PtCo/NC and PtNiCo/NC	28
2.2.3 Catalyst Characterization and Analysis	28
2.2.4 Thin Film Rotating Disk Electrode and Electrochemical Evaluation	29
2.2.5 Catalyst Coated Membranes	32
2.2.6 Gas Diffusion Layer	34
2.3 Discussion for PtCo/NC	38
2.4 Discussion for PtNiCo/NC	44
2.5 Conclusion.....	59
 3 THERMAL INDUCED OV IN ALPHA MANGANESE DIOXIDE TOWARDS ORR IN ALKALINE MEDIA AND ALKALINE MEMBRANE FUEL CELL	 62
3.1 Introduction	62
3.2 Experimental.....	64
3.2.1 α -MnO ₂ Preparation	64
3.2.2 Electrode Preparation and Testing.....	65
3.2.3 Materials Characterization.....	66
3.2.4 Catalyst Coated Membranes	67
3.2.5 Gas diffusion layer.....	69
3.3 Discussion for OV in α -MnO ₂	70
3.4 Discussion for α -MnO ₂ Cathode in Alkaline Membrane Fuel Cell	85
3.5 Conclusion.....	92

CHAPTER	Page
4	FIRST PRINCIPLES STUDY OF THE PROTONATION EFFECT AND ACTIVE SITES TOWARDS OXYGEN REDUCTION REACTION ON ALPHA MANGANESE DIOXIDES (211) PLANE 95
	4.1 Introduction 95
	4.2 Simulation and Experiment Details..... 96
	4.3 Results and Discussion 100
	4.4 Conclusion..... 105
5	CONCLUSION 106
	REFERENCES 110
APPENDIX	
A	EXCEL VBA CODE FOR CORRECT LSV OXYGEN DATA WITH NITROGEN CURRENT ALONG WITH ELECTRODE NORMALIZATION TO RHE..... 123
B	EXCEL VBA CODE FOR CALCULATING CHARGE TRANSFER NUMBER 130
C	EXCEL VBA CODE FOR ORGANIZING FUEL CELL DATA FOR PLOTTING 137
D	EXCEL VBA CODE FOR CALCULATING LATTICE PARAMETER FROM XRD DATA 140
E	EXCEL VBA CODE FOR CONVERSION DIFFRACTION ANGLE BETWEEN CO AND CU X-RAY SOURCE..... 144

F	EXCEL VBA CODE FOR CALCULATING THE ALLOY COMPOSITION BY VEGARD'S LAW FROM XRD DATA	147
G	EXCEL VBA CODE FOR CALCULATING THE SCHERRER CRYSTALLITE SIZE FROM XRD DATA.....	150
H	EXCEL VBA CODE FOR MODIFYING POSCAR FOR DFT SELECTIVE DYNAMICS CALCULATIONS	153
I	PYTHON CODE FOR BAND STRUCTURE INFORMATION FROM EIGENVAL WITH SPIN-POLARIZED CALCULATION.....	156
J	PYTHON CODE FOR EXTRACT THE PROJECTED DENSITY OF STATES FROM THE DOSCAR FILE	161

LIST OF TABLES

Table		Page
1.	The Cost of PEMFC System for L/MDV Application in 2016, 2017 and 2018. The Price Estimations Are Based on 500,000 Units of 100 kW System Per Year [17]	8
2.	The Catalyst Specifications in 80 Kw Fuel Cell System in the Current Auto System and the Target in 2020 and 2025 [17]	9
3.	The Diffraction Peaks Positions, Lattice Spacings, Pt:(Ni/Co) Ratios and Particle Sizes of Pt, Co, Ni, PtCo and PtNiCo.	46
4.	Composition (Atomic %) of Elements in the PtNiCo/NC, Estimated from the Deconvoluted Components in XPS Data.	50
5.	Comparison of Different as Prepared Samples and Commercial Pt/C Used as Electrocatalysts for ORR in Acidic Medium.	56
6.	Comparison of Different Pt Based Electrocatalysts for ORR (1600 RPM, 0.1M HClO ₄).....	57
7.	Catalyst Coated Membrane Sample Specifications.....	67
8.	List of Intensity Ratios of O/Mn and Mn L ₃ /L ₂ In All α -MnO ₂ Samples.....	77
9.	Catalyst Coated Membrane Sample With Power and Impedance Specifications	92

LIST OF FIGURES

Figure		Page
1.	The World Energy Demand and Prediction for 2017 and 2040, Respectively [4].	2
2.	Components of a PEMFC.	5
3.	The Structure of a Sulphonated Fluoroethylene [13].	7
4.	Possible ORR Pathway on Pt (111) Surface [19].	11
5.	(A) The ORR Activities Vs. Oxygen Adsorption Energies and (B) Vs. Oxygen Adsorption and Hydroxyl Ion Desorption Energies [22].	11
6.	Schematic Illustration of Different Shapes of Pt Nanocrystals Derived from Conventional Single-Crystal Polyhedron. The Yellow and Blue Colors Represent the (100) and (111) Facets, Respectively [25].	13
7.	The Flowchart of Calculation Through the Kohn-Sham DFT Method.	21
8.	Polished RDE Working Electrode.	31
9.	Ink Restricted on the GC Electrode.	31
10.	Thin Film on RDE.	32
11.	Exactacoat Machine.	33
12.	PEMFC MEA on Nafion 212 Membrane.	34
13.	(A) Carbon Paper (B) The Carbon in Water Without SDS (Top View) (C) the Carbon in Water Without SDS (Side View) (D) Adding SDS and (E) the Carbon Suspended in Water.	35

Figure	Page
14. Schematic Representation of Isolating Carbon Bundle by Ultrasonication. (A) Carbon Bundle, (B) Single Carbon Unit Separated by Sonication, (C) Surfactant Adsorption on Isolated Carbon Unit, (D) Dispersed Carbon Unit with Help of Surfactant, and the Possible Way of Carbon-Surfactant Interactions: (E) Cylindrical Micelles, (F) Hemimicelles and (G) Random Adsorption.....	36
15. EC26 Coatema Machine with the Carbon Slurry Coated Carbon Paper.	37
16. GDL with Water Droplets Demonstrating Its Hydrophobic Characteristics.	37
17. SEM of (A) and (B) ZIF-67 at Two Different Magnifications, (C) Co/NC and (D) PtCo/NC.....	38
18. Transmission Electron Micrographs for (A) Co/NC, (B) PtCo/NC and (C) EDS for PtCo/NC Shown in (B).	39
19. X-Ray Diffractograms of (A) Co/NC and (B) PtCo/NC.	40
20. RDE Data HClO ₄ Electrolyte At 23 °C For (A) Co/NC, (B) PtCo/NC at 1600 RPM, (C) Commercial Pt/C at 1600 RPM, (D) PtCo/NC at Various RPM, (E) Koutecký–Levich (KL) Plot for PtCo/NC at Various Potentials with Inset Shown the Number of Electron Change and (F) CV Data for PtCo/NC and Commercial Pt/C at 400 RPM.....	41
21. Fuel Cell Performance of (A) PtCo/NC and (B) Commercial Pt/C Cathode Catalysts at Various Temperatures with H ₂ and O ₂ Gases, 100 % RH at Ambient Pressure. The Open Symbols Represent the Power Density Values.	43

Figure	Page
22. XRD of (A) Co ZIF (Red) and NiCo ZIF (Blue) Along with a Simulated Pattern for Co ZIF (Black), (B) NiCo/NC and PtNiCo/NC, and (C) High-Resolution XRD Looping Scan for Pt, Ni, Co (111) Regions.....	44
23. Morphology and Structural Characterization in FESEM. (A) Co-ZIF, (B) Nico-ZIF, (C) NiCo/Ncand (D) PtNiCo/NC.....	47
24. (A) The HAADF Image of NiCo-ZIF, (B) EDS Mapping of the Selected Area from (A), (C) EDS Signal of the Selected Area from (A) and (C), and (D), (E), (F) TEM Images of PtNiCo at Various Magnifications.....	48
25. (A) The Wide Scan of XPS Data and the Deconvoluted High-Resolution XPS Scan of (B) C1s, (C) N1s, (D) O1s, (E) Co2p and (F) Pt4f For PtNiCo/NC.	51
26. Comparison of Pt4f Spectra of PtNiCo/NC and Pt/C From XPS	52
27. Electrochemical Performance of (A) CV Plots in N ₂ (Red) and O ₂ (Black) Saturated Electrolyte; (B) LSV for Co/NC (Red Dash), NiCo/NC (Black Dash), PtCo/NC (Black Solid), NiCo/NC (Red Solid) and Pt/C (Blue Solid) at 1600 RPM in O ₂ Saturated Electrolyte; (C) LSV for PtNiCo/NC at Different RPM in O ₂ Saturated Electrolyte; (D) The Charge Transfer Numbers For PtNiCo/NC (Blue) and Pt/C (Red) and K-L Plots for PtNiCo/NC at Different Potential (Inset); (E) LSV For Ptnico/NC Before and After Durability Test at 1600 RPM in O ₂ Saturated Electrolyte; (F) LSV for Pt/C Before and After Durability Test at 1600 RPM in O ₂ Saturated Electrolyte. All the Electrolytes Were 0.1 M HClO ₄	55

Figure	Page
28. The PEMFC Performance of (A) Nafion/Catalyst Ratio Optimization for PtNiCo/NC, (B) MEAs With NiCo/NC, PtNiCo/NC and Pt/C with and Without Back Pressure, and (C) The Stability Testing with PtNiCo/NC Cathode at Ambient Pressure (All the Data Were Obtained at 70 °C Using H ₂ and O ₂ at 200 and 300 SCCM at 100 % RH with Nafion-212 Electrolyte).	58
29. Oxygen at Different Sites of AMFC Cathode α -MnO ₂ /C Layer, (A) Ionomer and Catalyst Boundary, (B) Ionomer and Carbon Support Boundary, (C) Catalyst and Carbon Support Boundary (D) Ionomer, Catalyst, and Carbon Support QPB.	63
30. The Picture of MO, MO300, MO400, and MO500.	65
31. Tested AMFC MEA With the Membrane in OH ⁻ Form (Left) and Newly Sprayed MEA With the Membrane in Br ⁻ Form (Right).	69
32. (A) X-Ray Diffractograms of MO, MO300, MO400, and MO500 Samples, (B) Integrated Diffraction Intensity of Each Plane for all the Samples.	70
33. SEM of MO (A,B), MO300 (C,D), MO400 (E,F) and MO500 (G,H) at Different Magnifications.	72
34. High Angle Annular Dark Field Images of (A) MO, (B) MO300, (C) MO400 and (D) MO500.	73
35. EELS (A) for O _K and Mn _{1,2,3} Edges of MO, MO300, MO400, and MO500, Respectively, and (B) Zoomed in Mn _{1,2,3} Edges of MO, MO300, MO400 and MO500, Respectively.	74
36. The Deconvoluted High Resolution XPS Data Of O1s in (A) MO, (B) MO300, (C) MO400 and Mn2p in (E) MO, (F) MO300, (G) MO400 and (H) MO500.	78

Figure	Page
37. The O ₂ (Red) and N ₂ (Black) CV in 1M KOH Electrolyte of (A) MO, (B) MO300, (C) MO400 and (D) MO500.....	80
38. The Electrochemical Analysis of (A) LSV of MO (Black), MO300 (Red), MO400 (Blue) MO500 (Black-Dash) and Pt/C (Red-Dash) With N ₂ Correction at 1600rpm, (B) Specific Current Density at 0.3 V Vs RHE, MO (Black), MO300 (Red), MO400 (Blue), MO500 (Black-White Stripe), (C) Tafel Slope of MO (Black-Solid), MO300 (Red-Solid), MO400 (Blue-Solid), MO500 (Black-Dash) and Pt/C (Red-Dash), (D) Methanol Tolerance in 1 M KOH and Methanol Electrolyte for Pt/C (Black) and MO400 (Red), (E) the Koutecky-Levich (K-L) Plot for MO (Black-Solid), MO300 (Red-Solid), MO400 (Blue-Solid) MO500 (Black-Dash) and Pt/C (Red-Dash), (F) The Charge Transfer Number Estimated from K-L Analysis for MO (Black-Square), MO300 (Red-Square), MO400 (Blue-Square), MO500 (Black-Circle) and Pt/C (Red-Triangle), (G) CV Data in O ₂ Saturated Electrolyte At 500 RPM, MO400 (Red) MO400 after 500 Cycles (Red-Dash) and Pt/C (Black) Pt/C after 500 Cycles (Black-Dash), (H) Chronoamperometry for Pt/C (Black) and MO400 (Red).....	81
39. AMFC Performance of MEA #S 1-4 (Test Conditions: 50 °C Using H ₂ (200 SCCM) and O ₂ (300 SCCM) Gases at 100 % RH and Ambient Pressure).....	85
40. The Main Effects Plot for S/N Ratios for Carbon, Ionomer, and Catalyst Loadings at A Different Level.....	87
41. AMFC Performance of Meas # 3 and 5.....	88
42. AMFC Performance of MEA #S 3 and 6-8.....	88

Figure	Page
43. AMFC Performance of MEA #S 6, 9 and 10.....	89
44. AMFC Performance of MEA with Both Side Pt/C and MEA #6.....	89
45. The Total Energy and The Lattice Constant of Bulk α -MnO ₂ as A Function of (A) Cutoff Energy of Planewave Basis Set and (B) K-Points Meshing of The Reciprocal Space.	96
46. The Model of The (211) Surface of α -MnO ₂ . The Mn and O Are Shown in Purple and Red, Respectively.....	98
47. The Schematics of the Top Layer Atoms of α -MnO ₂ (211) Plane, (A) The Green Circle Indicates the Eight Possible Positions for Oxygen Adsorption, (B) Four Possible Sites for Protonation. The Mn, O and H Atoms Are Represented Using Purple, Red and Grey Balls, Respectively.	99
48. Experimental (Black) and Simulated (Red) XRD of α -MnO ₂	100
49. The Adsorption Energy of Proton Inserted Surface at Position 1-4.	101
50. (A) The Adsorption Energies of Oxygen and (B) Desorption Energies of Hydroxyl Ion On Clean Surface (Black), Position 1 PS (Red), Position 2 PS (Blue), Position 3 PS (Pink) and Position 4 PS (Green).	102
51. Nitrogen Data in the “N ₂ ” Sheet.	124
52. Oxygen Data in the “O ₂ ” Sheet.....	124
53. The Outputs “O-N” Sheet Page. Fill the Information on the Top Left (Blue) and Press the “Calculate” Button, the Output Data Is Shown on The Right. the Potential Vs. RHE Is Shown in Yellow and the N ₂ Corrected Data Is Shown in Green. ..	125

Figure	Page
54. The Outputs “N” Sheet Page. Those Data Are Corrected RDE LSV Data at a Different Potential and Used to Calculate the Charge Transfer Number in APPENDIX B.	125
55. The Input Data in “Sheet1”, RPM in the First Row, the Potential in the First Column and Current Density in the Light Green Part. The Data Must be Corrected with N ₂ Current and That Can be Found in APPENDIX A.	131
56. The Inputs in “Sheet4”, Diffusion Coefficient, Viscosity, and Oxygen Concentration Are Being Inputted in the Second Row. Once Click The Button, the Potential (Green) Vs. Charge Transfer Number (Yellow) Are Shown on the Right.	132
57. The Screenshot of Showing the Table of the Diffusion Coefficient, Viscosity and Oxygen Concentration in the “Constant Data” Sheet for the Different Electrolyte, Temperature, and Concentration Along with the References.	132
58. The Screenshot of the “Sheet2”. The $\omega^{-1/2}$ (Red), The Inverse Of Current Density 1/J (Blue) and Slope (Green) Data Can be Used to Do K-L Plotting.	133
59. The Screenshot of The Data (Highlighted) Collected from Greenlight G40 Fuel Cell Testing Machine.	138
60. The Screenshot of The Data in the File “Sheet1”.	138
61. The Screenshot of the “Sheet2”. The Current Density, Voltage and the Power Density Are Shown in Yellow, Green and Blue, Respectively.	139

Figure	Page
62. The Screenshot of the (hkl) (With l = 0) Plane and the D Spacing Information in the Blue Box in “Tetragonal” Sheet (The Information Can be Found in Any XRD Analysis Software). Then Press “Calculate A” Button to Get Lattice Parameter A in Yellow.....	141
63. The Screenshot of the (hkl) (with l not in 0) Plane and the D Spacing Information in the Blue Box in “Tetragonal” Sheet, (The Information Can be Found in Any XRD Analysis Software). Then Press “Calculate C” Button to Get Lattice Parameter C in Yellow.....	141
64. The Screenshot of the (hkl) Plane and the D Spacing Information in the Blue Box in “Cubic” Sheet. Then Press “Calculate A” Button to Get Lattice Parameter A in Yellow.....	142
65. The Screenshot of the Diffraction Angle and Intensity from Cu K α X-Ray Source in The File. Then Press the “From Cu K α to Co K α ” Button to Get The Diffraction Angle, Intensity and D Spacing (Å) in Yellow.....	145
66. The Screenshot of The Diffraction Angle and Intensity from Co K α X-Ray Source in The File. Then Press the “From Co K α To Cu K α ” Button to Get The Diffraction Angle, Intensity and D Spacing (Å) in Yellow.....	146
67. The Screenshot of the Diffraction Angle (2 Theta Degree) of a _x b _(1-x) , a and b, and X-Ray Source in the Blue Part. after Clicking the “Calculate” Button, the D Spacing Of a _x b _(1-x) , a and b, and the X Percentage Value are Shown in the Yellow Box.	148

Figure	Page
68. The Screenshot of the X-Ray Source and FWHM into the Blue Part. After Clicking the “Calculate” Button, the Crystal Sizes Are Shown in The Yellow.....	151
69. The Screenshot of the POSCAR and Threshold Value in the Blue Part, by Clicking “Convert” to Process the Data.	154
70. The Screenshot of Data after Processed, the “Selective Dynamics” and the Atom Translatable or Fixed Are Added. The Data Threshold Means the Set Point of Z Value, If The $Z > \text{Threshold}$, It Will Be Able to Translate, as a Label of “t”, if the $z < \text{threshold}$, the Atom Will be Fixed, as a Label of “F”.	154
71. The Screenshot of EIGENVAL, OUTCAR and Readband_Xuan.Py.	157
72. The Screenshot of the Command “Python2 Readband_Xuan.Py”.	157
73. The Screenshot of the Band Structure Data.	157
74. The Screenshot of DOS_Element_Read_Xuan.Py, DOSCAR and POSCAR. ..	162
75. The Screenshot of the Command “Python2 DOS_Element_Read_Xuan.Py” in the Putty Software within the Correct Directory.	162
76. The Screenshot of the Projected Density of States.	162

CHAPTER 1

INTRODUCTION

1.1 Background

The world energy demand in 2017 was 14,152.8 (oil: 4435.3, coal: 3750.1, natural gas: 3107.1, bioenergy: 1384.4, nuclear: 687.7, hydro: 534.4 and other renewable energies: 253.8) million ton of oil equivalent (MTOE) and it is expected to grow to 17,714.6 (oil: 4894.2, coal: 3808.9, natural gas: 4435.8, bioenergy: 1850.6, nuclear: 971.1, hydro: 531.3 and other renewable energies: 1222.7) MTOE in 2040, as shown in Figure 1 [1]. Based on the energy policies, a nearly 5-fold increase in renewable energies in 2040 has drawn a lot of attention on the clean energy carriers. From coal to hydrocarbon, and from hydrocarbon to hydrogen, the energy source derivation tends to strip the carbon out. The specific energy per kg of coal (C), methane (CH₄) and hydrogen (H₂) are 26-33, 55.6 and 141.9 MJ. kg⁻¹, respectively [2]. Hydrogen content in the fuel does not only reduce the carbon emissions but also improves the energy density per kilogram. However, hydrogen as a fuel in gas form does not have a very promising specific energy per cubic meters. The hydrogen density at one bar is ~0.090 kg. m⁻³, but at 700 bar pressure, it will increase to 42 kg. m⁻³ due to advanced carbon fiber composite storage materials. At this pressure, 5 kg of hydrogen can be stored in a 125-liter tank, which is the quantity needed to drive ~500 km in a family-size sedan [3].

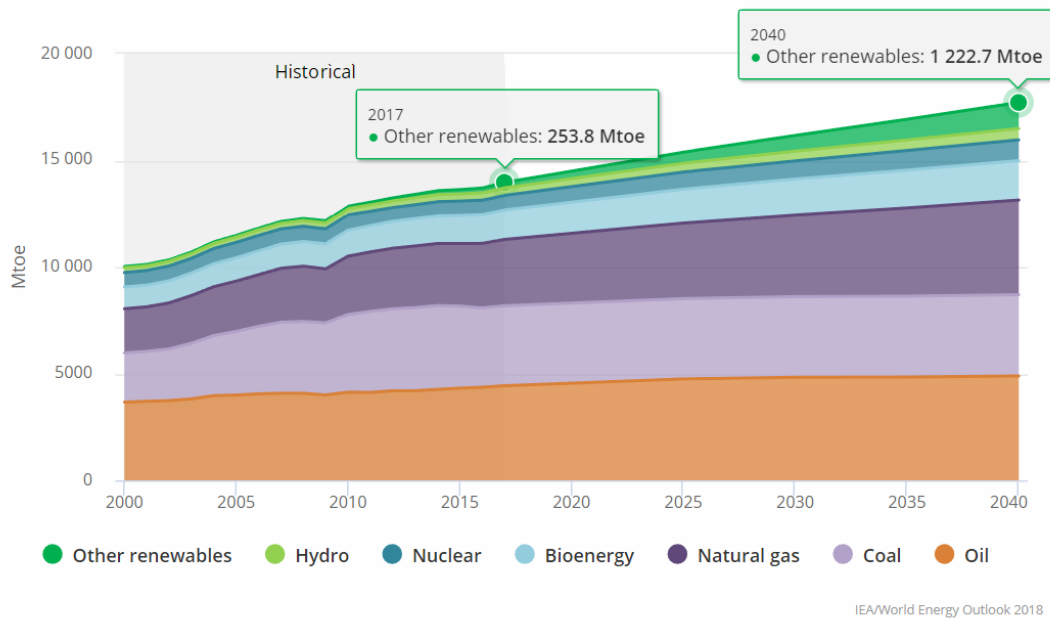


Figure 1. The world energy demand and prediction for 2017 and 2040, respectively [4].

Hydrogen is a promising energy carrier; however, it is not directly available. At present, hydrogen is mainly produced by fossil fuel, e.g. steam reforming and water-gas shift reactions. However, it can also be largely produced by electrolysis with electricity from solar and wind [5]. The other environmentally-friendly technologies are still under development; for example biomass-derived liquid reforming [6], electrolysis biomass gasification [7], thermochemical water splitting [8], photoelectrochemical water splitting [9], photobiological processes [10] and microbial biomass conversions [11]. The cost of hydrogen in Irvine California in 2018 at 350 and 700 bars were 12.99 and 14.99 \$. kg⁻¹, respectively. The department of energy's (DOE) target for hydrogen at the dispenser should be less than ~4 \$.kg⁻¹ to be competitive [12].

Hydrogen is surely a promising energy carrier in the future, but it is very important to use hydrogen more efficiently. The combustion process is well known to be limited by the Carnot cycle, which depends on the difference between combustion temperature and environment temperature. A hydrogen fuel cell is a device that directly converts the chemical energy from hydrogen into electrical energy through a non-combustion process, which means that it is not restricted by the Carnot limit. Fuel cells can be categorized as either a high-temperature fuel cell, e.g., a solid oxide fuel cell (SOFC) or a molten carbonate fuel cell (MCFC), or a low-temperature fuel cell, e.g. a PEMFC, a direct methanol fuel cell (DMFC), an alkaline fuel cell (AFC), an AMFC, or a phosphoric acid fuel cell (PAFC) [13]. The SOFC is typically running at 500 to 1000°C, so the elevated temperature could increase the kinetics at the cathode and avoid the Pt-group metal (PGM) usage as a catalyst. The natural gas can be internally reformed in the SOFC due to the high operating temperature. The thermal energy can also be harvested with a combined heat and power (CHP) system. However, different ceramic components have different thermal expansion coefficients that resulting in expensive SOFC maintenance. The MCFC is also a high-temperature fuel cell (~650 °C), so it has all the same advantages as SOFC. However, the MCFC has a hot and corrosive electrolyte mixed with lithium, potassium, and sodium carbonates. The PEMFC is the simplest, using an immobile solid-state acidic electrolyte with high power density, low operating temperature, and quick start-up and shut-down features. Nevertheless, the sophisticated Pt-based catalyst is used due to the low electrode kinetics at low temperature in acidic media. Also, pure hydrogen must be used to avoid the catalyst poisoning. With the same electrolyte, the methanol can be used in DMFC. The advantage of DMFC is the simplicity of handling liquid fuel compared to hydrogen gas.

However, DMFC has low power density and high methanol crossover problems [14]. The AFC was the first type of fuel cell used in spacecraft. The non-PGM material can be applied to the electrodes due to the alkaline environment [15]. However, the liquid KOH is used as the electrolyte and the fuel/air supply should avoid the CO₂ gas. AMFC is using a solid-state electrolyte which can resist the CO₂ contamination, but the OH⁻ ion conductivity is low compared to the KOH resulting in low power density. The PAFC is operating at ~ 220 °C with phosphoric acid as a electrolyte. This temperature boosts the electrode kinetics and prevents Pt catalyst poisoning from the CO. Nonetheless, the liquid electrolyte brings the inconvenience to the PAFC [13].

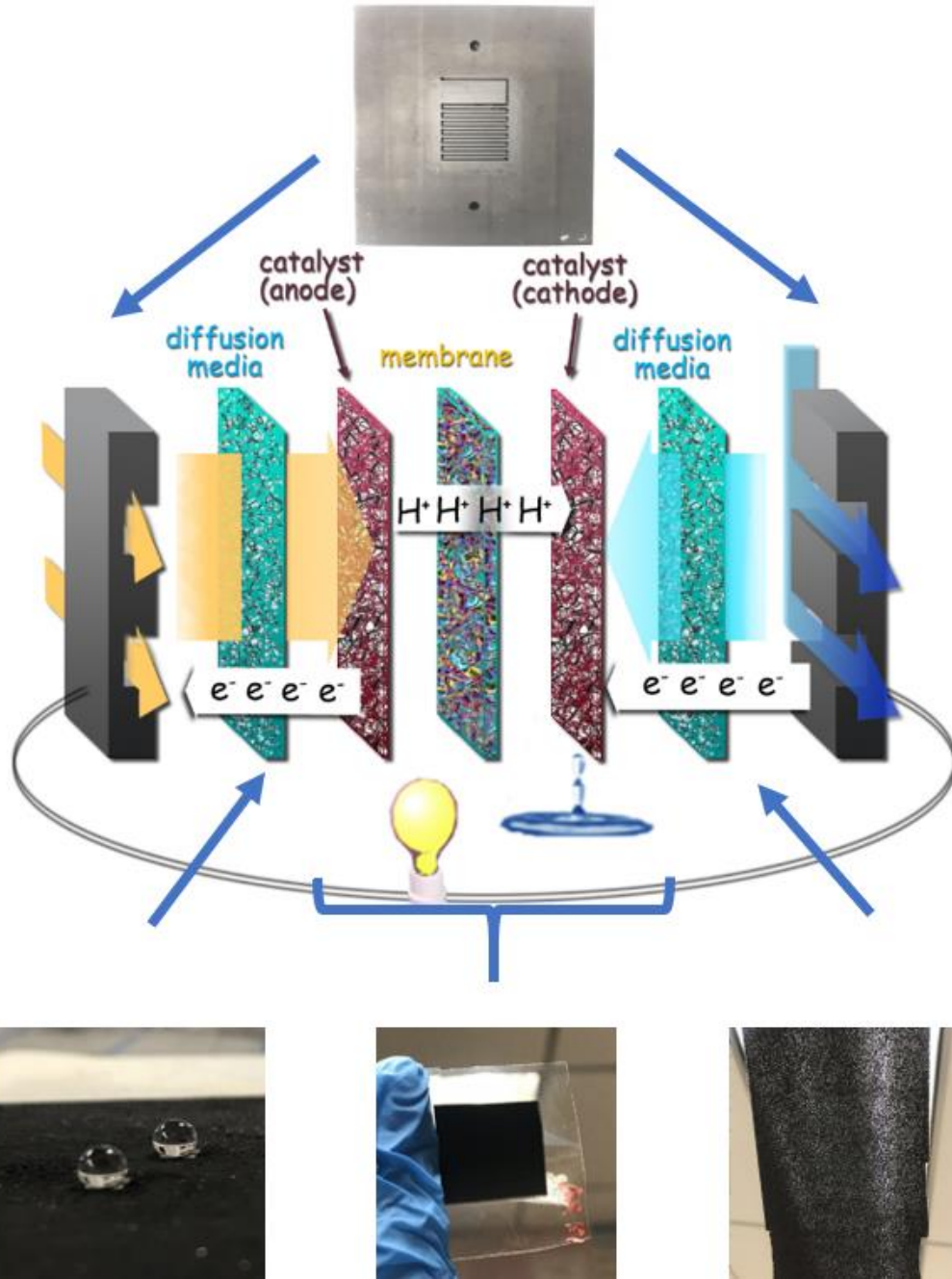


Figure 2. Components of a PEMFC.

Since the PEMFC has the advantages of a solid electrolyte, simple design, high power density, low operating temperatures, and quick start-up and shut-down. This type of fuel

cell is the most promising technology for vehicles, portable devices, and backup power supply applications. Figure 2 shows the components of a PEMFC; from left to right they are anode flow channel, anode gas diffusion layer (GDL), anode catalyst layer, electrolyte, cathode catalyst layer, cathode GDL, and the cathode flow channel. The overall reaction $O_2 + 2H_2 \rightarrow 2H_2O$ converts chemical energy of H_2 into electrical energy along with water.

The GDL is a piece of macroporous carbon paper coated with a hydrophobic microporous layer. The hydrophobic property can control the water balance to avoid the electrode flooding (block the fuel path) or membrane drying (lower the electrolyte conductivity). The ideal GDL should have properties such as good gas diffusion with optimum bending stiffness, porosity, surface contact angle, electrical/electronic conductivity, crack-free surface morphology, high mechanical integrity and enhanced oxidative stability along with durability at various operating conditions including freezing [16].

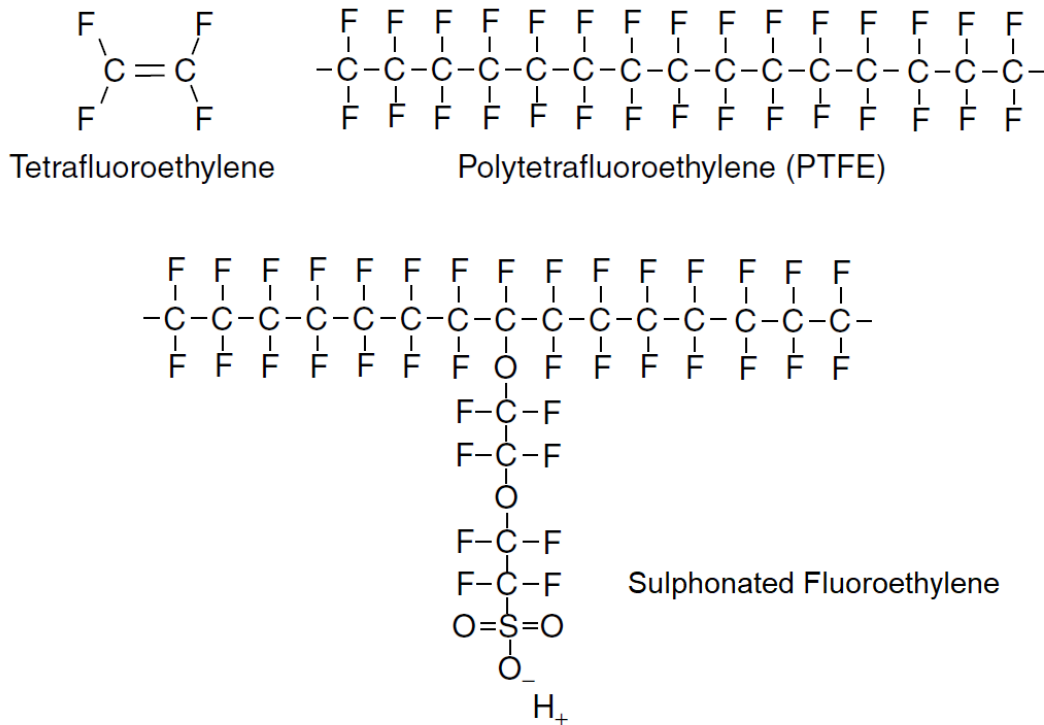


Figure 3. The structure of a sulphonated fluoroethylene [13].

The membrane electrode assemblies (MEA) are usually fabricated by coating the Nafion membrane with catalysts on both sides and sandwiched by a pair of GDLs. Nafion membrane is a sulphonated fluoroethylene (Figure 3.) with hydrophobic, hydrophilic side chains and SO_3^- ions with a typical proton conductivity of $\sim 0.1 \text{ S.cm}^{-1}$ [13].

Though the fuel cell has many advantages, there are still several challenges, e.g. system cost, hydrogen production, transportation, and storage. The current cost of a PEMFC system for a light/medium duty vehicle (L/MDV) is shown in Table 1. The cost of a $1 \text{ kW}_{\text{net}}$ power system were \$52.89, \$44.80 and \$46.16 in 2016, 2017 and 2018, respectively. The

target from the DOE is \$40 per kW for 2020 to compete with the internal combustion engine and \$30 per kW for ultimate goal [17].

Table 1. The cost of PEMFC system for L/MDV application in 2016, 2017 and 2018. The price estimations are based on 500,000 units of 100 kW system per year [17]

Parameter/Conditions	d-PtNi/C (2016)	d-PtCo/HSC (2017)	d-PtCo/HSC (ANL update for 2018)
Power density (mW.cm ⁻²)	739	1095	1165
Cell voltage (V)	0.66	0.66	0.663
Stack Pressure inlet (atm)	2.5	2.5	2.5
Temperature (coolant exit °C)	94	94	94
Total Pt loading (mg.cm ⁻²)	0.134	0.125	0.125
System cost (\$/kW _{net})	52.89	44.80	46.16

Table 2. The catalyst specifications in 80 kW fuel cell system in the current auto system and the target in 2020 and 2025 [17]

	2018	2020	2025
Stack power density	1095	1165	1500
(mW.cm ⁻²)	PtCo/HSC	PtCo/HSC	
Total Pt loading	0.125	0.125	0.088
(mg.cm ⁻²)			
Pt group metal total content (g.kW ⁻¹)	0.114	0.107	0.065

More than 40% of the cost of the system is due to the catalyst of the PEMFC. Because of sluggish kinetics of ORR on the cathode, platinum group metals or alloys are applied to catalyze the reaction. Table 2 shows the catalyst specifications in an 80 kW auto fuel cell system, as well as the targets for 2020 and 2025. The power density for 2018 is 1165 mW.cm⁻² and the targets for 2020 and 2025 are 1250 and 1500 mW.cm⁻², respectively. The platinum loadings to reach this power density with a PtCo/HSC electrocatalyst are 0.125, 0.125 and 0.088 mg_{Pt}.cm⁻² for 2018, 2020 and 2025, respectively. Also, the Pt loading per kW is targeted to reduce to 0.117, 0.108 and 0.064 g_{Pt} for 2018, 2020 and 2025, respectively [17]. Therefore, the research of the PEMFC catalyst to maximize the Pt utilization while increasing the fuel cell power density and durability is important for the commercialization.

The exchange current at the electrode determines the activity of the reaction. Typically, the exchange current density for a Pt catalyst at the cathode for ORR is $\sim 2.8 \times 10^{-3}$ A.cm⁻²,

however, for hydrogen oxidation reaction, it is five orders higher than that for ORR [18,19]. In this case, the limiting factor of fuel cell performance is mostly ORR, and thus the literature review is only focused on ORR.

1.2 The ORR Catalysts Based on Pt

The Pt-based materials are generally considered to have either a 4-electron pathway or two 2-electron pathways to reduce the oxygen. The DFT study on Pt (111) surface and the possible reaction path have been given in Keith's paper [20]. The schematic possible ORR pathways on Pt (111) surface is shown in Figure 4. In total, three pathways are proposed. (1) When oxygen is adsorbed on the Pt (111) surface, O_2^* disassociates to 2 O^* (* stands for active sites), then it is further reduced and combined with protons to form water. The O_2^* first undergo protonation forming OOH^* , (2) then further dissociates to O^* and OH^* , and finally OH^* combines with a protons to form water. (3) The OOH^* first reacts with protons, forming $H_2O_2^*$, then the peroxide further decomposes to 2 OH^* and combines with protons to form water. When the $O=O$ breaks determines the pathway which the ORR will take. It is considered that the first and second path are 4-electron reduction, and the third path is two 2-electron transfer reactions. Direct dissociate $O=O$ bonds need strong energy to overcome the reaction barrier ~ 0.44 eV [21]. Therefore, the adsorption energies of O^* and desorption energies OH^* are crucial to the catalytic efficiency. The E_{O^*} determines the dissociation of $O=O$ and when to form OH^* , the E_{OH^*} determines the reaction rate of forming water, and both energies should be in a good range. Another DFT study by Nørskov et al. reported the ORR activities vary with the adsorption and desorption energies shown in Figure 5a and Figure 5b, for ORR activities vs. E_{O^*} and, vs. E_{O^*} and E_{OH^*} ,

respectively. As so far, the best metal for ORR, Pt, has E_{O^*} and E_{OH^*} energy in a range of ~ 1.55 - 1.95 and ~ 0.98 - 1.45 eV, respectively [22].

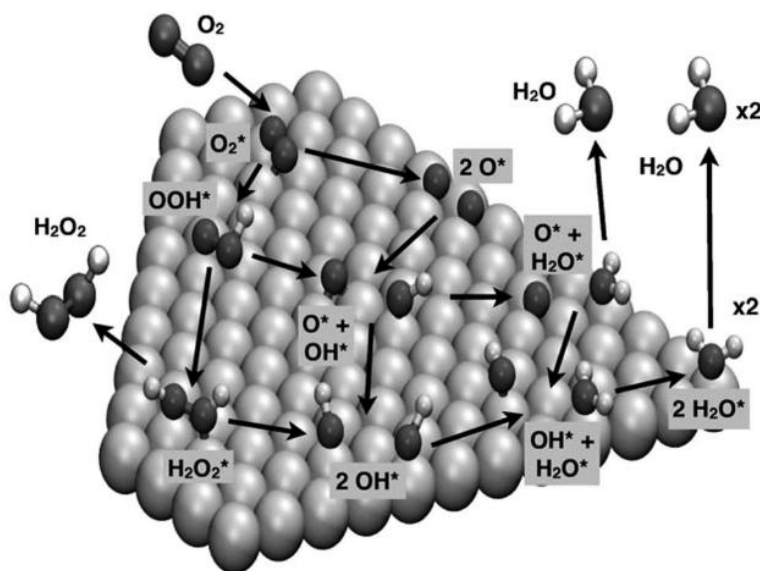


Figure 4. Possible ORR pathway on Pt (111) surface [19].

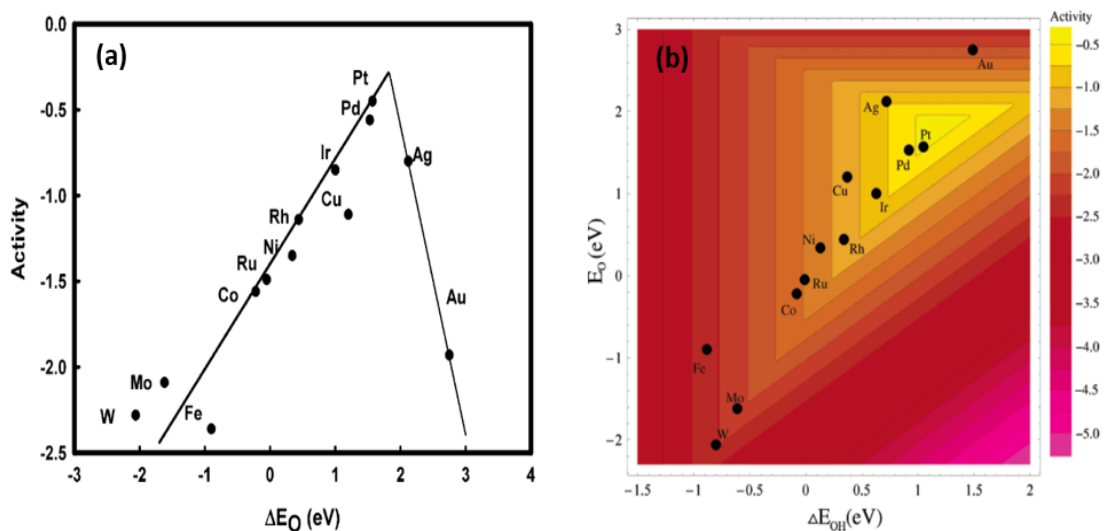


Figure 5. (a) The ORR activities vs. oxygen adsorption energies and (b) vs. oxygen adsorption and hydroxyl ion desorption energies [22].

ORR is a surface reaction, so the shape and the exposed surface of Pt nanoparticles (NP) plays an important role. The single atomic catalyst (SAC) has the highest surface to volume ratio. Many methods have been applied to synthesize it, e.g., mass-selected soft-landing method, metal leaching method, wet-chemistry method, atomic layer deposition method, and organometallic complexes approaches, all summarized in Liu's review paper [23]. The SAC doesn't give a satisfactory ORR durability due to the lack of support anchoring and further agglomeration under the fuel cell operating potential. The Pt NP size ~ 2.2 nm was reported to have the highest mass-specific current density towards ORR [24]. Different NP geometries expose different number of edges, kinks, defects and atomic densities. Xia's group conducted research on the shape-controlled synthesis of Pt nanocrystals. Details of synthesis perfect polyhedron, truncated polyhedron, overgrown polyhedron, and multipod have given in the reference [25]. As shown in Figure 6, the different polyhedron shapes tend to expose different facets to the oxygen, like Pt (110) in cubic shape and Pt (111) in octahedron and tetrahedron shape. A Pt multi-octahedron with a high ratio of Pt (111) to (100) has exhibited higher catalytic activity per unit surface area compared to the commercial Pt/C (E-Tek) due to the facets effect [26].

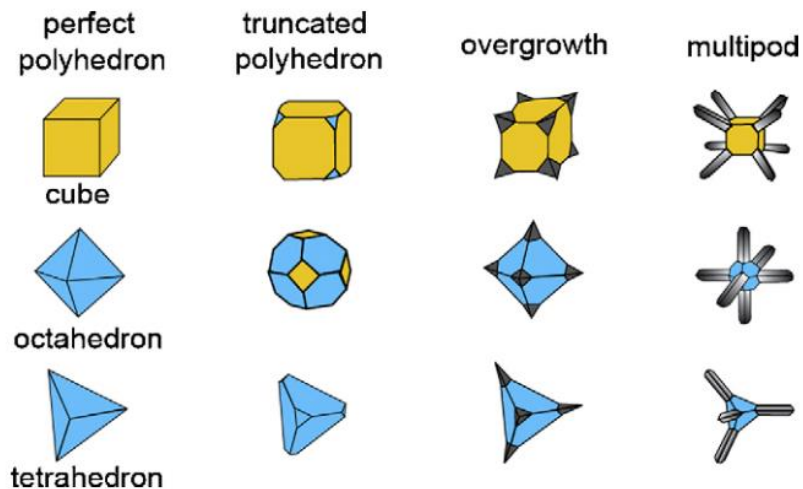


Figure 6. Schematic illustration of different shapes of Pt nanocrystals derived from conventional single-crystal polyhedron. The yellow and blue colors represent the (100) and (111) facets, respectively [25].

As mentioned before, the E_{OH^*} and E_O must be in a range of $\sim 0.98-1.45$ and $\sim 1.55-1.95$ eV, respectively, to have optimum ORR activities [22]. Adding different metals could change the adsorption energy and result in higher specific mass activities. The synthesis methods of Pt-alloy/C hollow bimetallic nanoparticles are given in the Dubau's review paper [27]. The Y/Pt (111) and Gd/Pt (111) thin film electrodes were improved by a factor of 4 compared to the Pt (111) surface [28]. The Pt₃Ni and Pt₃Co electrodes were evaluated with enhanced activity by a factor of 2 compared to the Pt polycrystalline electrodes [29]. The Pt₃Co alloy NP has the highest mass activity when the size is around 4.5 nm [30]. In PtMe alloy NPs, the electronic structures are modified by the strain (produced from the changing lattice parameter) [31] and the ligand effect (introduced by foreign transition atoms) [32]. This lowers the energy of Pt 5 d-band center, therefore reduces the E_{OH^*} and results in higher ORR activities [33,34].

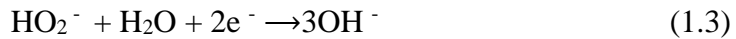
1.3 The ORR Catalyst Based non-PGM Materials in Alkaline and Acidic Media

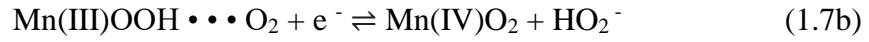
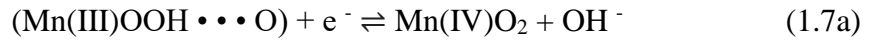
1.3.1 The ORR Catalyst Based on Manganese Oxides in Alkaline media

Among noble metal free ORR catalysts, manganese dioxides have received extensive attention due to their abundance (10th element in the earth's crust [35]), low cost, non-toxicity, lack of impact on the environment and high stability. Additionally, manganese dioxides have many polymorphs (e.g., α -MnO₂, β -MnO₂, δ -MnO₂, γ -MnO₂ and λ -MnO₂) in which the basic building blocks [MnO₆], octahedrons, are assembled to different tunnels and layer structures [36]. Various crystal polymorphs lead to different electronic structures, which influence the electrochemical performance. Li et al. studied α -MnO₂ N-doped carbon hybrid shell [37], Hang et al. reported α -MnO₂ supported g-C₃N₄ [38], and Zhang et al. studied phosphate promoted α -MnO₂ in alkaline media towards ORR [39]. Based on a comparison of the published ORR data, the specific current per dollar of α -MnO₂ is much higher than Pt/C due to the metal cost and high α -MnO₂ electrochemical properties [40]. In particular, α -MnO₂ shows onset potential and limiting current values close to those of the Pt/C benchmark in alkaline media towards ORR.

The ORR process can have two or four electrons transfer paths, depending on the active sites of the catalytic surface. The two-electron path can give higher cell potential; however, the generated peroxides will cause damages to the membrane [41]. Typically, it is favorable to synthesis peroxides [42]. For fuel cell and metal-air batteries, the four-electron transfer path is desired [43,44]. The noble metal Pt mainly goes through a direct four-electron transfer, reducing the O₂ into OH⁻ in alkaline media (eq 1.1) [45]. The ORR mechanism

for α -MnO₂ has not yet been understood clearly, but the commonly accepted mechanism was summarized in Cheng's paper [46]. Firstly, the oxygen molecule undergoes a 2-electron partial reduction, to form HO₂⁻ (eq 1.2), then further reduces into OH⁻ (eq 1.3) or decomposes into OH⁻ and O₂ (eq 1.4) [47,48]. The catalytic speed of HO₂⁻ reduction or decomposition is infinitely fast compared to the eq 1.2. Therefore, the generated peroxide ions reduces or decomposes immediately on the MnO₂ surface [49]. The MnO₂ reacts with water to form the proposed active sites Mn(III)OOH (eq 1.5). The oxygen molecule is either adsorbed onto two (eq 1.6a) or one generated Mn(III)OH (eq 1.6b), then further reduced into OH⁻ (eq 1.7a) or HO₂⁻ (eq 1.7b), respectively. The route eq 1.6a and eq 1.7a illustrate the eq 1.2 for the two-electron transfer process, and route eq 1.6b and eq 1.7b depicts the eq 1.3 for the four-electron transfer reaction. Cheng's results showed both routes exist in the ORR process in alkaline media for α -MnO₂ [46]. Cao et al. have proposed that the increase in the concentration (above 3M) will decrease the ORR performance, and the whole process rate should be controlled by the oxidation of Mn(III)OOH•••O (eq 1.7a) [50].





OV is a defect inside the manganese dioxides crystalline materials, which can change the geometry, electronics structures and elongate the adsorbed oxygen O=O bond. Li et al. have studied the OV in β -MnO₂ along with the experiment and the DFT calculations. The results concluded that moderate OV could lower the band gap, increase Fermi levels and improve the ORR performance [51], similar results have been found in other literature [52,53].

1.3.2 The ORR Catalyst Based on Me Supported on Nitrogen-doped Carbon (Me/NC) in Acidic media

In 1964, Jasinsky first reported cobalt phthalocyanine as a non-Pt material which can act as a catalyst to reduce the oxygen at room temperature in alkaline media [54]. Over the five decades since then, plenty of Me on Me/NC materials has been studied and applied to the PEMFC. It was believed ORR performance of the Me/NC macrocycle is determined by the center metal ions [55], e.g. $\text{Fe} > \text{Co} > \text{Ni} > \text{Cu} = \text{Mn}$ [56]. The active sites are not clearly understood at this time, but Zhang's review paper concluded a total of five models that are proposed by different research groups [57]:

- (1) The Van Veen model [58,59]; when the precursor is heated at 500~ 600 °C, the ligands is destroyed while the metal-N₄ ring structure remains. The further heating will connect metal-N₄ ring with carbon surface to form the moiety. This moiety is the proposed active site and that will decompose at ~850°C.
- (2) The Yeager model [60–62]; when the heating temperature is at ~ 800°C, the metal ion does not stay in the macro-ring, instead of, forming metal or metal oxide. In the acidic media, the metal and metal oxide tend to dissolve and adsorb to the C-N_x sites to form C-N_x-Me. The C-N_x-Me is proposed to be the active site for ORR.
- (3) The Wiesener model [63,64]; in this model, the metal ion does not contribute to the ORR. However, it provides a catalytic pathway for forming a special type of C-N_x which is believed to be the active site toward ORR.
- (4) The Savy model [65,66]; two different active sites at low and high heating temperature are proposed. At low heating temperature ~ 500-600 °C, a face to face

Me-N₄ dimer acts as the active site. At high heating temperature ~ 800°C, a metalless C-N_x-O_y at various oxidation state is believed to be the active site.

- (5) The Dodelet model [67–69]; also, two different active sites are proposed: Fe-N₄ and Fe-N₂. The Fe-N₄ sites are dominating in the decomposing of macrocycle compounds synthesis method and Fe-N₂ sites are dominating in the synthesis method with separate Fe and N precursors.

Recent researches are focusing on synthesizing Pt-free ORR catalyst by decomposing metal-organic frameworks (MOF) to obtain Me/NC. A peak power density ~910 mW.cm⁻² PEMFC study was published with the Zn-ZIF as catalyst template, the 1,10-phenanthroline as carbon and nitrogen precursor, and iron (II) acetate as a transition metal source under two-step pyrolysis in Ar and NH₃ [70]. Later, another group of researchers from Japan developed a type of ORR catalyst by decomposing polyacrylonitrile and iron precursor with NH₃ post-treatment. A high peak power density of 940 mW.cm⁻² was reached with hydrogen and oxygen at two atm back pressure in PEMFC testing [71]. Since then, a S doped Fe/NC electrocatalyst was synthesized with a specialized iron source Fe (SCN)₃. The reported peak power density was ~ 1030 mW.cm⁻² with hydrogen and oxygen at two atm back pressure [72]. However, the evaluations showed that the degradation of performance after 100 h in oxygen and air were 72% and 56%, respectively [70]. For the typical automobile applications, the durability should be at least 5000 h (equivalent to 150,000 miles) without noticeable performance degradation [73]. The lack of knowledge regarding the active sites hindered further performance and durability improvement [74].

1.4 The First Principles Theoretic Calculation with the Vienna Ab Initio

Simulation Package (VASP)

The energy of a material system can be calculated through a Schrodinger's equation. The non-relativistic time-independent Schrodinger Hamiltonian operator is shown in eq 1.8. The first term means the kinetic energy of N electrons; the second term means the kinetic energy of M nuclei, the M_A indicates the mass of a nucleus to electron ratio. The third term means the coulomb reaction on both nuclei and electrons. The fourth term represents the interaction between electrons, and the fifth term stands for the repulsion between the nuclei.

$$H_{\text{tot}} = - \sum_{i=1}^N \frac{1}{2} \nabla_i^2 - \sum_{A=1}^M \frac{1}{2M_A} \nabla_A^2 - \sum_{i=1}^N \sum_{A=1}^M \frac{Z_A}{r_{iA}} + \sum_{i=1}^N \sum_{j>i}^N \frac{1}{r_{ij}} + \sum_{A=1}^M \sum_{B>A}^{MN} \frac{Z_A Z_B}{R_{AB}} \quad (1.8)$$

However, this is a second order partial differential equation, and it is hard to solve even in one particle situation. If a system has two or more particles, the equation and solution will be more complicated and most time will not have an analytical solution. An example of this is the electronic structure on benzene, which contains 42 electrons. If antisymmetric functions are considered, it will consist of 126 coordinates and 42 electron spin components. The problem will become even more complicated when the heavy atoms (like Pt, Au, etc.) are calculated.

Since nuclei are much heavier compared to the electrons, an approximation was proposed by Born-Oppenheimer to let the nuclei be in a fixed position. In this case, the terms in H_{BO} are reduced to eq 1.9. The kinetic energy of nuclei (zero) and the interaction between nuclei (constant) are removed.

$$H_{\text{BO}} = - \sum_{i=1}^N \frac{1}{2} \nabla_i^2 - \sum_{i=1}^N \sum_{A=1}^M \frac{Z_A}{r_{iA}} + \sum_{i=1}^N \sum_{j>i}^N \frac{1}{r_{ij}} \quad (1.9)$$

Every term can be assumed as the function of electrons density $n(\mathbf{r})$, since the electron density is the function of the position \mathbf{r} ; this is called density functional theory [75].

Another representation in eq 1.10,

$$E(n) = T(n) + V_{\text{ne}}(n) + V_{\text{ee}}(n) \quad (1.10)$$

The $V_{\text{ne}}(n)$ can be expressed as eq 1.11:

$$V_{\text{ne}}(n) = \int n(\mathbf{r}) v_{\text{ext}}(\mathbf{r}) d\mathbf{r} \quad (1.11)$$

The $v_{\text{ext}}(\mathbf{r})$ is the external potential field as the function of position. A single electron approximation was made by treating only one electron in a multi-particle system. The other electrons and nuclei are replaced by an effective potential, as shown in eq 1.12.

$$h_s \psi_s = \left[-\frac{1}{2} \nabla^2 + v_{\text{eff}}(\mathbf{r}) \right] \psi_s = \epsilon_s \psi_s \quad (1.12)$$

The $v_{\text{eff}}(\mathbf{r})$ is given in eq 1.13.

$$v_{\text{eff}}(\mathbf{r}) = v_{\text{ext}}(\mathbf{r}) + \frac{\delta J(n)}{\delta n(\mathbf{r})} + \frac{\delta E_{\text{xc}}(n)}{\delta n(\mathbf{r})} \quad (1.13)$$

Which the electron repulsion $J(n)$ is shown in eq 1.14.

$$J(n) = \frac{1}{2} \int \frac{n(\mathbf{r})n(\mathbf{r}')}{|\mathbf{r} - \mathbf{r}'|} d\mathbf{r}d\mathbf{r}' \quad (1.14)$$

The $E_{\text{xc}}(n)$ is called exchange-correlation energy.

Since there is no other explicit solution for $E_{\text{xc}}(n)$; it consists of the correction of the kinetic energy from a non-interacting fictitious system and the non-classical effects of the

electron-electron interactions. Generally, the local density approximation (LDA) [76] and the generalized gradient approximation (GGA) [77,78] are proposed for $E_{xc}(n)$.

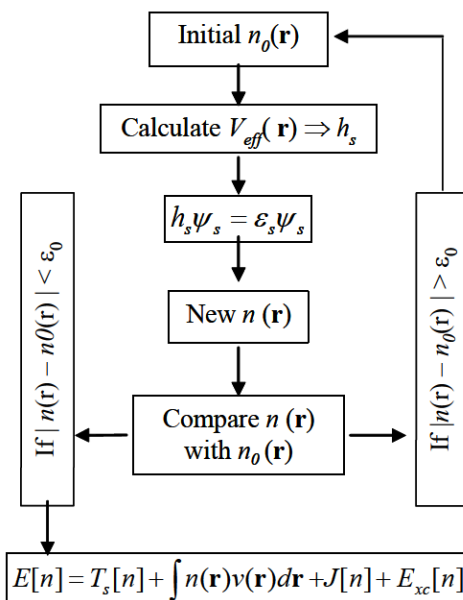


Figure 7. The flowchart of calculation through the Kohn-Sham DFT method.

The computational software package VASP uses the Kohn-Sham method to simulate the material. A flowchart of the calculation process is shown in Figure 7. In the beginning, the $n_0(\mathbf{r})$ is guessed and plugged into LDA or CGA to calculate a Hamiltonian operator h_s . A new electron density $n(\mathbf{r})$ is yielded from the wave function. When the difference between new and old electron density is smaller than the threshold ϵ_0 , the iteration is stopped. When the difference is larger than the threshold ϵ_0 , the new electron density is used to calculate the h_s in the first step, until the $n(\mathbf{r})$ converges.

The development of non-Pt electrocatalysts is progressing slowly due to the lack of knowledge regarding the reaction mechanism and the fact that the proposed mechanism

cannot be proved by the modern characterization techniques [74]. Another route to view and examine this problem could be using first principles material simulation with DFT packages. With the advances in the supercomputer computing speed, the material modeling on a bulk surface could be achieved. Since the ORR is a surface catalyzed reaction, the ORR 4-electron process can be simulated by determining the adsorption and desorption energies between reactant and catalyst surfaces. Nørskov et al. has reported the trend of ORR activities in the variables of adsorption and desorption energies for different metals [22]. The adsorption and desorption energies can be defined as $E_{ad} = E_{adsorbate/catalyst} - E_{catalyst} - E_{adsorbate}$. If the E_{ad} is negative, it indicates the $E_{adsorbate/catalyst}$ is lower than the sum of $E_{catalyst}$ and $E_{adsorbate}$, which is favorable to form adsorption. Similarly, if the E_{ad} is positive, the adsorption process will not be favorable and indicates the desorption process [51].

1.5 Objectives

Based on the previous literature review, the MOF is a newly emerging platform for synthesizing the ORR electrocatalysts [79,80]. One kind of MOF, ZIF, is rich in carbon, nitrogen and transition metals. After carbonization at high temperature in the inert atmosphere, the N atoms tend to bond with the surrounding transitional metal ions to form the proposed active sites MeN_4 . Since the synergic effect between Pt-Me alloy and MeN_4 has never been studied before, the first objective is to combine them and then evaluate the performance.

Even though the Me/NC electrocatalyst showed good ORR activity in PEMFC testing, the durability still does not yet meet the industrial requirements [70]. Most of the non-PGM

ORR catalyst is based on Fe, Ni, Co, Cu, and Mn, which tend to dissolve into the acidic electrolyte. Alkaline media provides a milder environment for those metals. α -MnO₂ is known for its good catalytic ability, non-toxicity, low cost, and its abundance. OV is the defect inside the manganese dioxides crystalline materials, and it can boost the ORR performance in β -MnO₂ [51] and δ -MnO₂ [52]. Since OV effect has never been studied in α -MnO₂, the second objective is on thermal induced OV in α -MnO₂ towards ORR in alkaline media and AMFC.

The fuel cell electrocatalysts are developing slowly due to the lack of knowledge of the active sites and the reaction mechanism [74]. The modern chemical characterization techniques cannot resolve or prove the proposed mechanisms. The first principles theoretical calculation is a supplementary tool to the electrochemical method to explore the insight of ORR. The third objective is to use first principles theoretical calculation to simulate the protonation effect and active sites on α -MnO₂ (211) surfaces.

1.5.1 Objective 1

The Co-ZIF and NiCo-ZIF were synthesized by the solvothermal method. The Pt precursor was further mix with Co-ZIF and NiCo-ZIF, then underwent pyrolyzing and acid leaching processes. During the pyrolysis, the Pt and Me were reduced and tend to form an alloy. The Pt alloy could increase the Pt usage efficiency per Pt atom and the stability of the catalyst. The carbon tends to graphitize and provide a good conducting network. The N tends to bond with C, Me, and Pt or PtMe alloys to boost the ORR. The additional acid leaching was used to remove all the unstable metal particles in the catalyst. The final

products were examined under XRD, scanning electron microscopy (SEM), transmission electron microscopy (TEM), rotating disk electrode (RDE), and PEMFC testing.

1.5.2 Objective 2

The proposed experiment is synthesizing α -MnO₂ by the hydrothermal method with MnSO₄.H₂O and KMnO₄. The OV was introduced by post heat treatment at 300, 400 and 500 °C. The resulting products were examined under XRD, SEM, scanning transmission electron microscopy (STEM), X-ray photoelectron spectroscopy (XPS), RDE, and AMFC testing.

1.5.3 Objective 3

In this proposed research, the ORR on α -MnO₂ (211) planes in alkaline media were modeled in three steps. (1) α -MnO₂ is going to undergo water uptake or protonation to form MnOOH, (2) the MnOOH is acting as an active site to adsorb the oxygen, (3) the oxygen will be reduced to OH⁻ and then desorbed from the surface. Due to the α -MnO₂ (211) plane contributing the most towards the ORR [81], a supercell was created with a (211) plane as the top surface. Based on the symmetry, there were a total of four possible sites at which the proton bonded with oxygen, and eight possible positions for oxygen to be adsorbed onto the α -MnO₂(211) plane. In summary, 40 different cases were calculated, and the result was the possible sites which are favorable to reduce the oxygen.

1.6 Structure of the Dissertation

The objectives provided in this Chapter will be discussed in detail through experimental and theoretical outcomes in the Chapters 2 to 4. Chapter 2 provides the synthesis and characterization of Pt alloy catalysts (PtCo and PtNiCo NP) supported on the nitrogen doped carbon towards ORR in PEMFC. Chapter 3 studies the thermal induced OV in α -MnO₂ towards ORR in alkaline media and AMFC. The Chapter 4 further analyzes the protonation effect and active sites towards ORR on α -MnO₂ (211) plane using theoretical study using VASP. Finally, the Chapter 5 summarizes all the research reported in each Chapter and provides recommendation for future development of various ORR electrocatalysts.

CHAPTER 2

PLATINUM COBALT ALLOY AND PLATINUM NICKEL-COBALT ALLOY SUPPORTED ON THE NITROGEN DOPED CARBON DERIVED FROM COBALT-ZIF AND NICKEL COBALT-ZIF TOWARDS ORR IN PEMFC

2.1 Introduction

As specified in Chapter 1, one of the major objectives is to maximize Pt utilization for cost reduction with improved durability of the ORR catalyst in PEMFC. Since ORR is a surface reaction, the shape and the exposing surface of Pt NP plays an important role. The smaller of the Pt particles, the higher of the surface to Pt atom ratio, which means Pt is used more efficiently. Many methods were applied to synthesize Pt NPs, e.g., mass-selected soft-landing method, metal leaching method, wet-chemistry method, atomic layer deposition method, and organometallic complexes approach, all summarized in the literature [23]. However, smaller NPs are not necessarily better as they will not be stable thermodynamically and the Pt NPs of ~ 2.2 nm showed the highest ORR performance in PEMFC [24]. Therefore, the method used to control particle size is also very crucial to achieve high PEMFC power density. Another way to increase the Pt utilization is to alloy Pt with other transition metals; in the meantime, both the power density and durability were improved [82]. The E_{OH^*} and E_O must be in a range of ~0.98-1.45 and ~1.55-1.95 eV, respectively, to have optimum ORR activity [22]. Adding different Me could change the adsorption energy, resulting in higher specific mass activities [28–30,83]. In PtMe alloy NPs, the electronic structures are modified by strain from changing lattice parameter [31] and the ligand effect introduced by foreign transition atoms [32]. This will lower the energy of Pt 5 d-band center, therefore reduces the E_{OH^*} results in higher ORR activities [33,34].

The MOF is a newly emerging platform for synthesizing the ORR electrocatalyst [79,80,84]. As one kind of MOF, ZIF, is rich in carbon, nitrogen and transition metals. After carbonization at high temperature in the inert atmosphere, the N atoms tend to bond with the surrounding transitional metal ions, to form the proposed active sites MeN_4 .

In this study, the Co-ZIF and NiCo-ZIF were synthesized by the solvothermal method. The Pt precursor was further mixed with Co-ZIF and NiCo-ZIF materials, then underwent pyrolyzing and acid leaching process. The final products were examined under XRD, SEM, TEM, RDE, and PEMFC testing.

2.2 Experimental Section

2.2.1 Synthesis of Co-ZIF and NiCo-ZIF Particles

Co-ZIF samples were synthesized as described in the published literature [85]. In a typical synthesis, 1.97 g of 2-methylimidazole (2-MIM) was dissolved in a mixed solution of 20 ml of methanol and 20 ml of ethanol. Then 1.746 g of $\text{Co}(\text{NO}_3)_2 \cdot 6\text{H}_2\text{O}$ was dissolved in another mixed solution of 20 ml of methanol and 20 ml of ethanol. The above two solutions were further mixed under continuous stirring for a few minutes and held for 20 h at room temperature. The purple precipitate was collected by centrifuging the solution, then washed in ethanol several times and dried at 80 °C overnight. NiCo-ZIF were synthesized by modifying the previous method. Typically, 1.97 g of 2-MIM was dissolved in 20ml of methanol, 873 mg of $\text{Co}(\text{NO}_3)_2 \cdot 6\text{H}_2\text{O}$ and 873 mg of $\text{Ni}(\text{NO}_3)_2 \cdot 6\text{H}_2\text{O}$ were dissolved in 60ml of methanol. The above two solutions were then mixed and stirred at room

temperature for 24 h. The purple precipitate was collected by centrifugation, washed in methanol several times and dried at 80°C.

2.2.2 Synthesis of PtCo/NC and PtNiCo/NC

The ZIF-67 particles were mixed thoroughly by stirring in a $\text{H}_2\text{PtCl}_6 \cdot 6\text{H}_2\text{O}$ solution (5 wt.% in deionized water) and the resultant slurry was dried at 80 °C for about 2 hours. The dried powder was heated at 350 °C for 1.5 h then raised to 700 °C at a ramp rate of 2 °C per minute and pyrolyzed for 3.5 h under flowing Ar- H_2 (90:10% volume ratio) atmosphere. After, the as-prepared black powder product was cooled down to room temperature naturally. Next, it was treated in 0.5 M H_2SO_4 solution for six hours. The resultant catalyst product was collected by centrifugation, repeatedly washed with deionized (DI) water and then dried at 80 °C under a vacuum for about 2 hours. The Pt loading on the nitrogen doped carbon (NC) was 10 wt.% based on the initial composition. An upgraded method was employed to synthesize the PtNiCo/NC. The NiCo-ZIF particles was mixed with $\text{H}_2\text{PtCl}_6 \cdot 6\text{H}_2\text{O}$ solution under the sonication then dried at 80°C for 3 hr. The resultant powder was then pyrolyzed by the previous method. The Co/NC and NiCo/NC were pyrolyzed directly from ZIF without Pt precursor by the same method.

2.2.3 Catalyst Characterization and Analysis

The morphology and structure of the Co-ZIF, NiCo/NC, PtNiCo/NC and PtCo/NC were characterized by a SEM HITACHI S-4700 and a TEM, Philips CM200, 200 kV. The XRD were recorded using a SIEMENS D5000 X-Ray Diffractometer with Cu $\text{K}\alpha$ radiation (Cu $\text{K}\alpha$, $\lambda = 1.54 \text{ \AA}$ nm, 40 kV and 30 mA). For NiCo-ZIF and PtNiCo/NC, XRD data were

collected by the SIEMENS D5000 X-ray Diffractometer with a Co anode (Co $K\alpha$, $\lambda = 1.79 \text{ \AA}$). The data collection was from 5 to 29 and 20 to 70 2θ degrees for ZIF samples and pyrolyzed ZIF samples, respectively, with 0.02 2θ degrees per step and 1 step per second. The reason Co target was chosen instead of Cu target was that the Co-containing samples exhibited the greatest fluorescence under Cu $K\alpha$. That will lead to low signal to noise ratio. It was solved by applying a longer wavelength Co $K\alpha$ X-ray. HAADF and EDS mapping were recorded by a STEM (JEM-ARM200F) at 200 keV for PtNiCo/NC. Inductively coupled plasma mass spectrometry (ICP-MS) elemental analysis was carried out by taking 5 mg of PtNiCo/NC ashes (oxidized at 800°C for 2h) with 3 ml and 1 ml trace metal grade of HCl and HNO₃, respectively. The mixture was agitated and then kept at 80°C overnight for metal digestion. After filtering out the undigested ashes, the sample was diluted to the detection limit with DI water and measured on Thermo Scientific's iCAP Q quadrupole ICP-MS using an Elegra Argon humidifier.

2.2.4 Thin Film Rotating Disk Electrode and Electrochemical Evaluation

Catalyst ink was prepared by dispersing 7.6 mg of PtCo/NC (10 wt.% Pt) or Co/NC or commercial Pt/C (46.8 wt.% Pt; Tanaka TKK, Japan) in 7.6 ml of DI water (Resistivity 18.2 M Ω .cm), 2.4 ml of isopropyl alcohol and 40 μ l of 5 wt.% Nafion dispersion (LQ-1005-1000, Ion Power Inc.), and then sonicated in a cold-water bath for 20 min [86]. A thin catalyst film was deposited by dropping a required volume of the catalyst ink onto the polished glassy carbon (GC) disk (4 mm diameter, AFE3T040GC, Pine Instruments) to obtain Pt loading of 45 and 15 μ g. cm⁻² in commercial Pt/C and PtCo/NC nano-catalysts, respectively. For comparison purposes, a thin film electrode with non-platinized Co/NC (~

290 $\mu\text{g. cm}^{-2}$) was also prepared. Uniform and well-adhered catalyst films were obtained by rotational air drying at room temperature for 15 min, for all three different catalysts [86]. For PtNiCo/NC and NiCo/NC, approximately 45 $\mu\text{g}_{\text{Pt. cm}^{-2}}$ and 700 $\mu\text{g. cm}^{-2}$ were applied to a 5 mm diameter GC electrode (AFE5T050GC), respectively.

RDE experiments were carried out in 0.1 M HClO₄ (Sigma-Aldrich) with N₂ as well as O₂ saturation [87]. Linear sweep voltammetry (LSV) experiments were conducted in the potential range of 0.7 to -0.3 V vs. a saturated calomel electrode (SCE), which was 1 to 0 V vs. a reversible hydrogen electrode (RHE), at 20 mV.s⁻¹ rate with Pt coil as a counter electrode and SCE as a reference electrode using a PAR Bistat at various rpm, at room temperature. To evaluate the performance stability of the PtCo/NC catalyst film, cyclic voltammetry (CV) was conducted for the disk electrodes between 1 and 0.6 V vs RHE with a sweep rate of 50 mV.s⁻¹ at 400 rpm for 50 cycles in a 0.1 M O₂ saturated HClO₄ electrolyte solution [86]. For PtNiCo/NC, a stability test was performed at room temperature in an oxygen-saturated 0.1M HClO₄ solution by applying cyclic potential sweeps between 0.5 and 1.1V versus RHE at a sweep rate of 200 mV. s⁻¹ for 5000 cycles.



Figure 8. Polished RDE working electrode.

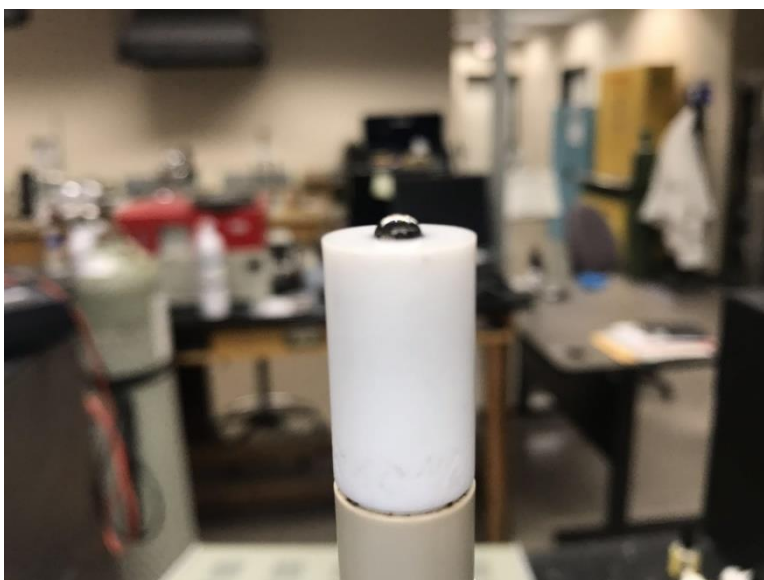


Figure 9. Ink restricted on the GC electrode.



Figure 10. Thin film on RDE.

The polished working electrode is clean and shiny, enclosed with a white insulation made by polytetrafluoroethylene (PTFE), as shown in **Error! Reference source not found.** The PTFE is a hydrophobic material, which means it tends to expel the water whereas the glassy carbon is hydrophilic material and tends to attract water. The RDE ink was mostly made by DI water due to this reason; the ink can be confined perfectly inside the GC electrode (Figure 9). Adding IPA helps the carbon-based material to disperse better. The final uniform and well-adhered film with rotation drying is shown in Figure 10.

2.2.5 Catalyst Coated Membranes

For the PEMFC single cell tests, the MEAs with an active area of 5.0 cm^2 were fabricated as described below. The Commercial Pt/C (Tanaka TKK TEC10E50E, Japan) were used as anode catalysts. The cathode catalyst ink was prepared by mixing 200 mg PtCo/NC or commercial Pt/C nano-catalysts in 2.6 ml of 5 wt.% Nafion dispersion (LQ-1005-1000, Ion

Power, Inc.) and 5 ml of isopropyl alcohol under inert atmosphere. The catalyst coated membranes (CCM) were fabricated by spray coating PtCo/NC or PtNiCo/NC catalyst ink on the cathode side (Figure 11) and commercial Pt/C catalyst ink on the anode side, on a Nafion-212 (Ion Power Inc.) membrane and vacuum-drying at 70 °C for half an hour (Figure 12). CCMs were also prepared with both anodes and cathodes commercial Pt/C for fuel cell performance comparison. The Pt loading was 0.2 and 0.12 mg_{Pt}. cm⁻² on the anode and cathode sides of the CCM, respectively. The same method was applied for the PtNiCo/NC and the Pt/C reference CCM. The resulted Pt loadings are 0.12 and 0.12 mg_{Pt}. cm⁻² on anodes and cathodes, respectively. For the non-Pt cathode, the ionomer:catalyst ratio was ~1:2 and the loading was ~ 3.5 mg.cm⁻².



Figure 11. ExactaCoat machine.

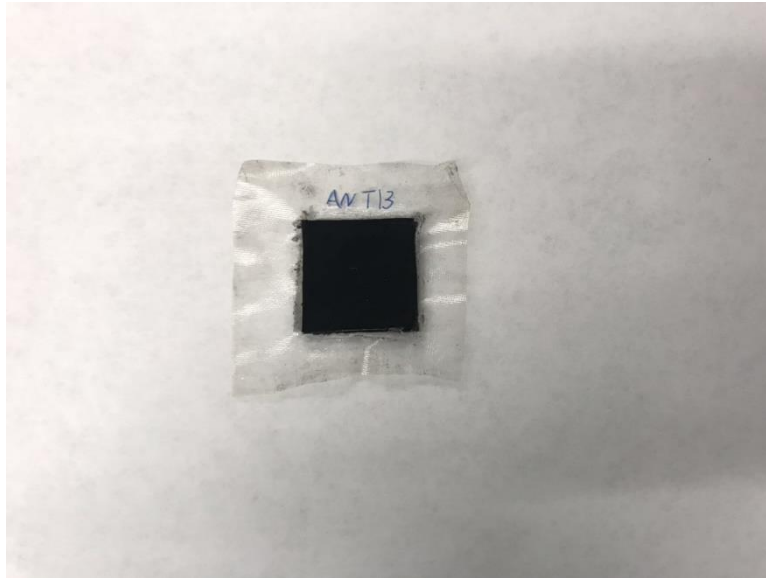


Figure 12. PEMFC MEA on Nafion 212 membrane.

2.2.6 Gas Diffusion Layer

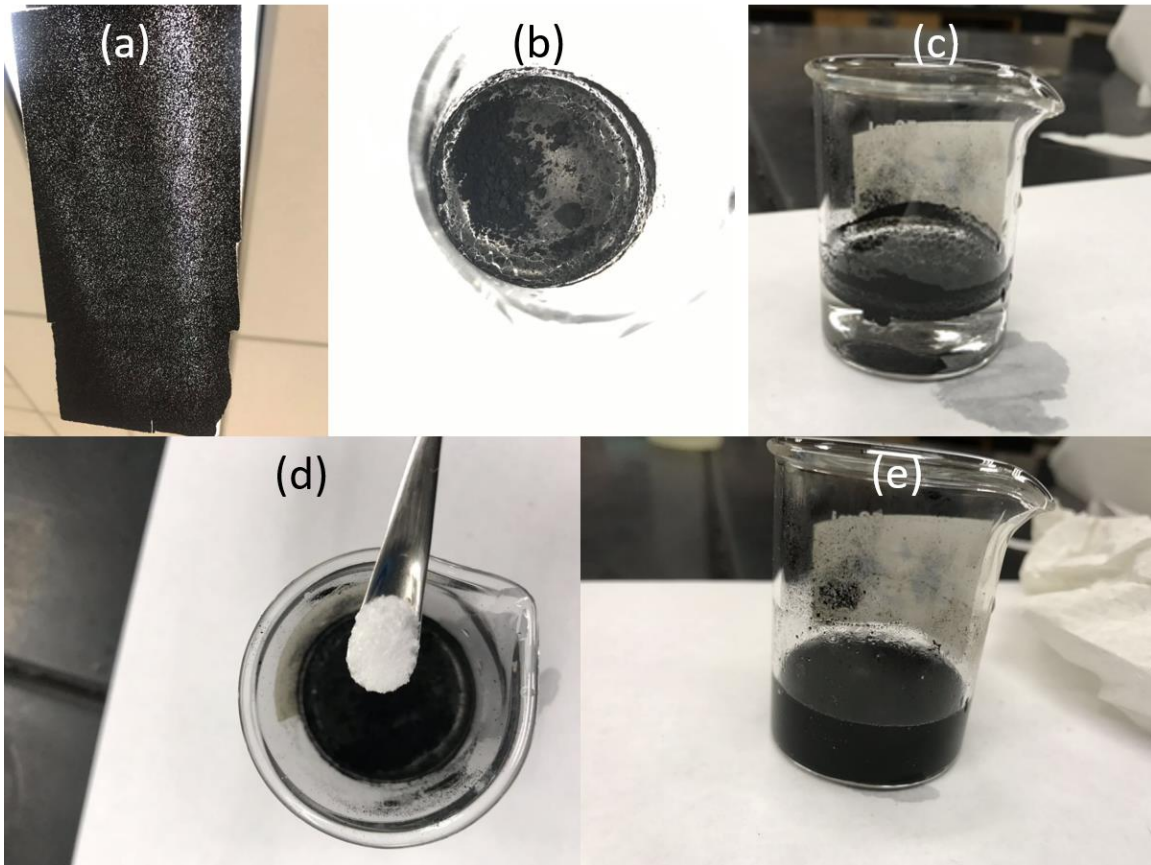


Figure 13. (a) carbon paper (b) the carbon in water without SDS (top view) (c) the carbon in water without SDS (side view) (d) adding SDS and (e) the carbon suspended in water.

Graphitized non-woven carbon paper (GD07508G, Hollingsworth & Vose Company) was used as a substrate for fabricating GDLs (Figure 13a). Nano-chain Pureblack carbon (grade 205-110) from Superior Graphite Co., vapor grown carbon fiber (VGCF) from Showa Denka, Teflon dispersion (DISP 30, Fuel cell earth) and sodium dodecyl sulfate (SDS) from Fisher Scientific were used for carbon slurry preparation. In brief, 0.5 g of carbon powder (75 wt.% Pure black carbon powder and 25 wt.% VGCF) was dispersed in 6.5 ml of DI water containing 120 mg of SDS by sonicating for 30 min and stirring the mixture for 60 min. Figure 13b (top view) and Figure 13c (side view) show the carbon powder mixed with water without SDS. The carbon was floating and not suspended well in the water. Figure 13d and Figure 13e shows the well-dispersed carbon powder in the beaker after adding SDS. SDS is an anionic surfactant which consists of a 12-carbon tail attached to a sulfate group. The carbon bundles are exfoliated during sonication and stabilized by the SDS adsorption (Figure 14a-d). The carbon unit-SDS dispersion could be stable for several months with a critical micelles forming concentration of ~ 0.2 wt.% SDS [88]. The carbon-surfactant interaction could be visualized through cylindrical micelles (Figure 14e), hemimicelles (Figure 14f) or randomly adsorbed surfactant on carbon unit (Figure 14g). In particular, with the critical micelles forming a concentration of ~ 0.2 wt.% SDS, there is a formation of SDS randomly adsorbed on carbon units (Figure 14g) [89].

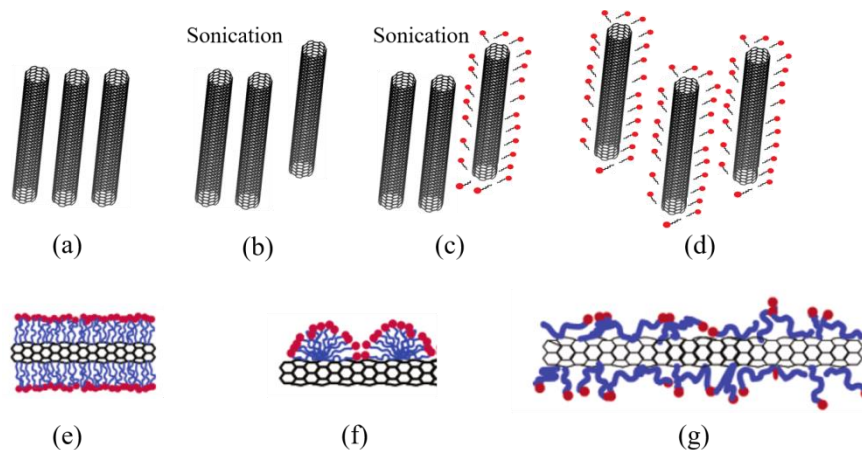


Figure 14. Schematic representation of isolating carbon bundle by ultrasonication. (a) carbon bundle, (b) single carbon unit separated by sonication, (c) surfactant adsorption on isolated carbon unit, (d) dispersed carbon unit with help of surfactant, and the possible way of carbon-surfactant interactions: (e) cylindrical micelles, (f) hemimicelles and (g) random adsorption.

After, teflon (30 wt.%, Fuel Cell Earth) dispersion was added into the mixture and followed with magnetic stirring for 10 min. The non-woven carbon paper substrate (10 cm x 10 cm) was coated with the carbon slurry at $3 \text{ m}\cdot\text{min}^{-1}$ speed using Easycoater equipment (EC26, Coatema) as shown in Figure 15. After coating the microporous layer, the GDL samples were dried at room temperature overnight followed by sintering at $350 \text{ }^\circ\text{C}$ for 30 min in air. GDL samples were washed thoroughly to remove the SDS by immersing in DI water for 30 min. The carbon loading on the microporous layer was controlled by the gap between the wire-rod and substrate to achieve a $\sim 3 \text{ mg}\cdot\text{cm}^{-2}$ loading [90]. As shown in Figure 16, the GDL is highly hydrophobic in nature.



Figure 15. EC26 Coatema machine with the carbon slurry coated carbon paper.

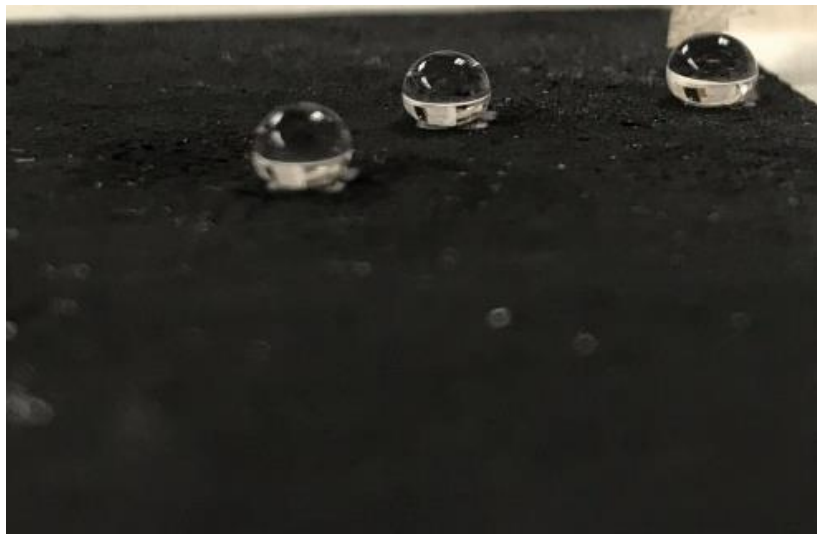


Figure 16. GDL with water droplets demonstrating its hydrophobic characteristics.

2.3 Discussion for PtCo/NC

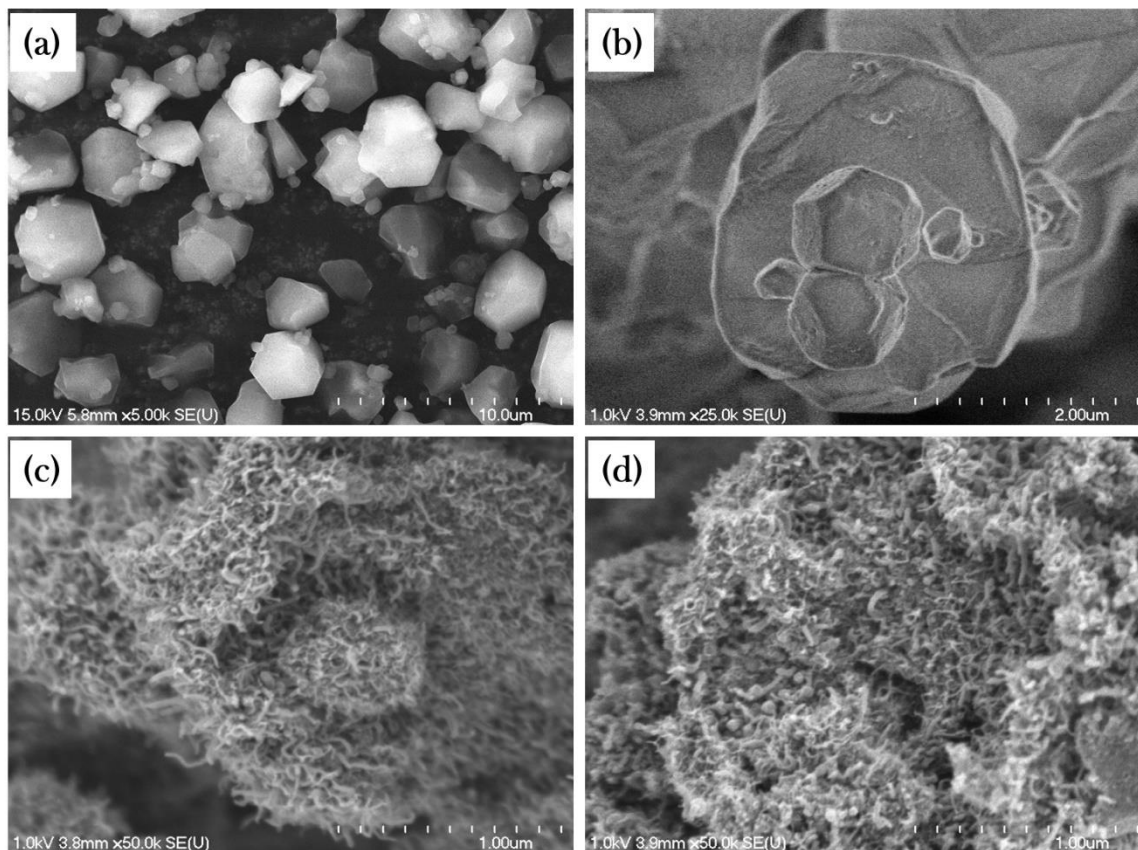


Figure 17. SEM of (a) and (b) ZIF-67 at two different magnifications, (c) Co/NC and (d) PtCo/NC.

Figure 17 shows the structure of ZIF-67 at two different magnifications. As seen from the scanning electron micrographs, the dimension of the larger ZIF particles was about 2 μm . However, smaller ZIF particles were also observed (see Figure 17a, b). The pyrolyzed samples were also examined by SEM and are given in Figure 17c and d. As seen in Figure 17c, carbon nanostructure was densely grown with the ZIF-67 shape still intact in the Co/NC sample. Figure 17d shows the surface structure of PtCo/NC. Adding Pt precursor did not change the morphology of catalyst support during the deposition of Pt nanoparticles. In both the Co/NC and PtCo/NC samples, the nitrogen-doped carbon nanostructures were

twisted, entangled and well-integrated to provide a conducting network as catalyst support. As the sample were synthesized by following the published literature, the nitrogen doping amount and the BET surface area were expected to be $\sim 2.4\%$ and $500\text{ m}^2\cdot\text{g}^{-1}$, respectively [91].

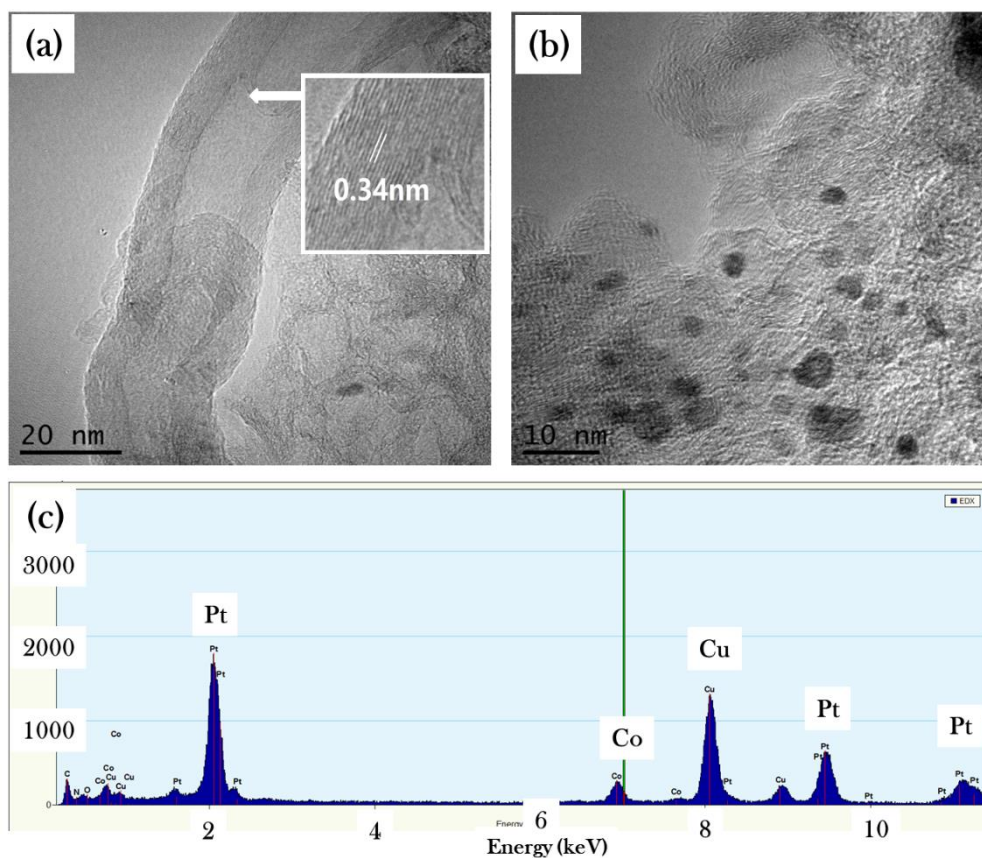


Figure 18. Transmission electron micrographs for (a) Co/NC, (b) PtCo/NC and (c) EDS for PtCo/NC shown in (b).

A TEM image of the Co/NC (Figure 18a) shows the evidence of well-defined multiwall carbon nanotubes and the darker dot is cobalt particle. As seen from Figure 18a, the

diameter of the multiwall carbon nanotubes (CNTs) is ~ 20 nm. Graphitic lattice fringes (with 0.34 nm) were also observed in high-resolution TEM analysis (inset shown in Figure 18a), which would exhibit superior conducting network as well as electrochemical stability. The TEM image of PtCo/NC (Figure 18b) shows the presence of Pt nanoparticles (7 to 10 nm) homogeneously dispersed on the NC supporting matrix. To identify the specific metallic elements, EDS analysis was carried out. As seen in Figure 18c, the majority of the nanoparticles were Pt, but there was also Co present in the platinized carbon. XRD study was conducted to quantify the Co on the catalyst sample.

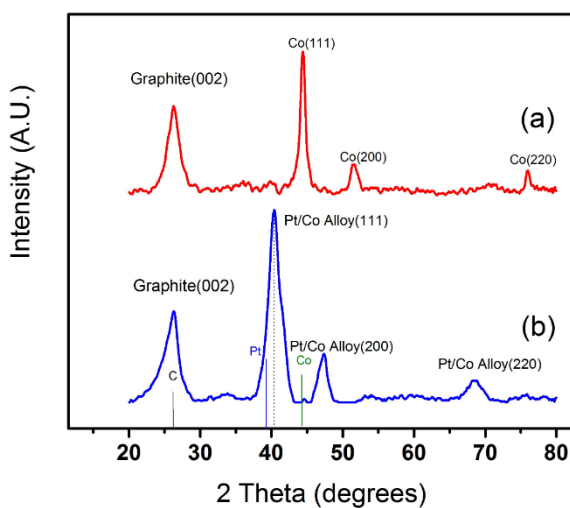


Figure 19. X-Ray diffractograms of (a) Co/NC and (b) PtCo/NC.

XRD patterns for Co/NCs and PtCo/NC are given in Figure 19. As clearly observed, both the Co/NCs and PtCo/NC showed the presence of graphitic carbon at 2θ value of ~26.3 (hkl value: 002), confirming the graphitized carbon under TEM examination. Three other major diffraction peaks in the Co/NC (Figure 19a) were identified as Co (111), Co (200) and Co (220) planes at the 2θ values of 44.36, 51.67 and 75.98, respectively. In the case

of PtCo/NC, the presence of the Pt-Co alloy was identified and was expected to exhibit enhanced electrochemical performance towards ORR [92]. Based on the lattice parameters of Pt (3.92 Å) and Co (3.53 Å), the composition of the PtCo/NC (3.86 Å) was estimated to be 5:1 for Pt: Co alloy ratio using Vegard's law [93]. From the Scherer Equation, the average crystallite size was calculated (using full width half maximum) as 10.5 nm for the PtCo/NC, which was nearly identical to the value estimated from the TEM images.

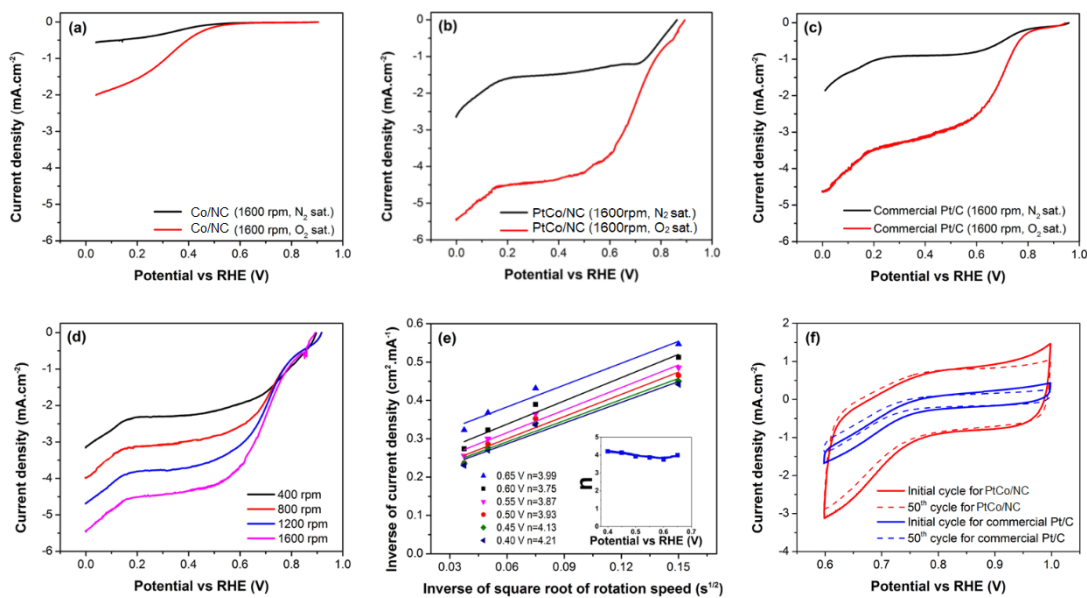


Figure 20. RDE data HClO₄ electrolyte at 23 °C for (a) Co/NC, (b) PtCo/NC at 1600 rpm, (c) commercial Pt/C at 1600 rpm, (d) PtCo/NC at various rpm, (e) Koutecký–Levich (KL) plot for PtCo/NC at various potentials with inset shown the number of electron change and (f) CV data for PtCo/NC and commercial Pt/C at 400 rpm.

In order to evaluate the PtCo/NC nano-catalyst towards ORR performance, mechanism and durability, the electrodes were fabricated and LSV experiments were conducted in a 3-electrode system in the 0.1 M HClO₄ electrolyte [94]. For comparison purposes, the RDEs with Co/NCs and commercial Pt/C were also evaluated under identical conditions. Figure 20 a, b and c show the ORR activities of Co/NCs, PtCo/NC and commercial Pt/C in N₂, as well as the O₂, saturated electrolyte at 1600 rpm, respectively. As seen in Figure 20a, the Co/NC did show some ORR activity in the O₂ saturated electrolyte, but it was very low (-1.52 mA mA.cm⁻² after background correction) at 1600 rpm. As observed in Figure 20b, PtCo/NC showed the limiting current of -5.43 mA.cm⁻² (-2.78 mA.cm⁻² after subtracting N₂ current) in the O₂ saturated electrolyte at 1600 rpm, with a Pt loading of 15 μg. cm⁻². However, the commercial Pt/C in the O₂ saturated electrolyte only showed -4.63 mA.cm⁻² (-2.77 mA.cm⁻² after subtracting N₂ current) (see Figure 20c) with a Pt loading of 45 μg. cm⁻² under identical conditions. From the LSV data (Figure 20b and c), the PtCo/NC with one-third of Pt loading had a slightly higher ORR value compared to that with a commercial Pt/C based thin film electrode, probably due to the synergetic effect of the Pt-Co nanoparticle with the NC network as a supporting matrix. Figure 20d shows the LSV data for the PtCo/NC in the O₂ saturated electrolyte at different rpm. Figure 20e presents the K-L plot obtained from the RDE data on ORR for PtCo/NC at several rotation rates in the O₂ saturated electrolyte given in Figure 20d. The intercepts of the extrapolated K-L lines were close to zero, which shows that the process of O₂ reduction was almost entirely under the diffusion control. The inset of Figure 20e compares the number of electrons involved in the ORR calculated from the K-L equation at various potentials. As shown in the inset to Figure 20e, the value of n for ORR for the PtCo/NC electrocatalyst approaches 4, indicating

direct ORR to water without any peroxide formation in this potential range [94]. Figure 20f compares the initial and 50th cycles of the CV data for the PtCo/NC and commercial Pt/C catalysts in the O₂ saturated electrolyte at 400 rpm. Evidently, the reduction in ORR performance over 50 cycles was only about 6 % (based the current density values at 0.6 V vs RHE) for the PtCo/NC whereas the Pt/C showed above 15 % under identical test conditions.

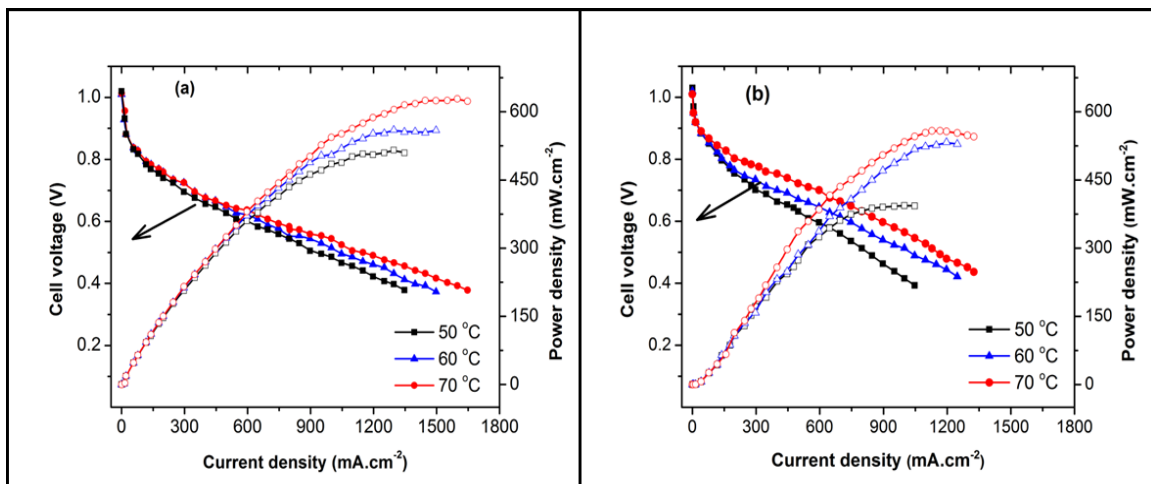


Figure 21. Fuel cell performance of (a) PtCo/NC and (b) commercial Pt/C cathode catalysts at various temperatures with H₂ and O₂ gases, 100 % RH at ambient pressure. The open symbols represent the power density values.

Figure 21a shows the PEM fuel cell performance of the MEA with PtCo/NC cathode and commercial Pt/C anode catalysts using H₂ and O₂ at various temperatures up to 70 °C. It was very encouraging to observe that the cathode with very low loading of 0.12 mg.cm⁻² showed a peak power density of 630 mW.cm⁻² at 70 °C with H₂ and O₂ gases at ambient pressure at 100 % RH. For the comparison, an MEA with commercial Pt/C based anode

and cathode and with similar Pt loading was also fabricated and evaluated. As given in Figure 21b, the peak power density is only $\sim 570 \text{ mW}\cdot\text{cm}^{-2}$ at identical test conditions. It was summarized that the relatively higher PEMFC performance of the PtCo/NC nanocatalysts was mainly due to the alloy catalyst distributed homogeneously in the NC conducting network.

2.4 Discussion for PtNiCo/NC

Figure 22a displayed the XRD patterns for simulated Co-ZIF (black), and for as prepared Co-ZIF (red) and NiCo-ZIF (blue). The simulated XRD pattern matched the recorded Co-ZIF pattern indicating the successful synthesis of Co-ZIF. When adding the Ni precursor during the synthesis, the XRD pattern remained the same but it was slightly shifted to higher 2θ degrees. This shifting explained the Ni replacing some of the Co ions in the ZIF structure and it gave a smaller d spacing due to the higher 2θ degrees.

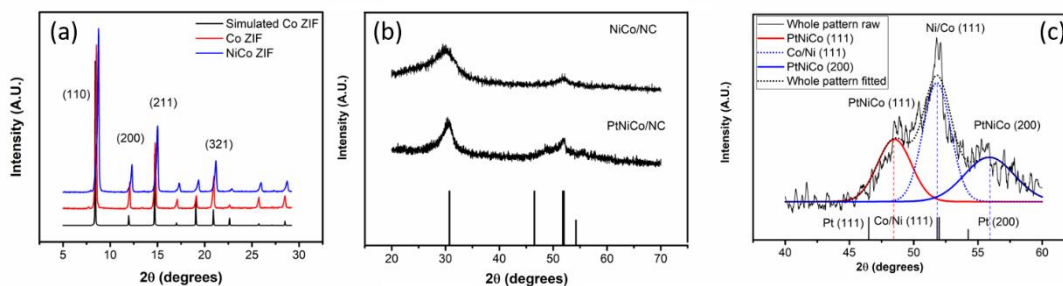


Figure 22. XRD of (a) Co ZIF (red) and NiCo ZIF (blue) along with a simulated pattern for Co ZIF (black), (b) NiCo/NC and PtNiCo/NC, and (c) high-resolution XRD looping scan for Pt, Ni, Co (111) regions.

For the pure Ni and Co metal (111) planes, the Ni has a higher diffraction angle compared to the Co at 51.830 and 51.998 2θ degrees, respectively. Figure 22b showed the XRD patterns for NiCo/NC and PtNiCo/NC. Both samples had clear graphite (002) diffraction peaks at ~ 30.72 2θ degrees, while the sample with Pt precursor had sharper/narrower diffraction peaks. These peaks indicated that the PtNiCo/NC had better crystallinity compared to the sample NiCo/NC. The NiCo/NC had a broad peak at ~ 52 2θ degrees due to the Co (111) and Ni (111) diffraction at 51.830 (PDF#15-0806) and 51.988 (PDF#65-0380) 2θ degrees. The alloys were confirmed for PtNiCo/NC by the broad diffraction peak was shifting away from 46.510 (PDF#65-2868) 2θ degrees (the pure Pt (111) plane). Figure 22c showed that the deconvoluted diffraction pattern of PtNiCo/NC had three peaks, PtNiCo (111), Ni/Co (111) and PtNiCo (200) at 48.42, 51.81 and 55.92 2θ degrees, respectively. The $\text{Pt}_{2.45}(\text{Ni/Co})$ was estimated to be the alloy formula. Also, for PtNiCo/NC sample, there were some unalloyed (Ni/Co) particles which were observed from the Ni/Co (111) diffraction. The full width half maximum (FWHM) from the deconvoluted peaks gave more information about the crystallite size. The sizes of PtNiCo and Ni/Co were estimated to be 3.1 and 3.5 nm. The diffraction peaks' positions, lattice spacings, Pt:(Ni/Co) ratios and particle sizes of PtNiCo/NC were summarized in Table 3.

Table 3. The diffraction peaks positions, lattice spacings, Pt:(Ni/Co) ratios and particle sizes of Pt, Co, Ni, PtCo and PtNiCo.

	Pt (111) PDF#65-2868	Co (111)/Ni (111) PDF#15-0806/ PDF#65-0380	PtNiCo (111)	Ni/Co (111)
Diffraction Angle (2θ degrees)	46.51	51.83/51.98	48.42	51.81
Lattice spacing (Å)	2.27	2.05/2.04	2.18	2.05
Pt: (Ni/Co) Alloy ratio	-	-	2.45	-
Scherrer FWHM estimation (nm)	-	-	3.1	3.5

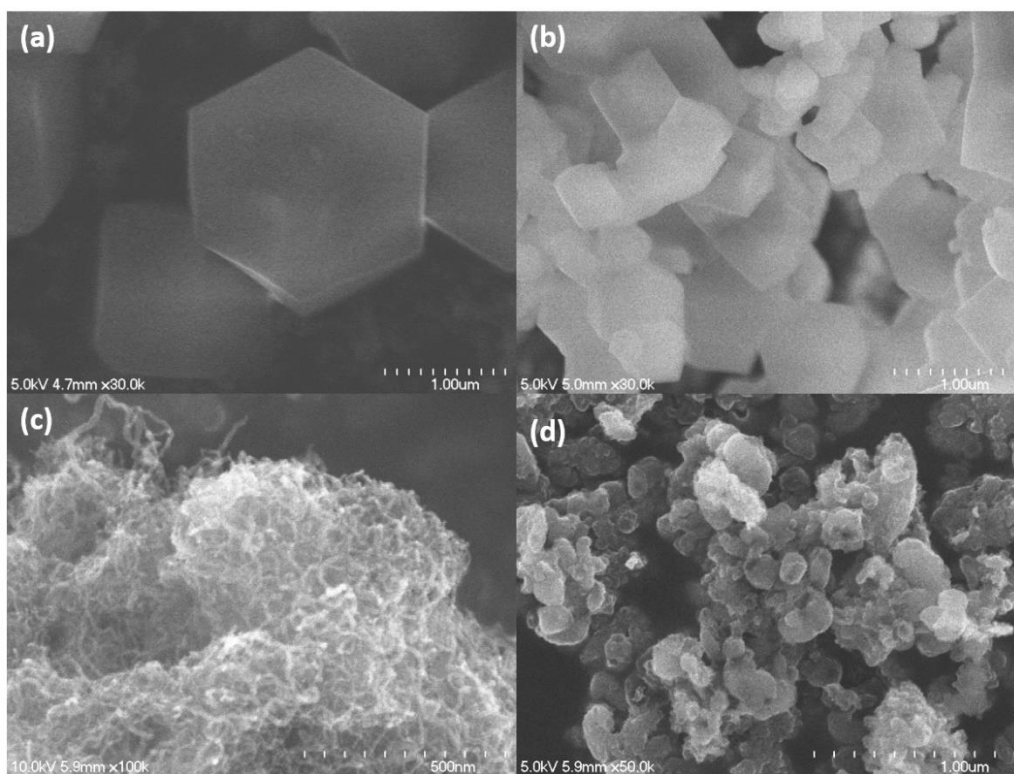


Figure 23. Morphology and structural characterization in FESEM. (a) Co-ZIF, (b) NiCo-ZIF, (c) NiCo/NC and (d) PtNiCo/NC.

Figure 23a,b show SEM of Co-ZIF and NiCo-ZIF. The size of NiCo-ZIF particles ($\sim 0.5 \mu\text{m}$) were smaller than Co-ZIF particles ($\sim 2 \mu\text{m}$). The Co-ZIF shows hexagonal based polyhedron while the NiCo-ZIF shows a cubic polyhedron. After adding the Ni precursor, the shape and particle size were changed during the solvothermal synthesis. After heat treatment and acid washing of NiCo-ZIF, the hollow structures were covered with interconnected CNTs, as shown in Figure 23c. The same observations were reported in reference [95–97]. Under Ar/H₂ environment, the Co/Ni ion was reduced by the hydrogen gas at high temperature; the Co/Ni metal acted as seeds widely spread out in the carbon-rich ZIF. In the meantime, the ZIF started to decompose by evaporating the unstable organic groups and leaving mostly carbon in the sample. The heated carbon atoms started to dissolve into the seeds under heating temperature. When the seeds became saturated with carbon atoms, the bottom-up growth started [98]. The XRD showed a broader graphite (002) peak for the PtNiCo/NC compared to the NiCo/NC. This can conclude that the CNTs were only limited on the surface of NiCo/NC because the majority of carbon was present as amorphous carbon inside the decomposed ZIF. Interestingly, no CNTs could be seen on the surface of the Pt loaded ZIF particles after the thermal treatment. The surface of the PtNiCo/NC became rougher compared to the NiCo-ZIF, and the size was also shrunk under pyrolysis (Figure 23d). The possible reason for this was due to the presence of the Pt precursor. The reduced Pt atoms tend to form an alloy with Ni/Co. The XRD showed more Pt compared to the Ni/Co, so the Ni/Co was buried into Pt and inhibited the forming of CNTs.

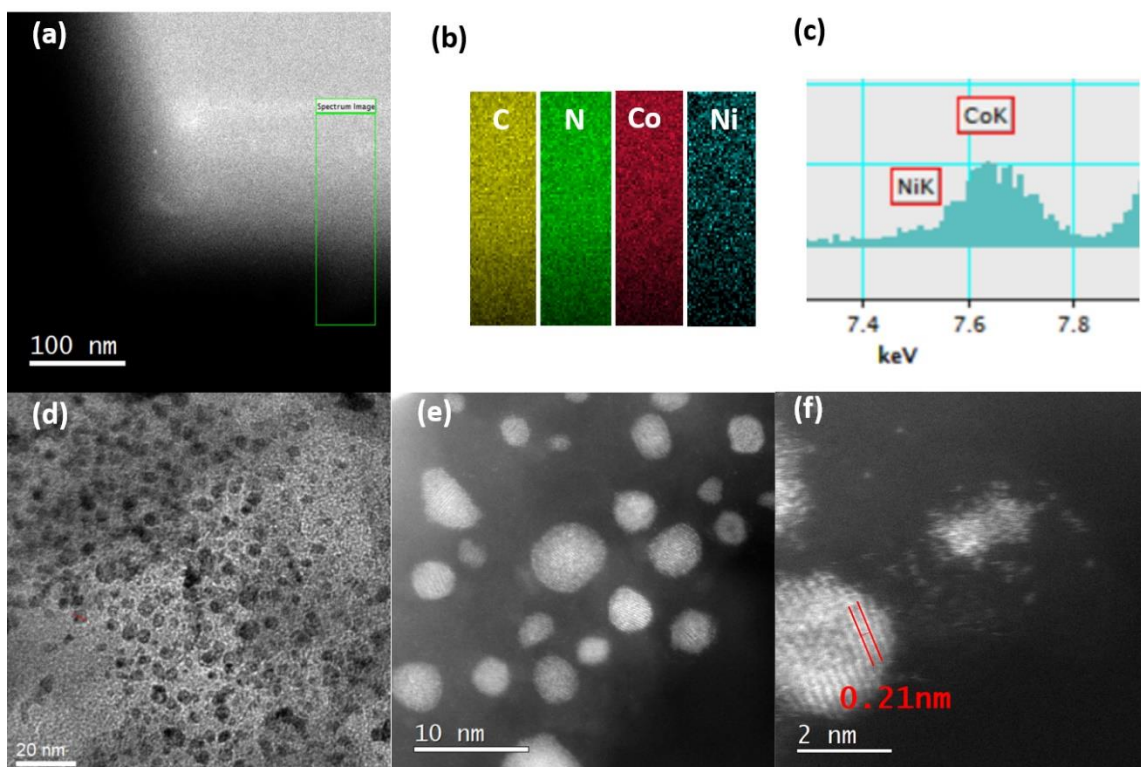


Figure 24. (a) The HAADF image of NiCo-ZIF, (b) EDS mapping of the selected area from (a), (c) EDS signal of the selected area from (a) and (c), and (d), (e), (f) TEM images of PtNiCo at various magnifications.

The HAADF image is shown in Figure 24a, the blurriness was due to the thickness of the NiCo-ZIF. In the selected area in the green box, the EDS signal was collected. The element mapping is shown in Figure 24b. C, N, Co, and Ni were well dispersed into the ZIF material and the Ni mapping was relatively sparse in the structure. The zoomed in the EDS spectrum showed Ni and Co K X-ray energy line region in Figure 24c, the Ni signal can be found but it was low compared to the Co signal. So, the EDS in the STEM also provided the evidence for the formation of the NiCo-ZIF. The well-dispersed metal/metal alloy supported by the amorphous carbon with particle size ~2-3 nm can be viewed in Figure

24d. A closer view of the PtNiCo/NC is shown in Figure 24e. The study showed that the Pt particle at around 2.2 nm was supposed to have the highest PEMFC activity [24]. The lattice spacing can be seen in Figure 24f at 0.21 nm, attribute to Pt/Ni or Co alloy (111) plane. From Table 3, the d-spacing of Pt and Ni/Co (111) plane were 0.227 and 0.204/0.205 nm, respectively. The contracting d-spacing of Pt (111) plane was also an indication for the formation of the alloy. Also, single atoms could be seen nearby the big island of atoms. The single atoms can be highly effective for catalyzing reactions, due to (1) unsaturated bonds' effects: (the unsaturated bonds increased with particle downsizing and reach the max in single atom); (2) the higher energy level of the single atom (quantum confinement) and (3) the stronger metal support interactions [23]. However, under the harsh environment in PEMFC, the single atom needs strong defects to anchor, to conquer the Ostwald ripening [99].

Table 4. Composition (atomic %) of elements in the PtNiCo/NC, estimated from the deconvoluted components in XPS data.

Element	Total (Atomic %)	Atomic % for each component				
C	94.42	52.2 (C-C)	11.7 (C-N)	5.35 (C-O)	5.2 (C=O)	26.8 ($\pi-\pi^*$)
N	0.72	43.14 (N1)	4.31 (N2)	52.55 (N3)		
O	2.57	50.00 (C=O)	50.00 (C-O)			
Co	0.18	10.40 (Co ⁰)	89.60 (Co ²⁺)			
Pt	2.11	32.62	17.76	31.65	17.97	
(PtNiCo/NC)		(Pt ⁰ 4f _{7/2})	(Pt ²⁺ 4f _{7/2})	(Pt ⁰ 4f _{5/2})	(Pt ²⁺ 4f _{5/2})	

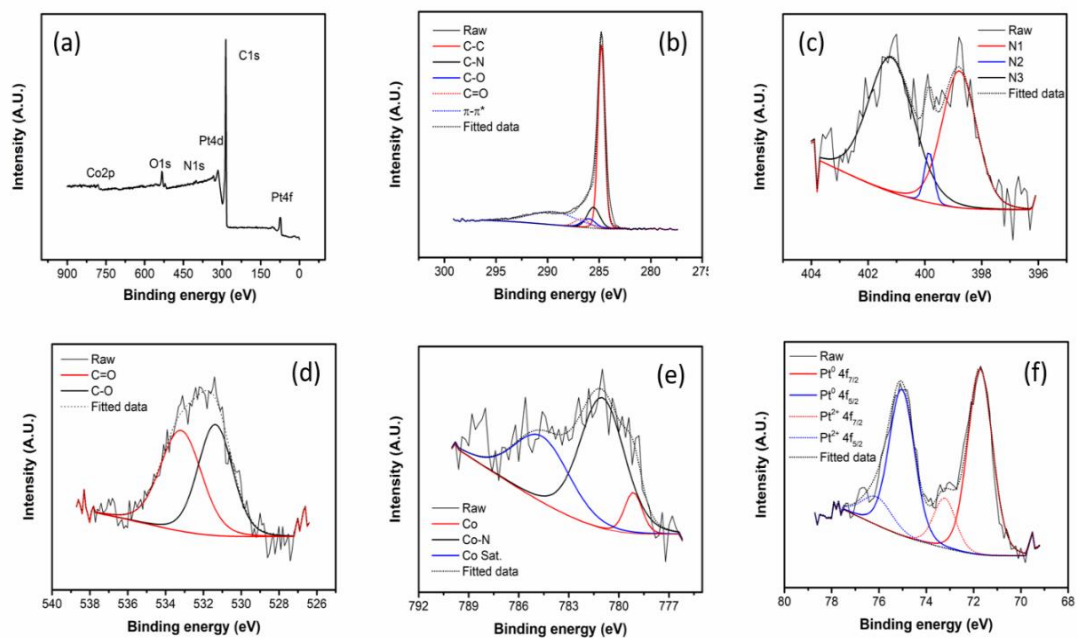


Figure 25. (a) The wide scan of XPS data and the deconvoluted high-resolution XPS scan of (b) C1s, (c) N1s, (d) O1s, (e) Co2p and (f) Pt4f for PtNiCo/NC.

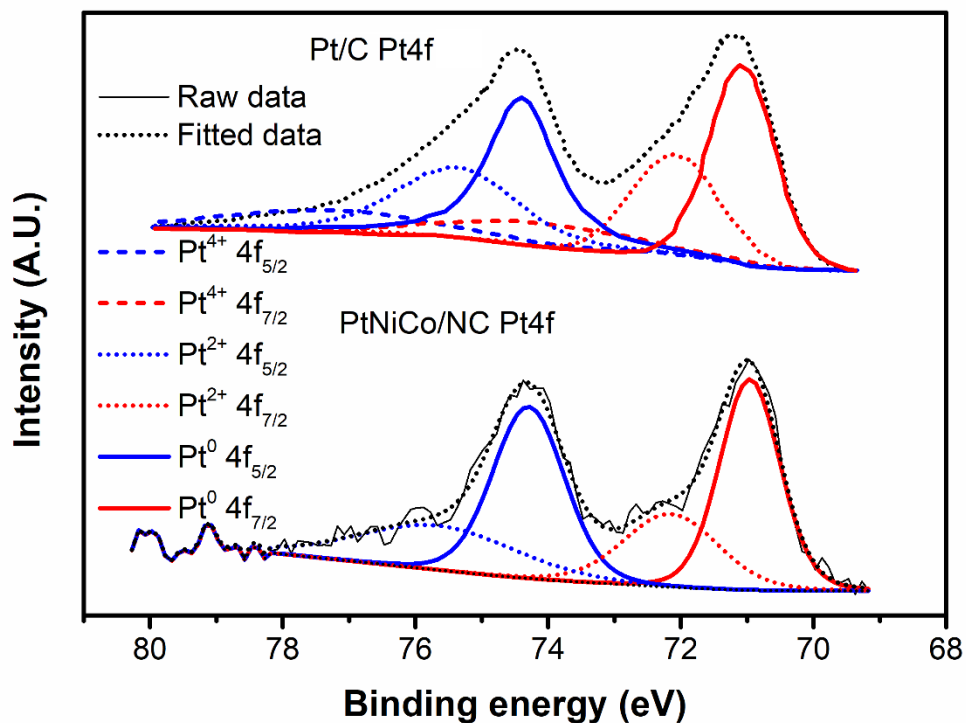


Figure 26. Comparison of Pt4f spectra of PtNiCo/NC and Pt/C from XPS

Figure 25 shows the XPS data for PtNiCo/NC. The survey scan is displayed in Figure 25a, from all the XPS peaks, there were 94.42, 0.72, 2.57, 2.11 and 0.18% of C, N, O, Pt and Co, respectively. The XPS didn't resolve Ni signal due to the at.% of Ni is less than the detecting limit. But from the ICP-MS analysis, the Pt, Ni and Co are 68.0, 0.6 and 31.4 at.%, respectively. For the detailed bonding information, the C1s high-resolution scan is shown in Figure 25b. Total five C bonding, C-C (284.8 eV), C-N (285.4 eV), C-O (286 eV), C=O (286.6 eV) and p-p* (291.3 eV) were resolved in PtNiCo/NC [100,101]. The N doping was also confirmed in Figure 25c, N1, N2 and N3 stood for the pyridinic N (398.7 ± 0.3 eV), -imine/ -amide/ -amine (399.8 ± 0.2 eV) and pyrrolic N (400.3 ± 0.2 eV) [102]. The N1, N2, and N3 were 43.14, 4.31 and 52.55 at.% from XPS surface quantification

analysis. The N1 and N3 were believed to have a positive effect on ORR [103,104]. Also, the nitrogen type determined the oxidation state of transition metal and platinum group metal [105]. O=C and O-C were deconvoluted in O1s XPS in Figure 25d, the small amount of oxygen content was due to oxidation during the pyrolysis. The defects-rich carbon support was acting as an anchor for Pt/Pt alloy particles even single Pt atoms [106,107]. Figure 25e shows the Co 2p XPS, three peaks were resolved, Co⁰(779.1 eV), Co²⁺ (781.6 eV) and Co 2p_{3/2} (785.2 eV) shake up satellite peak. The Co⁰ can be attributed to the Co and Pt alloy, the ionic Co belongs to Co-N coupling [100]. Co-N-C was also believed to act as an active site to catalyze ORR in acidic media [108]. High resolution Pt 4f XPS is shown in Figure 25f, four distinct peaks were resolved of Pt⁰ 4f_{7/2} (71.7 eV), Pt²⁺ 4f_{7/2} (73.2 eV), Pt⁰ 4f_{5/2} (75.1 eV) and Pt²⁺ 4f_{5/2} (77.6 eV) [109]. The ratio of Pt⁰ to Pt²⁺ was around 4.17:1. From the XPS data shown in Figure 26, the Pt composition for both the commercial Pt/C and PtNiCo/NC were estimated by peak quantification and is shown in Table 4. As given in Table 4, the Pt⁰ is 51 and 64 atomic % for commercial Pt/C and PtNiCo/NC, respectively [110]. Even though, the commercial Pt/C showed the presence of Pt²⁺ and Pt⁴⁺, the PtNiCo/NC catalyst only showed Pt²⁺ signals. The introduction of Ni and Co reduces the oxophilicity of Pt leading to enhanced fuel cell performance [111,112]. The Table 4 also summarized the rest atomic percentage of each element and the ratio of deconvoluted components. Overall, the XPS demonstrates the Pt and transition metal are strongly interacting with each other and the N, O functional groups on carbon support.

The electrocatalytic activity of the PtNiCo/NC is first evaluated by cyclic voltammetry (CV). As shown in Figure 27a when the HClO₄ solution is saturated with nitrogen, no redox

peak is observed. When the solution is saturated with O₂, a distinct cathodic peak is observed due to oxygen reduction. LSV measurements at different rotation rates are further conducted with a RDE set-up. The ORR performance of NiCo/NC is also evaluated by LSV. NiCo/NC shows reasonable performance at 1600 rpm as revealed by the onset potential (0.86 V vs. RHE) and current density (5.55 mA.cm⁻²). When Pt is added to these samples, the ORR activity is significantly enhanced. The PtNiCo/NC showed the best catalytic activity for the ORR as suggested by the more positive onset potential at 1600 rpm. The PtNiCo/NC is compared with the commercial Pt/C electrocatalyst for the ORR as shown in Figure 27b. At 1600 rpm PtNiCo/NC shows an onset potential of 1.03 V which is positively shifted by 50 mV compared to that of Pt/C. Figure 27b inset shows the mass activities are 7.21 and 0.108 A.mg_{pt}⁻¹ at 0.9 V vs RHE for PtNiCo/NC and Pt/C, respectively. The synergistic effect between nitrogen doped carbon, Co/Ni active sites, Pt/Pt alloy as well as single Pt atoms could be the factors for triggering exceptional ORR performance for PtNiCo/NC [113–116]. With the increase in rpm, values of current densities also increase for PtNiCo/NC (Figure 27c). The Koutecky-Levich (K-L) equation was used to analyze kinetic parameters. The linear K-L plots indicate fast reaction kinetics regarding dissolved oxygen for the potential range 0.7-0.3V and the reaction is controlled by diffusion [116,117]. The electron transfer numbers (n) at 0.7-0.3V is calculated to be in the range of ~3.97-3.98 which is the same as that of commercial Pt/C. This indicates a complete 4e⁻ ORR pathway conforming complete reduction of oxygen (Figure 27d) [118]. Table 5 provides the summary of the performance of all as prepared samples and commercial Pt/C in RDE. The PtNiCo/NC catalyst is further subjected to the CV test to determine the durability of the catalyst in acid. After 5000 CV cycles from 0.5-1.1 V,

PtNiCo/NC catalyst shows a negligible loss in performance determined by the LSV curve. In terms of halfwave potential, there is a negative shift of 15 mV at 1600 rpm compared to 30 mV for the commercial Pt/C catalyst Figure 27e, f. A comparison of Pt catalyst published by the different group is displaying in Table 6.

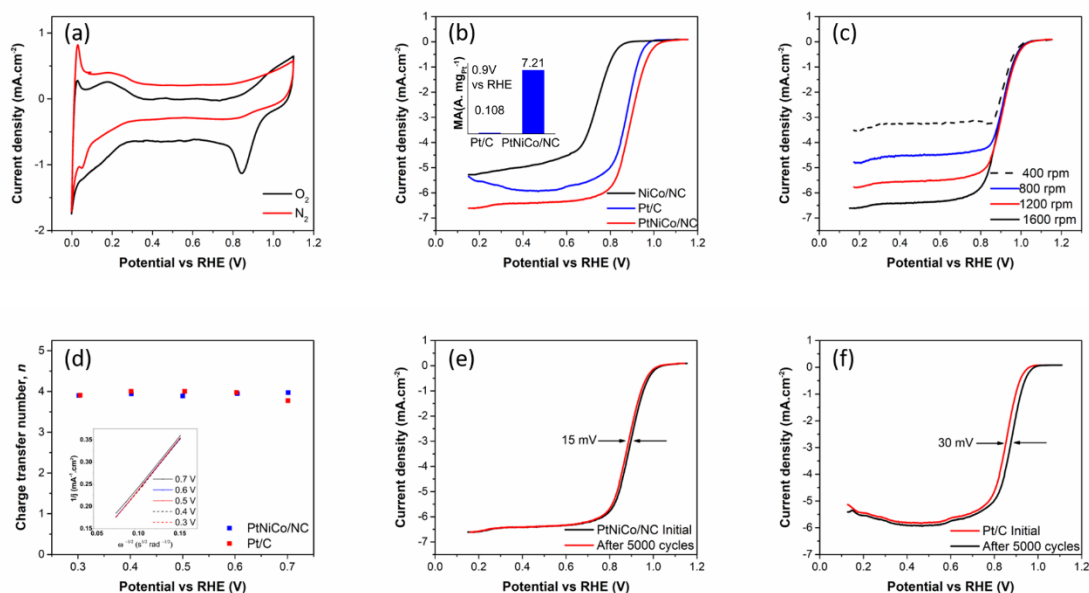


Figure 27. Electrochemical performance of (a) CV plots in N_2 (red) and O_2 (black) saturated electrolyte; (b) LSV for Co/NC (red dash), NiCo/NC (black dash), PtCo/NC (black solid), NiCo/NC (red solid) and Pt/C (blue solid) at 1600 rpm in O_2 saturated electrolyte; (c) LSV for PtNiCo/NC at different rpm in O_2 saturated electrolyte; (d) the charge transfer numbers for PtNiCo/NC (blue) and Pt/C (red) and K-L plots for PtNiCo/NC at different potential (inset); (e) LSV for PtNiCo/NC before and after durability test at 1600 rpm in O_2 saturated electrolyte; (f) LSV for Pt/C before and after durability test at 1600 rpm in O_2 saturated electrolyte. All the electrolytes were 0.1 M

$HClO_4$.

Table 5. Comparison of different as prepared samples and commercial Pt/C used as electrocatalysts for ORR in acidic medium.

Electrocatalysts	Onset Potential ^a (V vs. RHE)	Half wave Potential (V vs. RHE)	Loading	Limiting current density at 0.1V vs. RHE (mA.cm ⁻²)
PtC	0.98	0.87	25 $\mu\text{g}_{\text{Pt}}\cdot\text{cm}^{-2}$	5.50
NiCo/NC	0.86	0.76	0.7 mg.cm ⁻²	5.55
PtNiCo/NC	1.03	0.91	25 $\mu\text{g}_{\text{Pt}}\cdot\text{cm}^{-2}$	6.51

^a vs. RHE, read at current density of 0.05 mA.cm⁻² from Figure 27b

Table 6. Comparison of different Pt based electrocatalysts for ORR (1600 RPM, 0.1M HClO₄).

Electrocatalysts	Onset Potential vs RHE (V)	Halfwave Potential vs RHE (V)	Loading ($\mu\text{g}_{\text{Pt}}\cdot\text{cm}^{-2}$)	Limiting current density at 0.1V vs. RHE ($\text{mA}\cdot\text{cm}^{-2}$)	Scan rate ($\text{mV}\cdot\text{s}^{-1}$)	Reference
Pt ₁ -N/BP	0.94	0.76	24	4.8	5	[114]
Pt/Zr-C 3	0.90	-	40	5.7	10	[119]
Pt _{0.61} Ni/C	-	0.85	24	5.2	5	[120]
PtNi@Pt/C	0.95	-	12	6.0	10	[121]
PtNiCo/NC	1.05	0.91	25	6.5	20	This work

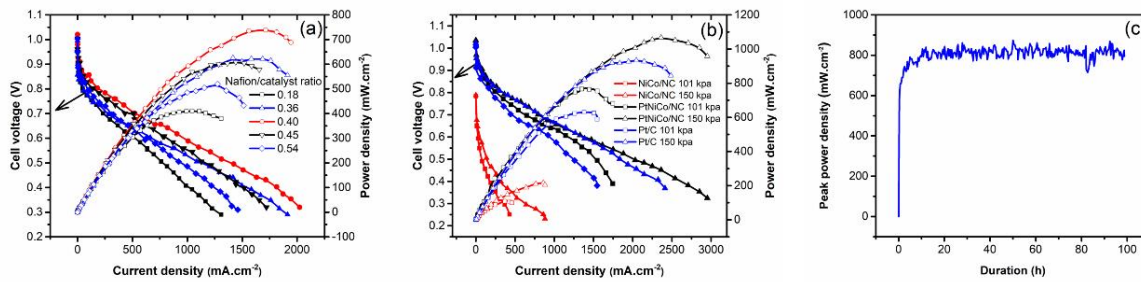


Figure 28. The PEMFC performance of (a) Nafion/catalyst ratio optimization for PtNiCo/NC, (b) MEAs with NiCo/NC, PtNiCo/NC and Pt/C with and without back pressure, and (c) the stability testing with PtNiCo/NC cathode at ambient pressure (All the data were obtained at 70 °C using H₂ and O₂ at 200 and 300 SCCM at 100 % RH with Nafion-212 electrolyte).

In order to maximize the catalyst utilization, the Nafion content in the catalyst layer was optimized and the fuel cell performance is given in Figure 28a for various ratios of Nafion to PtNiCo/NC catalyst amount at 70 °C using H₂ (200 SCCM) and O₂ (300 SCCM) gases at 100 % RH at ambient pressure. As observed from Figure 28a, the ratio of 0.4 exhibited the highest peak power density of 740 mW.cm⁻² at ambient pressure. Figure 28b compares the fuel cell performance of PtNiCo/NC cathode catalyst based MEA (optimized Nafion to catalyst ratio of 0.4) with that of NiCo/NC and commercial Pt/C at 70 °C using H₂ (200 SCCM) and O₂ (300 SCCM) gases at 100 % RH with (150 kpa) and without (101 kpa) back pressures. The cathode catalyst NiCo/NC without Pt exhibited a relatively lower peak power density of 211 mW.cm⁻². In addition, the MEA with NiCo/NC cathode catalyst also showed lower OCV (< 0.8 V) due to extremely high activation polarization associated with

the non-Pt catalyst. As expected from the RDE results (Figure 27b), the PtNiCo/NC showed the highest peak power density value of 1070 mW.cm^{-2} at 150 kpa and the commercial Pt/C led to 930 mW.cm^{-2} at 150 kpa. Evidently, the mass activity value for the PtNiCo/NC cathode catalyst is higher ($\sim 9 \text{ W.mg}_{\text{Pt}}^{-1}$) compared to that with the commercial Pt/C ($\sim 7.8 \text{ W.mg}_{\text{Pt}}^{-1}$) due to the synergistic effects of the elements in the alloy. The Pt-Ni-Co/NC cathode catalyst based MEA evaluated for 100 h at 100 % RH using H_2 and O_2 at ambient pressure showed excellent stability. As shown in Figure 28c, the peak power density values did not exhibit any performance degradation, demonstrating well anchored Pt alloy particles on the carbon support. The fluctuations are mainly due to the water management in the PEMFC single cell.

2.5 Conclusion

In the PtCo/NC, Pt nanoparticles of size $\sim 10 \text{ nm}$ were supported on the nitrogen doped carbon matrix prepared from pyrolysis of ZIF-67 (Co-ZIF) at 700°C in Ar/H_2 environment. ZIF-67 served as a single source for Co, C and N. Pt-Co alloy was confirmed on the surface of the nanostructured NC catalyst support. As evident from the RDE evaluation, the PtCo/NC nano-catalyst showed excellent performance towards ORR compared to commercial Pt/C electrocatalyst in perchloric acid. The cyclic voltammetry study showed very stable performance over 50 cycles for the PtCo/NC nano-catalyst (6 % degradation in current density) in comparison with that of the commercial Pt/C (15 %) under identical conditions. The MEA with PtCo/NC nanocatalyst showed much higher PEMFC performance with a peak power density of 630 mW.cm^{-2} compared to 563 mW.cm^{-2} by the

commercial Pt/C catalyst with same Pt loading (0.12 mg.cm^{-2}) using Nafion-212 membrane at $70 \text{ }^\circ\text{C}$ with H_2 and O_2 gases at ambient operating pressure.

This work was published in the International Journal of Hydrogen Energy.¹

In the summary of PtNiCo/NC, a highly efficient and durable catalyst were prepared, derived from NiCo-ZIF by the improved previous method. XRD showed that with the introduction of the Pt precursor, higher carbon crystallinity is obtained, to provide a higher conducting carbon matrix. By replacing Co^{2+} with Ni^{2+} in the zeolitic imidazolate frameworks, the size of ZIF particles is reduced as depicted in SEM. The Pt/Pt alloy with the size 2-3 nm as well as single Pt atoms are anchored with defects rich carbon support as confirmed by STEM and XPS. For ORR, the onset potential is 1.03 V and the value of limiting current density is 6.51 mA.cm^{-2} . The durability in acidic medium is better compared to commercial Pt/C. In single cell with PtNiCo/NC as cathode catalyst, the peak power density is 1067 mW.cm^{-2} at 150 kpa, $70 \text{ }^\circ\text{C}$ and 100% RH with H_2 and O_2 which is ~15 % increase with same Pt loading at identical conditions. A 100 h stability test showed no degradation with PtNiCo/NC MEA. These results reinforce its superiority over the traditional Pt/C catalyst in terms of ORR activity and durability.

¹ Shi, X., N. Iqbal, S. S. Kunwar, G. Wahab, H. A. Kasat, and A.M. Kannan. "**PtCo@NCNTs cathode catalyst using ZIF-67 for proton exchange membrane fuel cell.**" 43 (2018) 3520-3526.

This work is under Review in the Applied Catalysis B: Environmental.²

² Saadia Hanif, Xuan Shi, Naseem Iqbal, Tayyaba Noor, Rehan Anwar, A. M. Kannan." **ZIF derived Pt-Ni-Co/NC Cathode Catalyst for Proton Exchange Membrane Fuel Cell.**" Manuscript #: APCATB-D-19-01335 (June 2019).

CHAPTER 3

THERMAL INDUCED OV IN ALPHA MANGANESE DIOXIDE TOWARDS ORR IN ALKALINE MEDIA AND ALKALINE MEMBRANE FUEL CELL

3.1 Introduction

As mentioned in Chapter 1, the Fe/NC electrocatalyst showed good ORR activity in PEMFC testing, but the durability still does not meet industrial requirement needs yet [70]. Most of non-PGM ORR catalysts are based on Fe, Ni, Co, Cu and Mn, which tend to dissolve into the acidic electrolyte. Alkaline media provides a milder environment for those metals. The alkaline fuel cell with KOH liquid electrolyte was used for Gemini and Apollo spacecraft in the late 1960s due to better electrode kinetics in alkaline media compared to the acidic media [122]. Liquid KOH electrolyte is good for pure oxygen in the spaceship but it becomes contaminated by the CO₂ in the air, causing carbonate formation, conductivity loss, and blocking of the porous electrode [123,124]. The AMFC uses a solid polymer electrolyte membrane instead of the KOH solution, so, it has the advantages of both good kinetics in alkaline media and inert to CO₂ with air as reactant supply [125,126]. Therefore, AMFC provides more opportunities to develop and explore non-PGM electrocatalysts toward ORR [127–129].

α -MnO₂ is known about its good catalytic ability, non-toxic, low cost and abundance. OV is a defect inside the manganese dioxides crystalline materials, and it can boost the ORR performance in β -MnO₂ [51] and δ -MnO₂ [52]. Since OV effect has never been studied in α -MnO₂, the proposed experiments are to synthesize α -MnO₂ by hydrothermal method

with $\text{MnSO}_4 \cdot \text{H}_2\text{O}$ and KMnO_4 . The OV is going to introduced by post heat treatment at 300, 400 and 500 °C. The resulting products will be examined under XRD, SEM, S/TEM, XPS, RDE, and AMFC testing.

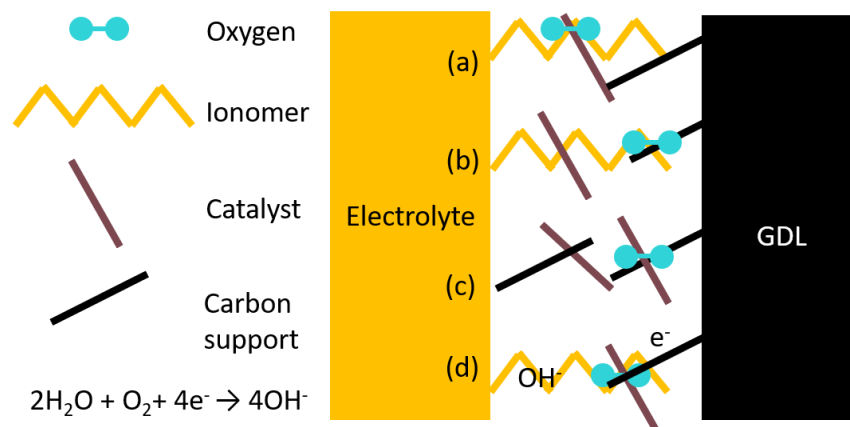


Figure 29. Oxygen at different sites of AMFC cathode $\alpha\text{-MnO}_2/\text{C}$ layer, (a) ionomer and catalyst boundary, (b) ionomer and carbon support boundary, (c) catalyst and carbon support boundary (d)ionomer, catalyst, and carbon support QPB.

$\alpha\text{-MnO}_2$ is a semiconductor which has low conductivity, so for the purpose of fuel cell studies, the highly conducting carbon support is added to improve the overall conductivity [130]. In order to enlarge the AMFC reaction zone, the ionomer is also added in the catalyst layer. In alkaline media, the oxygen reacting with water gives hydroxyl ions under suitable potential. This potential is produced by Gibbs free energy between the reactants and the product. Figure 29 shows how oxygen behaves at different sites of the AMFC cathode with a non-conducting electrocatalyst. When oxygen is at the ionomer and catalyst boundary (Figure 29a), there is no conducting material to deliver the potential and electrons to reduce the oxygen. So, at this point, the oxygen will either not be reduced or have a very slow reducing rate. When oxygen is at the boundary of ionomer and carbon support (Figure 29b),

there is no catalyst to lower the reaction barrier and the potential provided by conducting support is not enough to reduce the oxygen. Therefore, the oxygen will not be reduced at this site. When oxygen is crossing over the catalyst and carbon support boundary (Figure 29c), it is adsorbed on the catalyst active site, forming a partial bond with catalyst and lowering the reaction barrier. Under the reducing potential provided by the conducting support, the oxygen molecule reacts with nearby water molecules and forming OH^- . However, the generated OH^- cannot be delivered to the electrolyte, so the OH^- will build up in this region. Once OH^- concentration reaches a certain level, the oxygen reduction will be ceased. The maximum ORR rate can only occur at an ionomer, catalyst, carbon support and oxygen quadruple phase boundary (QPB) (Figure 29d). The generated OH^- is transferred to the electrolyte through the ionomer, then moved towards anode QPB, and finally combined with a proton to form water.

To maximize the QPB, MEAs with the different catalyst loading, carbon content and ionomer ratio were evaluated.

3.2 Experimental

3.2.1 α - MnO_2 Preparation

The α - MnO_2 samples were synthesized by the hydrothermal method in an autoclave [131]. In brief, 0.2 g of $\text{MnSO}_4 \cdot \text{H}_2\text{O}$ and 0.5 g of KMnO_4 (Sigma-Aldrich) were dissolved in 15 ml of DI water (Thermo Scientific Barnstead MicroPure, 18.2 $\text{M}\Omega \cdot \text{cm}$), then transferred into an autoclave (PARR Instrument) and heated at 140 °C for 12 hours. The precipitate was collected by centrifugation and washed thoroughly with DI water. The dark brown

precipitate was dried at 80 °C and the sample was labeled as MO. The post-heat treatments were carried out at 300, 400 and 500 °C in the air for 2 hours and the samples were labeled MO300, MO400, and MO500, respectively (Figure 30).

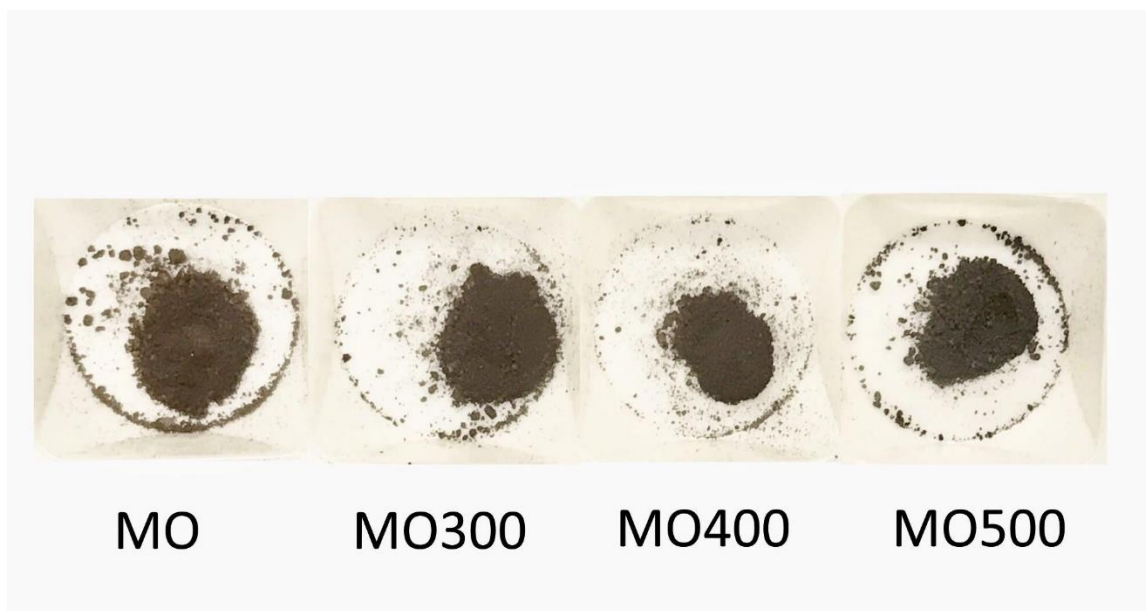


Figure 30. The picture of MO, MO300, MO400, and MO500.

3.2.2 Electrode Preparation and Testing

In order to increase the conductivity of the α -MnO₂ samples, 10 wt.% of XC72 carbon was added before ink making. The CV and durability test was only conducted with manganese dioxide film due to the different stability of different carbon support under oxidizing potential [132]. Typically, catalysts were dispersed in DI, 2-propanol and Nafion dispersion (H₂O: 2-propanol: Nafion (5 wt.% Nafion, 1100 EW, Sigma-Aldrich) = 3:1:0.016 (V: V: V)) under ultrasonic to form a 4 mg.ml⁻¹ (1 mg Pt/C per ml) slurry. Thin catalyst film was deposited by drop casting the catalyst ink onto the polished glassy carbon disk (5 mm diameter, Pine Research AFE5T050GC). The loading of α -MnO₂ and Pt on working electrodes were ~500 and ~50 μ g. cm⁻², respectively. The CV in saturated N₂ and

O₂ electrolyte for showing the redox profile purpose, ~125 μg. cm⁻² were employed on the working electrode. Uniform and well-adhered catalyst films were obtained by drying at ~50 °C for 15 min under 700 rpm.

LSV experiments were carried out in O₂ saturated 1 M KOH solution and all data were corrected by subtracting that with N₂ saturated solution. LSV experiments were conducted in the potential range of 1 to 0.2 vs RHE at 20 mV.s⁻¹ scan rate with Pt wire as counter electrode and SCE as reference electrode using PAR Bistat potentiostat at room temperature. In order to evaluate the stability of the catalyst, CV was conducted for the disk electrodes at 50 mV.s⁻¹ from 0.6 to 1.2 V vs. RHE with a 500 rpm for 500 cycles in O₂ saturated 1M KOH solution [133]. The chronoamperometry was tested at 0.8 V vs. RHE for 14 h in O₂ saturated 1M KOH solution at 400 rpm. The methanol tolerance tests were conducted in 1M KOH and 1M methanol electrolyte.

3.2.3 Materials Characterization

XRD analyses were recorded using Rigaku Ultima IV X-ray Diffractometer with Cu-Kα radiation ($\lambda = 0.154$ nm, 40 kV and 30 mA). The morphology and structure of α-MnO₂ nanorods were evaluated by FESEM (JEOL- JSM 7500F at 2keV and 3keV). The HAADF images and EELS data were characterized by JEOL ARM-200F STEM at 200keV. Mn2p and O1s XPS were recorded (Al Kα, 12 kV, Thermo Scientific, East Grinstead, UK) with surface charging correction at 284.8 eV.

Table 7. Catalyst coated membrane sample specifications.

MEA #	Carbon content (wt.%)	Ionomer (wt.%)	Anode catalyst loading (mg _{Pt} . cm ⁻²)	Cathode catalyst loading (mg.cm ⁻²)
1	10	16	0.2	1
2	10	25	0.2	2
3	20	16	0.2	2
4	20	25	0.2	1
5	20	16	0.2	3
6	30	16	0.2	2
7	40	16	0.2	2
8	50	16	0.2	2
9	30	10	0.2	2
10	30	20	0.2	2
Pt/C	54	25	0.2	0.4 mg _{Pt} . cm ⁻²

3.2.4 Catalyst Coated Membranes

For AMFC single cell testing, the CCMs with an active area of 5.0 cm² were fabricated as described below. The catalyst inks were prepared by dispersing 100 mg of commercial 46

wt.% Pt/C (Tanaka TKK, Japan) or α -MnO₂ with different carbon support (Vulcan XC72) ratios into a mixture of 3 ml methanol and 2.11 ml tetrahydrofuran (THF), followed by adding the right amount of Fumion FAA-3-10 solution (Br form). The final mixtures were repeated 3 times under 10 min sonication and vigorous agitation to obtain a homogeneously dispersed ink. The CCMs were fabricated by spraying coating 0.2 mg.cm⁻² commercial Pt/C on the anode side and the required amount of α -MnO₂/C mixture on the cathode side. During the spray coating, the electrolyte was using FAA-3-50 membrane (Br form, 50 μ m, Fumatech), with the help of hot air (50 °C) to avoid the catalyst layer cracking. The CCM was kept at room temperature \sim 30 min for membrane moisture balancing. The loadings were estimated by measuring the weight before and after the spray coating. Membrane and ionomer activations were carried out by immersing the prepared CCMs in 1M KOH overnight at room temperature to replace the Br⁻ counterions in the quaternary ammonium functional group with OH⁻ ions. Figure 31 at the left shows the tested AMFC with the membrane in OH⁻ form, and Figure 31 at the right shows a newly sprayed MEA with the membrane in Br⁻ form. The activated CCMs were thoroughly washed with DI water until the pH reached \sim 7 and stored in the DI water ready for assembly. In total, ten α -MnO₂ CCMs were made to optimize the carbon, ionomer ratio and cathode catalyst loading. A reference CCM was made by spraying Pt/C on both anode and cathode side following the procedure reported by Britton and Holdcroft [134]. The sample details are shown in Table 7. Samples #1 to #4 followed the L4 Taguchi experiment design in order to find the factor effects (FE) of carbon and ionomer ratio and catalyst loading. The detailed method description can be found in the published literature [135]. Sample #5 was used to identify optimized catalyst loading. The optimized carbon support ratio was studied through

samples #6 to #8, and the ionomer weight percentage ratio was studied through samples #9 and #10. The reference membrane (#11 CCM) with TKK Pt/C in both sides was used to compare the AMFC performance. The carbon/catalyst wt.% was calculated by the weight of the carbon/catalyst divide by the sum of carbon and catalyst. The ionomer wt.% was calculated by the weight of the ionomer divide by the sum of carbon, catalyst, and ionomer.

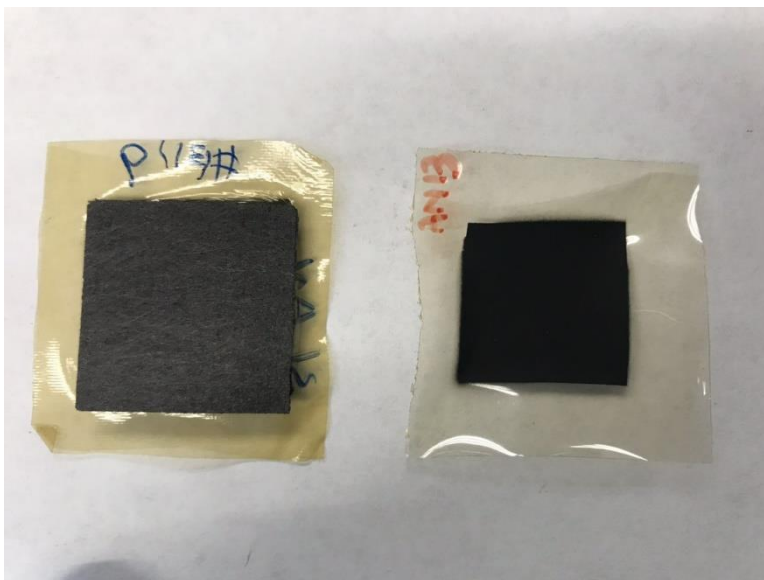


Figure 31. Tested AMFC MEA with the membrane in OH^- form (left) and newly sprayed MEA with the membrane in Br^- form (right).

3.2.5 Gas diffusion layer

The GDLs were fabricated as described in Chapter 2 (section [2.2.6](#)).

3.3 Discussion for OV in α -MnO₂

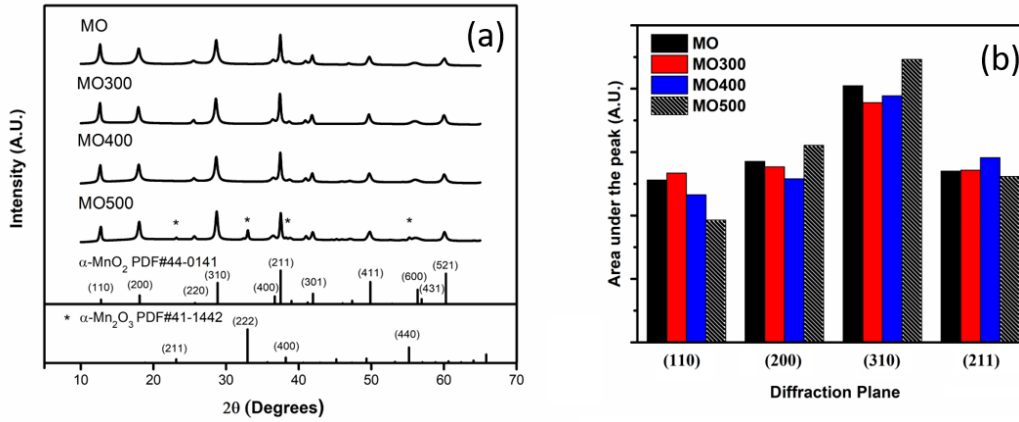


Figure 32. (a) X-ray diffractograms of MO, MO300, MO400, and MO500 samples, (b) Integrated diffraction intensity of each plane for all the samples.

The XRD patterns of the α -MnO₂ materials with and without heat treatment are shown in Figure 32a. Sharp peaks were observed on all of the samples at 2θ values of 12.75, 18.02, 28.79 and 37.45°. These correspond to the (110), (200), (310) and (211) planes (PDF# 44-0142), respectively, indicating the high crystallinity of the α -MnO₂ samples. However, after the 500 °C treatment, the α -Mn₂O₃ (PDF# 41-1442) peaks diffracted slightly at 23.13, 32.95 and 55.19°, corresponding to the (116), (222) and (440) planes, respectively, as α -MnO₂ was partially converted into α -Mn₂O₃. Under the same XRD measurement conditions, if a peak had higher integration intensity, it meant that the crystal preferred to form that certain plane [136]. To highlight the intensity of planes, Figure 32b summarizes the area under the diffraction peak on all synthesized samples. For the MO, MO300 and MO500 samples, the intensity of peaks decreased in the following order: (310) > (200) > (211) > (110). For MO400 sample, the peak intensity dropped as follows: (310) > (211) >

(200) > (110). DFT calculations showed that (211) and (310) were the first and second most active planes toward ORR, respectively [130]. In this case, (211) tended to grow on the α -MnO₂ sampled during the 400 °C treatment.

In order to study the surface morphology of the synthesized materials, SEMs were carried out (displayed in Figure 33). As seen in Figure 33a-b, the α -MnO₂ nanorods shaped with an average ~80 nm diameter, ~1 μ m length, and ~12.5 aspect ratio. Under the 300 °C heating treatment, the surfaces of α -MnO₂ nanorods (Figure 33c-d) became smoother, thinner (~70 nm in diameter) and longer (~1.5 μ m in length) with an aspect ratio of ~21.4. When the temperature increased to 400 °C (Figure 33e-f), the MO400 nanorods tended to become sharper and longer, maintaining the same diameter as MO300 with an aspect ratio of ~28. When the temperature reached 500 °C, MO500 stretched to nanowires. Even at lower magnifications, the wire ends were hard to observe (Figure 33g-h). In summary, as temperature increased, the aspect ratios also increased, and the MO samples tended to become thinner and longer.

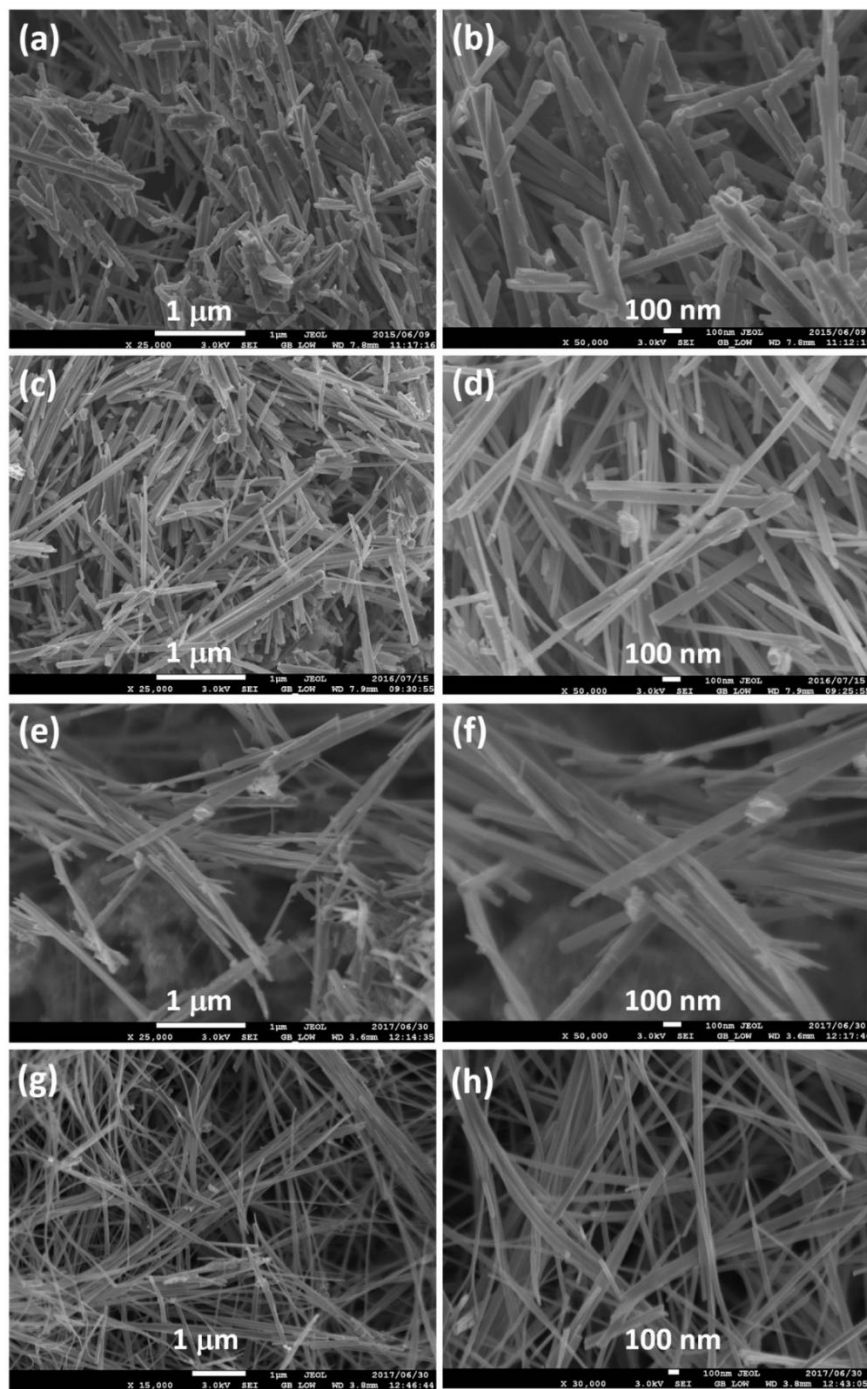


Figure 33. SEM of MO (a,b), MO300 (c,d), MO400 (e,f) and MO500 (g,h) at different magnifications.

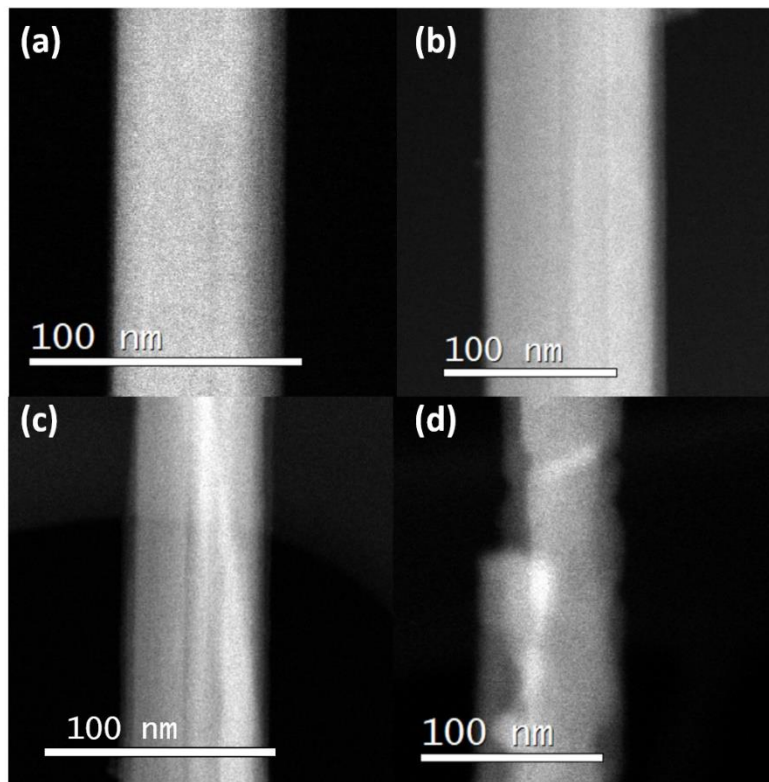


Figure 34. High angle annular dark field images of (a) MO, (b)MO300, (c) MO400 and (d) MO500.

EELS and HAADF were carried out by STEM for all four samples. Figure 34a-d shows the HAADF nanorod images for MO, MO300, MO400 and MO500, respectively. In the HAADF analysis, the darker areas in the picture indicate lower atomic densities. In this case, it can be observed from the HAADF images that the structure of α -MnO₂ nanorods collapsed as the heating temperature increased. The untreated MO (Figure 34a) sample showed smooth and uniform atomic distribution with the least defects among all four samples. At 300°C (Figure 34b), the appearance of grey lines indicated hollow channels

were forming on α -MnO₂ nanorods during the heating. Darker lines could be observed on the MO400 image (Figure 34c), indicating decreased atomic densities and hollow channels. In the MO500 sample (Figure 34d), the HAADF image showed severe damage in the nanorods. The defects on α -MnO₂ nanorods were enhanced because the form of Mn₂O₃ structures (from XRD) destroyed the inner structure of α -MnO₂ nanorods at 500°C.

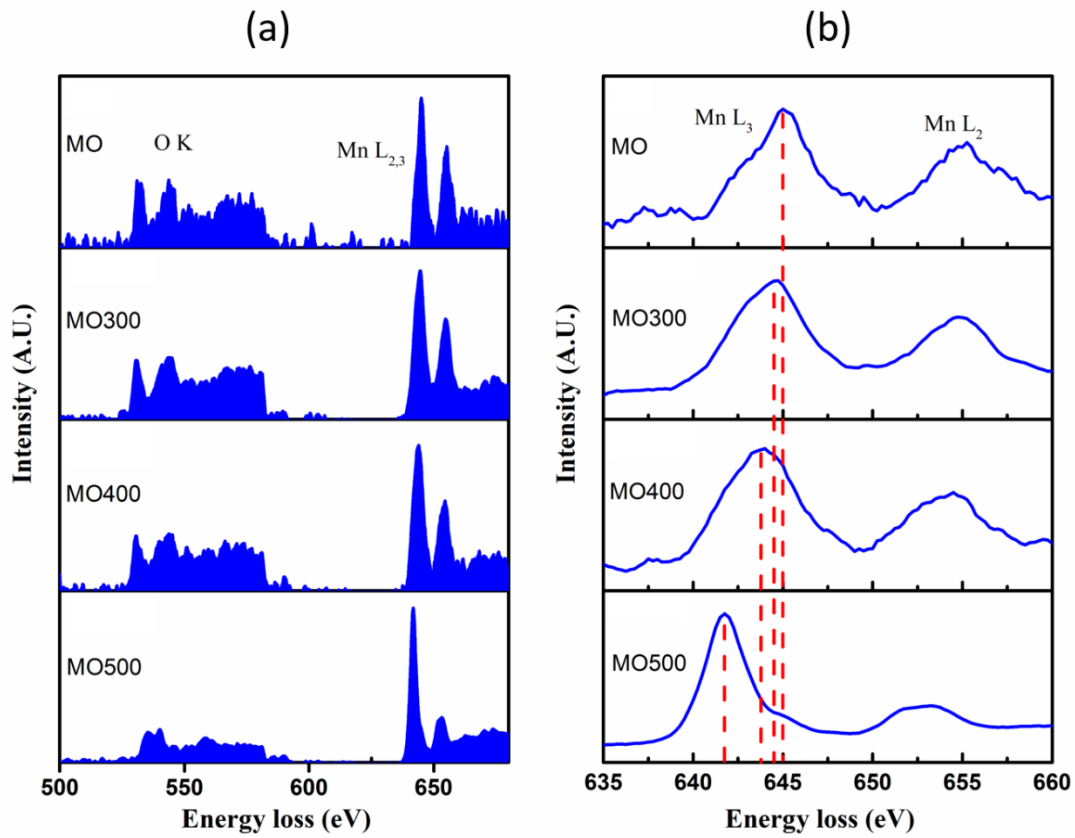


Figure 35. EELS (a) for O_K and Mn_{L_{2,3}} edges of MO, MO300, MO400, and MO500, respectively, and (b) zoomed in Mn_{L_{2,3}} edges of MO, MO300, MO400 and MO500, respectively.

When doing EELS analysis, dynamic scattering (scattering more than twice) interfered with the data interpretation. From published literature [137], the mean free path for a 200 keV energy electron in manganese oxide is ~100 nm. Based on the HAADF image, all the samples had a great chance of being single scattered, indicating that there was no interference from dynamic scattering. Figure 35 shows the results of the EELS. The oxygen K edge started at around 532 eV, corresponding to the oxygen K shell core-loss. The later signals that started at 640 eV correspond to the $Mn_{L_{2,3}}$ core-loss. The shape ranges from the oxygen threshold to the 50 eV after oxygen threshold determines the Mn oxidation state, as pointed out by Rask [138]. Since all four samples had relatively different O_K edges shapes (especially MO500), it can be seen from Figure 35a that the oxygen contents on MO300 and MO400 were slightly different from MO. There was also a huge difference observed on MO500 compared to the others. Manganese edges consisted of two major peaks. The first one started at 640 eV, corresponding to the Mn_{L_3} core-loss and the second one started around 651 eV, attributed to Mn_{L_2} . The magnified spectra of Mn loss on the samples are displayed in Figure 35b. With increasing temperature, Mn_{L_3} on α - MnO_2 materials was shifted to lower energy loss accordingly. The order of Mn_{L_3} energy loss on samples were: $MO > MO300 > MO400 > MO500$. The manganese valence was decreased (higher OV content) when the Mn_{L_3} peaks shifted to lower energy loss [138–141]. Therefore, the OV content in the manganese dioxides decreased in the following order: $MO400 > MO300 > MO$, with MO400 achieving the highest OV content. Since the MO500 had a different phase, as proved by the XRD, it could not be compared to the other samples.

To analyze OV quantity, the ratios of O and Mn intensities were calculated using Gatan DM software. In general, the hydrogenic model was accurate enough for K edges while the Hartree-Slater model was used for L edges [142]. The oxygen cross section was estimated based on the hydrogenic model, and the manganese cross-section estimation is based on the Hartree-Slater model. All the samples were calculated under the same background and signal selecting conditions using the above two models. All the samples were based on a standard criterion by setting the MO stoichiometric formula to α -MnO₂. The results of the quantitative analysis are listed in Table 8. According to analysis from Table 8, the formulas of MO300, MO400, and MO500 were α -MnO_{1.86}, α -MnO_{1.77}, and α -MnO_{1.10}, respectively. As shown in the results above, the oxygen content trend decreased as the sintering temperature increased.

Another approach to determine Mn oxidation state was from the Mn intensity ratio I(L3)/I(L2). From Table 8, the ratio of integrated intensity (area under the curve) on MO, MO300, MO400, and MO500 were 1.79, 2.04, 2.12 and 3.49. By Kurata's method, these resulted in Mn formal valences of 4.05, 3.96, 3.9 and 2.5, respectively [143]. This analysis also gave evidence that as temperature increased, the Mn formal valence decreased, and therefore OV increased. OV is a defect inside the manganese dioxides crystalline materials. The presence of OV can change the geometry, electronic structures and elongate the O–O bond of the adsorbed oxygen. Moderate OV can improve ORR performance found in β -MnO₂ and λ -MnO₂. If OV content is too high, the material changes its structure and become a different phase [52,53].

Table 8. List of intensity ratios of O/Mn and Mn $L_{3/L2}$ in all α -MnO₂ samples.

	MO	MO300	MO400	MO500
O: Mn ratio	2.0 (Mn+4)	1.86 (Mn+3.72)	1.77 (Mn+3.54)	1.10 (Mn+2.2)
I(L3)/I(L2)	1.79 (Mn+4.05)	2.04 (Mn+3.96)	2.12 (Mn+3.9)	3.49 (Mn+2.5)

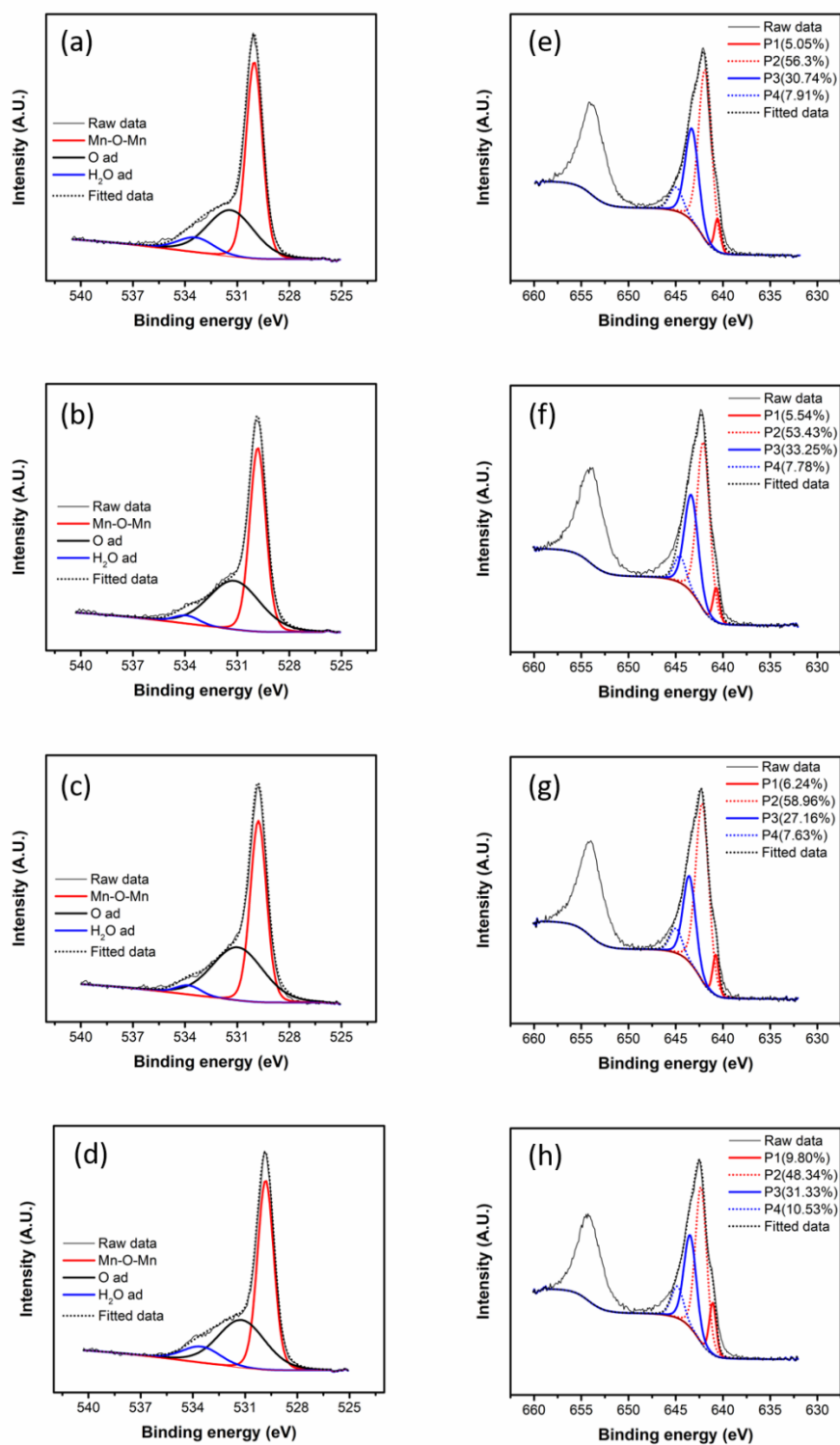


Figure 36. The deconvoluted high resolution XPS data of O1s in (a) MO, (b) MO300, (c) MO400 and Mn2p in (e) MO, (f) MO300, (g) MO400 and (h) MO500.

Figure 36 shows the deconvoluted high-resolution XPS. The O1s and Mn2p are shown in Figure 36 (a) and (e), (b) and (f), (c) and (g), (d) and (h) for MO, MO300, MO400 and MO500, respectively. The O1s (Figure 36a-d) spectra were deconvoluted into three peaks, Mn-O-Mn (529.79 eV), Mn-OH (531.26 eV) and water adsorption (533.8 eV) [144]. From the quantification analysis, the ratios of $O_{\text{latt}}/O_{\text{ad}}$ were 1.20, 1.08, 1.01 and 1.09 for MO, MO300, MO400, and MO500, respectively. The lower of the ratios indicated the stronger of manganese dioxides adsorption, which could boost the ORR [145]. The high-resolution Mn2p spectra are shown in Figure 36e-f, with the two XPS peaks attributed to Mn2p_{1/2} (654.04 eV) and Mn2p_{3/2} (642.36 eV). Since the Mn2p_{3/2} peaks had higher intensity, they were analyzed for further information. The Mn2p_{3/2} peaks were deconvoluted into four subpeaks P1 (640.80 eV), P2 (642.18 eV), P3 (643.54 eV) and P4 (645.08 eV). The P1 were found to be due to Mn³⁺ binding electrons. The percentage of P2 and P3 determined the Mn⁴⁺ ion, and the P4 were due to the satellite [146]. The P1 intensities were in an increasing order at 5.05, 5.54, 6.24 and 9.80 % for MO, MO300, MO400, and MO500, respectively. From another viewpoint, the sum of P2 and P3 decreased with the increase in heating temperature at 87.04, 86.68, 86.12, and 79.67 % for MO, MO300, MO400, and MO500, respectively. This indicated that more and more Mn⁴⁺ was reduced, with less oxygen content inside the structure when the heating temperature was increased. The quantification from the survey scan provided the chemical formula with $\alpha\text{-MnO}_2$, $\alpha\text{-MnO}_{1.98}$, $\alpha\text{-MnO}_{1.91}$, and $\alpha\text{-MnO}_{1.84}$ for MO, MO300, MO400, and MO500, respectively. The XPS quantification showed more oxygen content when compared to the EELS, due to the bulk signal from EELS and surface signal from XPS. Overall, oxygen content decreased as heating temperatures increased.

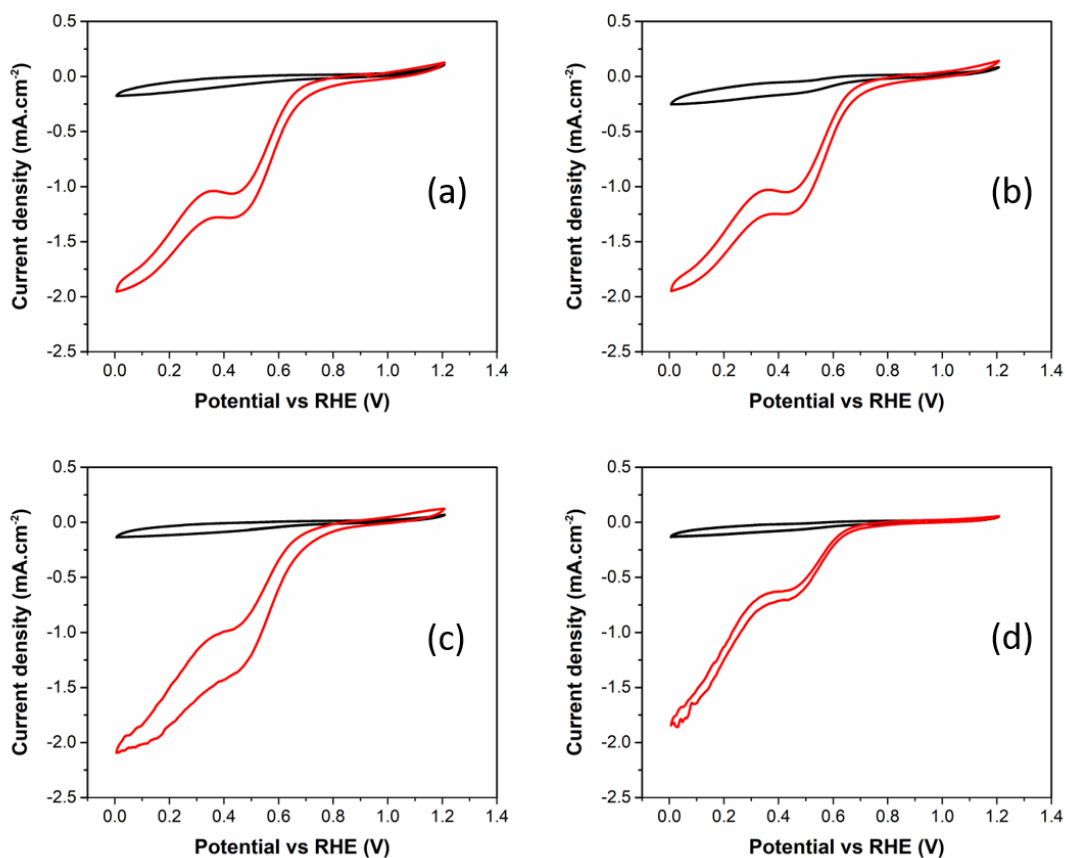


Figure 37. The O₂ (red) and N₂ (black) CV in 1M KOH electrolyte of (a) MO, (b) MO300, (c) MO400 and (d) MO500.

CV conducted in O₂ and N₂ saturated electrolyte for MO, MO300, MO400, and MO500 are shown in Figure 37a-d, respectively. The CV in N₂ (black) showed no observable redox peaks. However, the CV in the O₂ saturated electrolyte (red) showed reduction currents which belong to ORR. From the CV data in O₂, a two-step reaction mechanism was shown with two onset points. The first onset point could be attributed to eq 1.6b, eq 1.7b for a two-electron transfer process forming HO₂⁻. When more reducing potential was introduced, the as-formed HO₂⁻ was further being reduced to OH⁻ [46]. The second onset point of

MO400 started at ~ 0.45 V vs RHE, better than MO, MO300, and MO500 at 0.36, 0.37 and 0.34 V vs RHE.

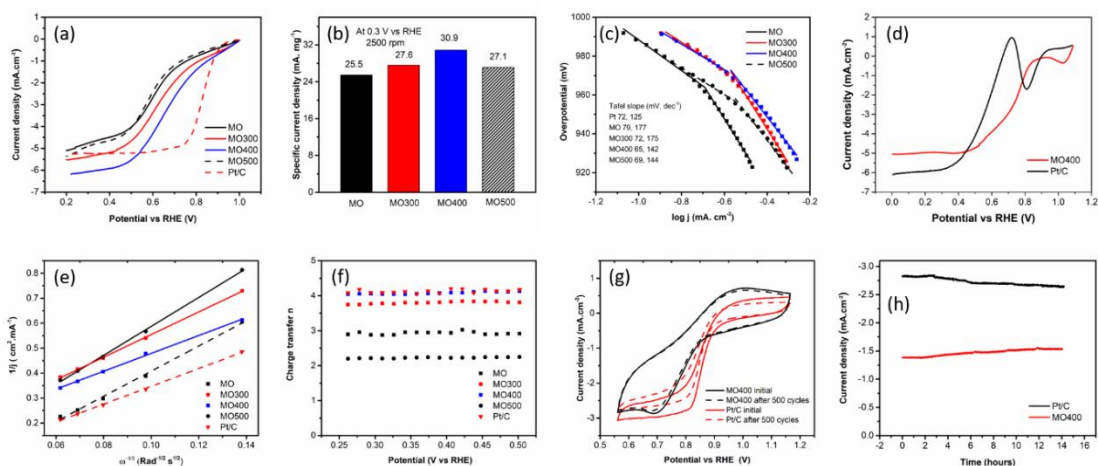


Figure 38. The electrochemical analysis of (a) LSV of MO (black), MO300 (red), MO400 (blue) MO500 (black-dash) and Pt/C (red-dash) with N_2 correction at 1600rpm, (b) specific current density at 0.3 V vs RHE, MO (black), MO300 (red), MO400 (blue), MO500 (black-white stripe), (c) Tafel slope of MO (black-solid), MO300 (red-solid), MO400 (blue-solid), MO500 (black-dash) and Pt/C (red-dash), (d) methanol tolerance in 1 M KOH and methanol electrolyte for Pt/C (black) and MO400 (red), (e) the Koutecky-Levich (K-L) plot for MO (black-solid), MO300 (red-solid), MO400 (blue-solid) MO500 (black-dash) and Pt/C (red-dash), (f) the charge transfer number estimated from K-L analysis for MO (black-square), MO300 (red-square), MO400 (blue-square), MO500 (black-circle) and Pt/C (red-triangle), (g) CV data in O_2 saturated electrolyte at 500 rpm, MO400 (red) MO400 after 500 cycles (red-dash) and Pt/C (black) Pt/C after 500 cycles (black-dash), (h) chronoamperometry for Pt/C (black) and MO400 (red).

The electrochemical properties and durability performance on α -MnO₂ and Pt/C electrodes are shown in Figure 38. The LSV of manganese oxide samples and Pt/C are shown in Figure 38a. With heating treatment up to 400 °C, the half-wave potential and limiting current were both improved at 0.60, 0.62, 0.65 and 0.59 V vs RHE and at -5.09, -5.52, -6.17 and -5.36 mA.cm⁻² for MO, MO300, MO400, and MO500, respectively. The specific current densities (Figure 38b) of MO, MO300, MO400 and MO500 at 0.3 V vs RHE were 25.5, 27.6, 30.9 and 27.1 mA.mg⁻¹, respectively. The specific current density increased with temperatures up to 400 °C and decreased at 500 °C. In addition, as displayed in Figure 38c, the Tafel slope of the kinetic current of MO400 (65 mV.dec⁻¹) was the smallest one among all samples, indicating the high ORR activity of MO400 at low overpotential [147]. Also, the value of the Tafel slope of MO400 was close to 2.303RT/F (59mV.dec⁻¹ at 25°C), in which the reaction order on MO400 was similar as Mn_xO/C under the O₂-saturated KOH solution [49] and γ -MnO₂ under the air-saturated KOH solution [148]. In the kinetic and diffusion-mixed control region, MO400 had the smallest Tafel slope at ~142 mV.dec⁻¹ as well. It was also an indicator of MO400 fast reaction kinetics towards ORR. From the XRD, XPS and EELS results, MO400 had the highest (211) diffraction peak intensity and moderate OV content among all four samples. These could be the reasons for better half-wave potential and the higher limiting currents compared to other electrodes. On the other hand, the coexistence of Mn⁴⁺ and Mn³⁺ should favor the ORR on α -MnO_x/C [49]. There was higher ORR activity when there was more Mn⁴⁺ on the surface of α -MnO_x, relative to having more Mn³⁺ species [149]. The coexistence of Mn⁴⁺/ Mn³⁺ species with a certain ratio accelerated the charge transfer to oxygen and thus favored oxygen reduction. The most favorable ratio of Mn⁴⁺/ Mn³⁺ was produced on MO400, which showed the best ORR

activity. The methanol tolerance for MO400 and Pt/C are shown in Figure 38d. The Pt/C showed a clear methanol oxidation peak at ~ 0.7 V vs. RHE but the MO400 showed no influence under 1 M methanol condition. This indicated that the MO400 was highly selective towards ORR even in methanol conditions.

The linear relationships of the K-L analysis at 0.3 V vs. RHE (Figure 38e) indicated fast kinetics for all the materials. The calculated charge transfer number from the K-L analysis for different potential are shown in Figure 38f. The region was selected from 0.25 to 0.5 V vs. RHE because the current was limited by the diffusion and displayed a stable relationship here. The charge transfer numbers (n) of ORR on MO, MO300, MO400, MO500, and Pt were calculated as around 2.9, 3.8, 4, 2.2 and 4, respectively. The oxygen reduction on a Pt/C catalyst mainly proceeds by a direct $4e^-$ pathway (eq 1.1) [46], which agreed with our result on commercial Pt/C observation. The oxygen reduction on α -MnO_x had been investigated to proceed with the first partial reaction with 2-electron (eq 1.2) followed by either the $2e^-$ reduction (eq 1.3) or the chemical disproportionation (eq 1.4) of hydrogen peroxide (HO_2^-) [49]. For the MO sample, $n=2.9$ at $E=0.3$ V vs. RHE was shown in the ORR mechanism to fall between then 2 and 4-electron pathways. As a result, the HO_2^- yield was large. The ORR on MO300 toward the 4-electron pathway (but not totally) showed $n = 3.8$, indicating that the HO_2^- yield was small. The number of electrons (n) on MO400 was 4, showing that the ORR mechanism was a 4-electron path and followed reaction routes of eq 1.5, eq 1.6a and eq 1.7a. When the temperature reached 500°C, impurities of α -Mn₂O₃ were formed. The charge transfer number was 2.2 on MO500, indicating that the oxygen reduction was towards the 2-electrons path but with HO_2^- yield.

However, with the highest content of OV in the MO500 sample, the α - MnO_2 structure deformed with the formation of the Mn_2O_3 phase leading to changes in electronic structure and adsorption energy. This was responsible for the 2-electron pathway of O_2 reduction [51].

A stability comparison was carried out for MO400 and Pt/C using CV and is shown in Figure 38g. After 500 cycles, the overpotential on Pt/C electrode increased by 12 mV at $-1 \text{ mA}\cdot\text{cm}^{-2}$ and the current density decreased by 9.5 % from -3.07 to $-2.77 \text{ mA}\cdot\text{cm}^{-2}$ at 0.6 V vs RHE on Pt/C electrode. However, the MO400 reduction current was increasing with CV cycles at the beginning. The MO400 was first cycled until the current was stable then tested consecutive 500 cycles. After 500 cycles, overpotential on MO400 electrode increased by only 6 mV at $-1 \text{ mA}\cdot\text{cm}^{-2}$ and current density decreased by 1.95 % from -2.84 to $-2.78 \text{ mA}\cdot\text{cm}^{-2}$ at 0.6 V vs. RHE. Chronoamperometry plots shown in Figure 38h compare the durability of MO400 and Pt/C based electrodes at 0.8 V vs. RHE for 14 h at 400 rpm with O_2 bubbling. Evidently, the MO400 electrode showed exceptional stability compared to the commercial Pt/C electrocatalyst.

3.4 Discussion for α -MnO₂ Cathode in Alkaline Membrane Fuel Cell

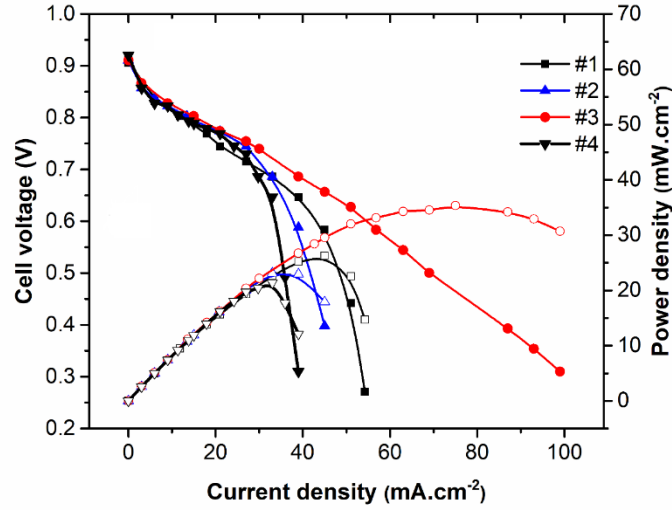


Figure 39. AMFC performance of MEA #s 1-4 (Test conditions: 50 °C using H₂ (200 SCCM) and O₂ (300 SCCM) gases at 100 % RH and ambient pressure).

Four MEAs were fabricated as per L4 Taguchi design (Table 7) to estimate the FEs of each parameter.

The FEs were calculated using eq (3.1) - (3.5) as follows:

$$\left(\frac{S}{N}\right)_i(\text{dB}) = -10 \log \left(\frac{1}{n}\right) \sum_i^n \left(\frac{1}{y_i}\right)^2 \quad (3.1)$$

$$m_j = \left(\frac{1}{N_j}\right) \sum \left(\frac{S}{N}\right)_i \quad (3.2)$$

$$\bar{m}_k = \frac{1}{N_k} \sum m_j \quad (3.3)$$

$$\text{SoS}_l = \sum (m_j - \overline{m}_k)^2 \quad (3.4)$$

$$\text{FE} = \frac{\text{SoS}}{\text{DoF} \times \sum \frac{\text{SoS}}{\text{DoF}}} \quad (3.5)$$

The signal to noise ratios (S/N) was calculated using eq (1.3), where n is the number of experiment repetitions and y_i is the peak power density (i is experiment number, in this case 1 to 4 for MEA #s 1-4). The analysis of mean m_j was determined by eq (3.2), where the index j stands for the level of parameters (low carbon content or high carbon content, etc.) and N_j stands for the number of the experiments. Eq (3.3) was used to calculate the average of the means, and the index k stands for all three parameters: carbon content, ionomer ratio, and catalyst loading. The sum of squares and the factor effect was determined by eq (3.4) and (3.5), respectively, and the index l stands for the parameters (carbon content, ionomer ratio, and cathode catalyst loading). The degree of freedom is the level of experiment minus 1; in this case, only two levels were used (high and low). The higher FE indicates this parameter has a larger influence on the peak power density of AMFC.

MEAs with MO400 as the cathodes were fabricated with different carbon and ionomer ratios. Figure 39 shows the AMFC performance of Taguchi experimental design samples (MEA #s 1-4 in Table 7). All four samples had similar OCVs around 0.91 V and the same activation and IR losses in the low current density region. However, MEA #s 1, 2 and 4 had severe concentration loss in the higher current density region. The MEA #3 was not limited by the reactant concentration and showed the highest peak power density (35.3

mW.cm⁻²) with 2 mg.cm⁻² cathodes loading and 20 wt.% and 16 wt.% carbon and ionomer content, respectively. Figure 40 shows the S/N ratio for carbon, ionomer and catalyst loadings. The low (1 in Figure 40) and high (2 in Figure 40) parameter of carbon had S/N ratio 24.69 and 28.35, respectively, with a difference of 3.65. The low and high level of ionomer had S/N ratio 30.80 and 22.24, respectively, with a difference of 8.56. The low and high level of catalyst loading had S/N ratio 29.23 and 23.80, respectively, with a difference of 5.43. The ionomer had the biggest difference in the S/N ratio indicated it influenced the performance most, then the catalyst loading was the second and carbon ratio was the last. From the calculations method published by Prakash et al. [135], the catalyst loading, carbon, and ionomer FE are 8.0%, 24.2%, and 67.8%, respectively. The higher of the FE, the higher influence of QPB.

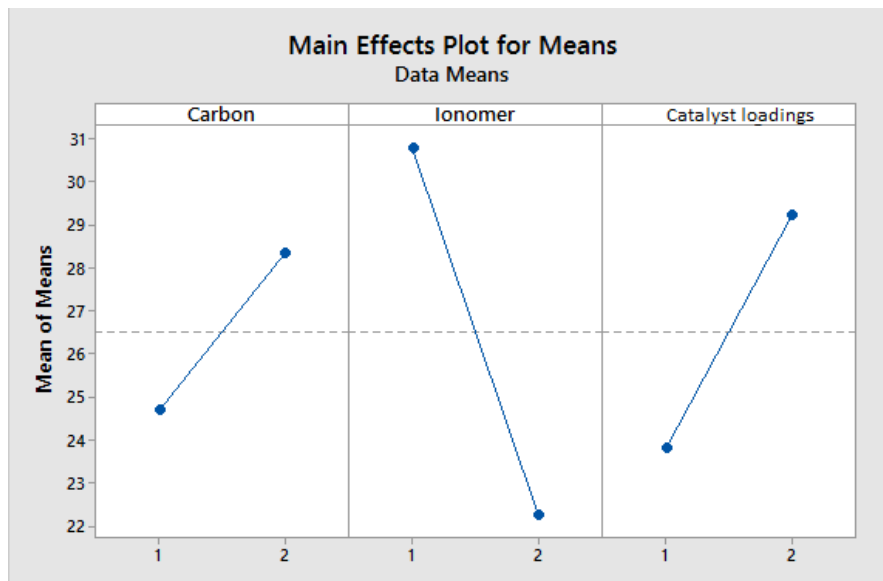


Figure 40. The main effects plot for S/N ratios for carbon, ionomer, and catalyst loadings at a different level.

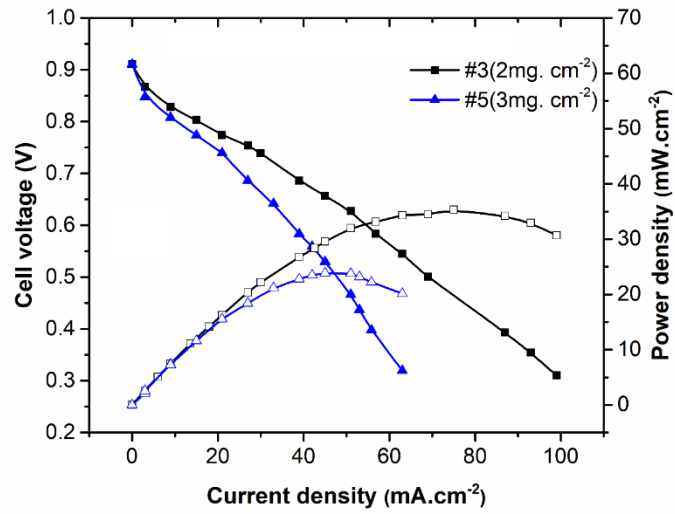


Figure 41. AMFC performance of MEAs # 3 and 5.

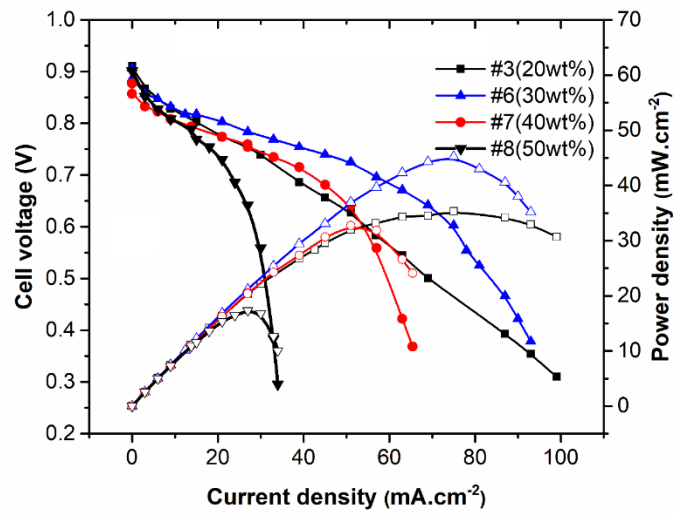


Figure 42. AMFC performance of MEA #s 3 and 6-8.

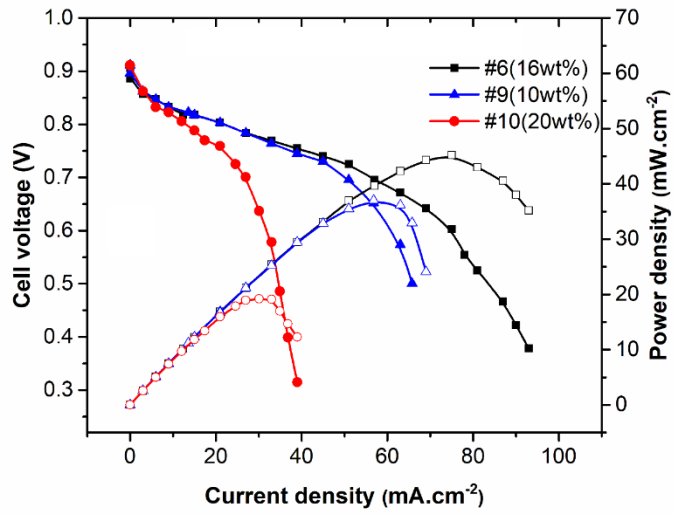


Figure 43. AMFC performance of MEA #s 6, 9 and 10.

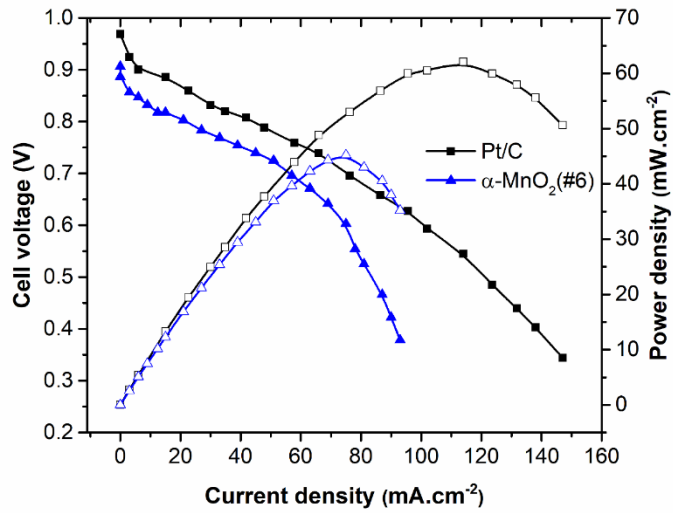


Figure 44. AMFC performance of MEA with both side Pt/C and MEA #6.

Further optimizations were carried out, in Figure 41 by spraying different amounts of catalyst (2 mg.cm^{-2} for MEA #3 and 3 mg.cm^{-2} for MEA #5). Both MEA #s 3 and 5 had

same OCV and similar activation losses as can be observed from the polarization curve. Different R_{pol} were observed at 2.457 and 2.871 Ω for MEA #s 3 and 5, respectively. The increases of IR and concentration losses were due to the thicker catalyst layer. Since α -MnO₂ has high electrical resistance, higher catalyst loading will bring more active sites for ORR. Meanwhile, it lowered the catalyst layer conductivity in the AMFC. Furthermore, it increases fuel diffuse resistance to form QPB. Different carbon contents were also evaluated (Figure 42) with 20, 30, 40 and 50 wt.% Vulcan XC72 (MEA #s 3 and 6-8, respectively). All four samples had similar OCV and activation losses. When the carbon ratio increased from 20 wt.% to 30 wt.%, a conductivity improvement was observed from the slope of IR loss region due to higher catalyst layer conductivity, and the conductivity improving can also be observed from the impedance. As carbon content increases, more diffusion resistance was introduced into the catalyst layer, so more overpotential was observed in the higher current density region. For this reason, MEA #s 7 and 8 had an excess of carbon which further decreases the peak power densities. Data from the Taguchi design suggested that ionomer had the most influence on the AMFC performances. Figure 43 shows the AMFC performance with different ionomer percentage (10 wt.% for MEA #9, 16 wt.% for MEA #6 and 20 wt.% for MEA #10). Similar OCV and activation losses were observed among all three MEAs. Compared to MEA #s 6 and 9 showed higher overpotential in the high current density region when the ionomer was decreased to 10%, which indicated that the generated OH⁻ ions cannot be transferred sufficiently to the electrolyte, thus lowering the peak power density. For MEA #10, too much ionomer decreased the conductivity (0.855, 0.198 and 1.542 Ω for MEA #s 6, 9 and 10, respectively) and covered the active sites, resulting in higher IR losses and more

overpotential in the high current density region. The optimized parameters for catalyst loadings, carbon support, and ionomer ratios were 2 mg.cm^{-2} , 30 and 16 wt.%, respectively, which corresponded to MEA #6. Figure 44 shows the AMFC performance of reference Pt/C and MEA #6. The observed OCV were ~ 0.91 and 0.97 V for the MEA #6 and Pt/C, respectively. This was consistent with the higher activation polarization observed in the LSV result. In the IR loss region, the Pt/C was more conductive compared to the MEA #6, 0.152 and $0.855 \text{ } \Omega$, respectively. In the concentration loss region, MEA #6 had more catalyst loading than Pt/C MEA. Therefore, MEA #6 showed high concentration losses. The MEA #6 showed a peak power density of $\sim 45 \text{ mW.cm}^{-2}$ compared to $\sim 60 \text{ mW.cm}^{-2}$ of commercial Pt/C catalyst. It is worth mentioning that the alkaline membrane electrolyte has more ionic resistance than proton exchange membrane electrolyte. In this case, the peak power density was heavily dependent on the thickness of the membrane. Thinner ($25 \text{ } \mu\text{m}$) membranes had higher peak power densities. However, they were not stable during activation of the polarization data collecting process. The above information is summarized in Table 9.

Table 9. Catalyst coated membrane sample with power and impedance specifications

MEA #s	Carbon content (wt.%)	Ionomer (wt.%)	Loading of anode (mg _{Pt} . cm ⁻²)	Loading of cathode (mg.cm ⁻²)	Peak power density (mW.cm ⁻²)	R _{pol} (ohm)
1	10	16	0.2	1	26.2	2.391
2	10	25	0.2	2	23.1	6.459
3	20	16	0.2	2	35.3	2.457
4	20	25	0.2	1	21.4	0.646
5	20	16	0.2	3	23.8	2.871
6	30	16	0.2	2	45.2	0.855
7	40	16	0.2	2	32.7	1.303
8	50	16	0.2	2	17.3	0.561
9	30	10	0.2	2	37.0	0.198
10	30	20	0.2	2	19.2	1.542
Pt/C	54	25	0.2	0.4 mg _{Pt} . cm ⁻²	62.0	0.152

3.5 Conclusion

Pristine α -MnO₂ nanorods were synthesized. Under various calcination temperatures (300, 400 and 500 °C), a series of α -MnO_x with different Mn valences and OV content were generated from the pristine α -MnO₂ nanorods. As the temperature increased, the α -MnO₂

nanorods tended to become longer and thinner. At 500 °C, XRD showed the presence of Mn₂O₃ impurity in α -MnO₂. The EELS spectrum and I(L3)/I(L2) methods analysis showed that the Mn state decreased as temperature increased. The XPS also showed decreasing oxygen content with increasing heating temperature. The ORR onset potential and limiting current were improved by increasing temperature up to 400 °C, and then decreasing under the 500 °C treatment due to overly high OV content and Mn₂O₃ impurities on the MO500 sample. In the stability analysis, MO400 indicated higher durability after 500 cycles and 14 h chronoamperometry than commercial Pt/C. The catalytic activity of the α -MnO_x towards ORR depended on the Mn valent state, OV content and crystal structure.

This work was published in ACS Inorganic chemistry in March 2019.³

The MO400 was fabricated as the cathode in AMFC with the different catalyst loadings, carbon and ionomer ratios. The OCV was only controlled by the catalyst type, all MO400 MEAs had same OCV and lower to the Pt/C MEA. The optimized catalyst loading, carbon support and ionomer ratio for MO400 MEAs were 2 mg.cm⁻², 30 and 16 wt.%, respectively. The FE of the catalyst loading, carbon and ionomer are 8.0%, 24.2%, and 67.8%, respectively. The ionomer had more influence on the AMFC peak power performance than carbon and loading. If the ionomer was less than 16 wt.% in the catalyst layer, the reduced OH⁻ cannot be transported efficiently to the anode and therefore restricted the overall fuel

³ Shi, X., Zheng, H., A.M. Kannan, A.M., Pérez-Salcedo, K. and Escobar, B. **Effect of Thermally Induced Oxygen Vacancy of α -MnO₂ Nanorods toward Oxygen Reduction Reaction. Inorganic Chemistry.**

cell performance. When the ionomer was more than 16 wt.%, it will block the porous electrode, introduce more electrical resistance and dilute the catalyst active sites, therefore lowering the total power. For the more than 30 wt.% carbon content, the catalyst active sites were blocked. Less than it resulted in more resistance in the catalyst layer and less QPB for ORR. The catalyst loading had a minor effect on the AMFC performance. When the loading was above the 2 mg.cm⁻², more electrical and diffusion resistant were introduced into the catalyst layer. When it was less than 2 mg.cm⁻² the active QPB was limiting the overall cell performance.

This work was published in the International Journal of Hydrogen Energy.⁴

⁴ Shi, X., Ahmad, S., Pérez-Salcedo, K., Escobar, B., Zheng, H. and A.M. Kannan. **“Maximization of quadruple phase boundary for alkaline membrane fuel cell using non-stoichiometric α -MnO₂ as cathode catalyst.”** 44(2), pp.1166-1173.

CHAPTER 4
FIRST PRINCIPLES STUDY OF THE PROTONATION EFFECT AND ACTIVE
SITES TOWARDS OXYGEN REDUCTION REACTION ON ALPHA
MANGANESE DIOXIDES (211) PLANE

4.1 Introduction

As briefly described in Chapter 1, developments of fuel cell catalysts have been limited by the lack of knowledge regarding its active sites and reaction mechanisms [74]. The modern chemical characterization techniques cannot resolve or prove the proposed mechanisms. The first principles theoretical calculation is a supplementary tool to the electrochemical method to explore the insights of ORR. With advances in computing speeds, it has become much easier to simulate materials on a bulk surface. Since the ORR is a surface catalyzed reaction, the ORR 4-electron process can be simulated by determining the adsorption and desorption energies between reactant and catalyst surface. Nørskov et al. has reported the trends in ORR as a function of both oxygen adsorption and hydroxyl ion desorption energies [22]. The adsorption and desorption energies can be defined as $E_{ad} = E_{adsorbate/catalyst} - E_{catalyst} - E_{adsorbate}$, where $E_{catalyst}$, $E_{adsorbate}$, and $E_{adsorbate/catalyst}$ are the total energies of the catalyst, adsorbate, and the combined system of catalyst and adsorbate, respectively. If E_{ad} is negative, then $E_{adsorbate/catalyst}$ is lower than the sum of $E_{catalyst}$ and $E_{adsorbate}$. Thus, adsorption will be favorable. Similarly, if E_{ad} is positive, then desorption will take place instead of adsorption [51].

In this work, the ORR on α -MnO₂ (211) plane in alkaline media is modeled in three steps. (1) α -MnO₂ is undergoing water uptake or protonation to form MnOOH. (2) The MnOOH is acting as an active site to adsorb the oxygen, (3) the oxygen is being reduced to OH⁻ and then desorbed from the surface. Due to the α -MnO₂ (211) plane contributed the most towards the ORR [130], supercells were created with (211) plane as the top surface. Based on the symmetry of the surface atom configuration, four possible sites were considered for proton adsorption, and eight positions for oxygen adsorption onto the α -MnO₂ (211) plane. In summary, 40 different structural configurations were simulated and the adsorption energies were calculated to determine the possible sites which are favorable for ORR.

4.2 Simulation and Experiment Details

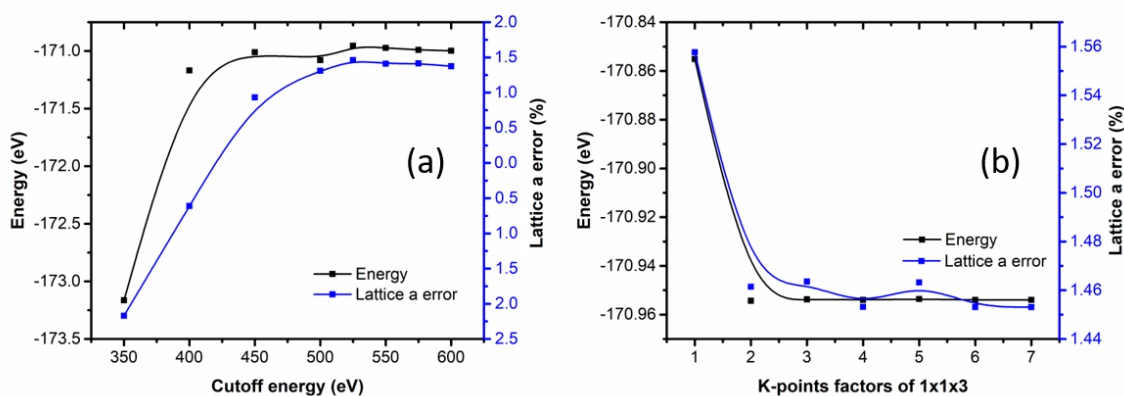


Figure 45. The total energy and the lattice constant of bulk α -MnO₂ as a function of (a) cutoff energy of planewave basis set and (b) K-points meshing of the reciprocal space.

The α -MnO₂ bulk and surface modeling were carried out using VESTA software packages. The DFT calculations including structural optimization and electronic properties were

carried out using VASP [150,151]. The Mn 3p, 4s, 3d; O 2s, 2p, and H 1s electrons were treated as valence electrons. The plane wave basis set was used in the calculations and the kinetic energy cutoff for the plane wave was scanned. Higher cutoff energy means bigger planewave basis set, thus better describes the wavefunction. However, higher cutoff energy also means higher demanding on computing resources. As shown in Figure 45a, the cutoff energies were scanned from 350 to 600 eV. The total energy of bulk α -MnO₂ and its lattice constant were calculated as a function of the energy cutoff. The calculated lattice constant was compared to its experimental value to figure out the error. The total energy (-170.95 eV) and the lattice constant error (~ 1.46 %) were stabilized at 525 eV. Therefore, the plane wave basis sets with a cutoff energy of 525 eV were used to describe the electron wavefunction. Figure 45b shows the scanning of Monkhorst-Pack K-points, the K-points started to converge at $2 \times 2 \times 6$ with -170.95 eV and 1.46 % for total energy and lattice error, respectively. The reason why K-points were scanned at multiples of $1 \times 1 \times 3$ is that the lattice constants of α -MnO₂ are $a = 9.785 \text{ \AA}$, $b = 9.785 \text{ \AA}$ and $c = 2.863 \text{ \AA}$. The general rule of the basis sets of K-points was around $1/a \times 1/c \times 1/c$. So, the reciprocal space was meshed at $2 \times 2 \times 6$ using the Monkhorst-Pack method. The convergence criteria for electronic self-consistency was set at 1×10^{-5} eV, and the ionic threshold was set at 1×10^{-4} eV. A Gaussian smearing of 0.1 eV was used for Fermi surface broadening. The DFT+U [152,153] calculation was used to improve the accuracy of the electronic property prediction for transitional metal oxides. The U value was set at 4 eV for Mn at 3d orbital [51].

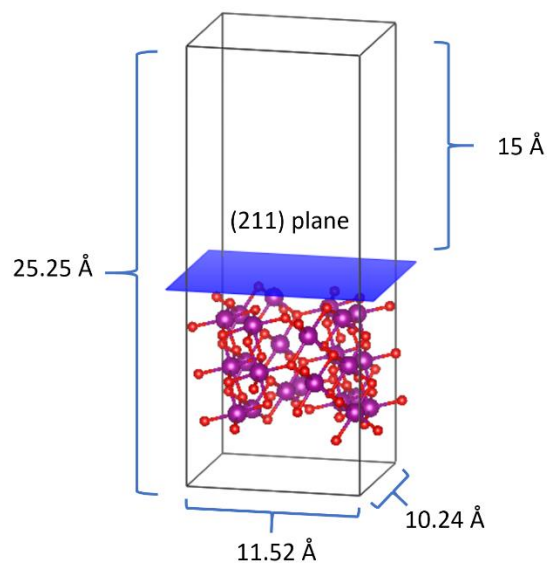


Figure 46. The model of the (211) surface of α -MnO₂. The Mn and O are shown in purple and red, respectively.

The (211) surface of α -MnO₂ is shown in Figure 46. By cleaving the (211) plane of α -MnO₂, multiple (211) surface models were created with different surface configurations. The surface energies of all the models were calculated. Figure 49 shows the (211) surface model with the lowest surface energy. A 15 Å vacuum space was added on the top of the (211) surface along with c direction to eliminate the interaction between surfaces due to the periodic boundary condition. The atoms arrangement on the top layer of the surface is shown in Figure 47. Based on the surface symmetry and atom positions, a total of eight possible sites for oxygen adsorption and four possible locations for proton insertion were considered. Figure 47a depicts the positions for oxygen (green circle with numbers), and Figure 47b displays the possible protonation sites (protons are in grey). The oxygen adsorption sites were considered at the spots between: (1) O42 and O33, (2) Mn12

and Mn15, (3) O42 and O36, (4) O33 and O45, (5) O45 and O12, (6) Mn12 and Mn9, (7) Mn9 and Mn18 and (8) Mn9 and O42.

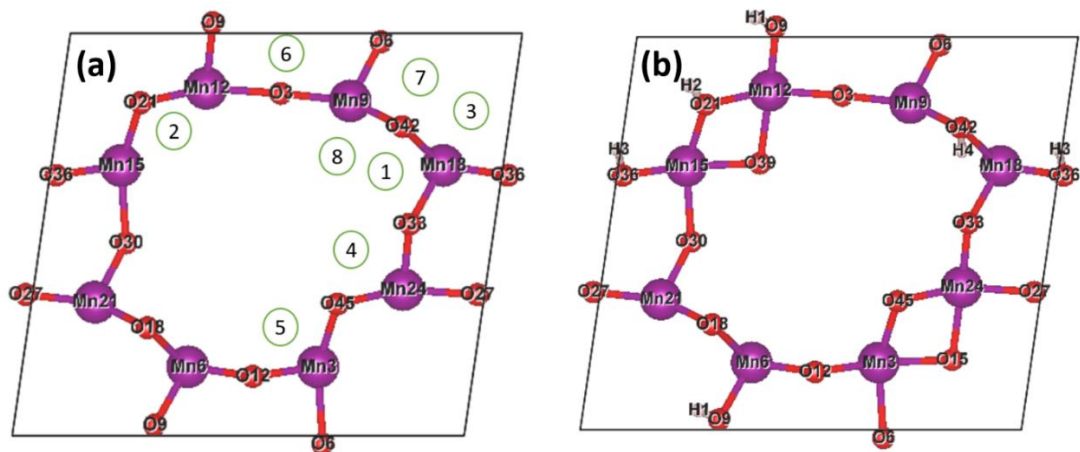


Figure 47. The schematics of the top layer atoms of α - MnO_2 (211) plane, (a) the green circle indicates the eight possible positions for oxygen adsorption, (b) four possible sites for protonation. The Mn, O and H atoms are represented using purple, red and grey balls, respectively.

The simulation of the ORR processes are summarized as below. First, bulk α - MnO_2 unit cell was calculated to obtain the optimized lattice constants. Second, the supercells of the (211) surface were built using the optimized lattice constants from the first step. Beside this clean surface, additional four surface configurations were generated by considering four different protonation sites. Third, the oxygen molecules were placed at eight different possible adsorption sites on the above mentioned five surface configurations (i.e. clean and four protonated surface configurations) and the adsorption energy was calculated for all 40 cases. Fourth, for the protonated four supercells, the desorption energies were calculated

by removing a hydroxyl ion. The energy of the hydroxyl ion was simulated by putting OH and an extra electron charge in a cubic cell with cell side length of 15 angstroms.

α -MnO₂ samples were synthesized by the hydrothermal method in an autoclave [131]. In brief, 0.2 g of MnSO₄·H₂O and 0.5 g of KMnO₄ (Sigma-Aldrich) were dissolved in 15 ml of DI water (Thermo Scientific Barnstead MicroPure, 18.2 M Ω .cm), transferred into the autoclave (PARR Instrument) and heated at 140 °C for 12 hours. The precipitate was collected by centrifugation and washed thoroughly with DI water. The dark brown precipitate was dried at 80 °C and the sample was used to do the XRD without any post heat treatment. XRD were recorded using Rigaku Ultima IV X-ray Diffractometer with Cu-K α radiation ($\lambda = 0.154$ nm, 40 kV and 30 mA).

4.3 Results and Discussion

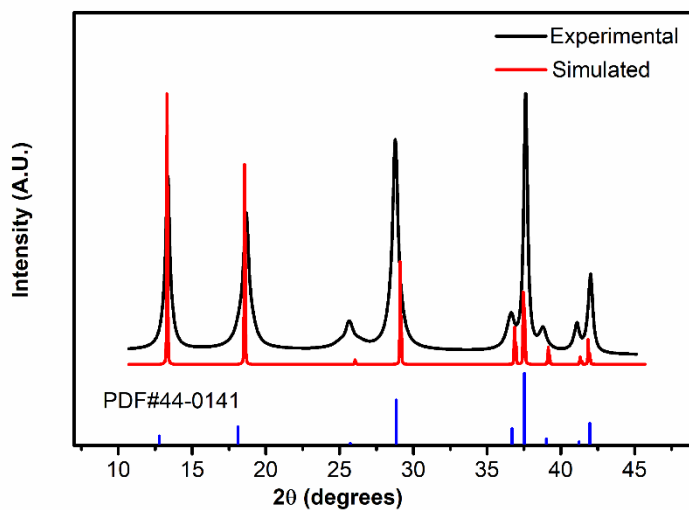


Figure 48. Experimental (black) and simulated (red) XRD of α -MnO₂.

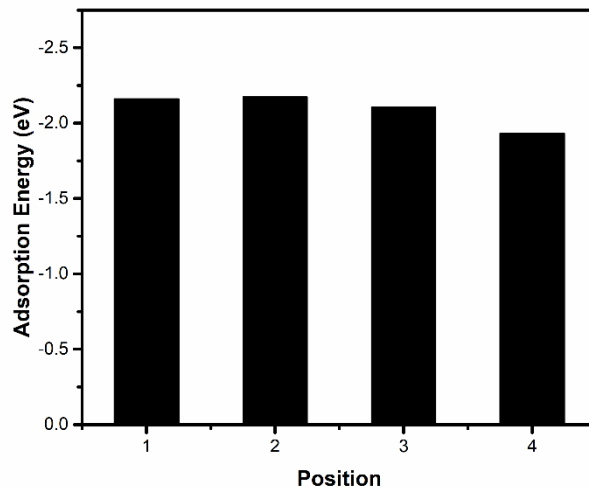


Figure 49. The adsorption energy of proton inserted surface at position 1-4.

Figure 48 shows the experimental (black) and simulated (red) XRD of α -MnO₂. Clearly, the simulated XRD was matching the experimental XRD as well as the standard powder diffraction card (PDF#44-0141). This indicated that the DFT calculation had successfully predicted the unit cell parameters and atoms positions within a reasonable error. The cutoff energy and K-points scanning in Figure 45a, b also proved the inaccuracy was $\sim 1.5\%$ when compared to the experimental data. Figure 49 shows all the proton adsorption energy on the (211) α -MnO₂ surface. The adsorption energies were -2.162, -2.175, -2.107 and -1.931 eV for protonated surfaces (PS) 1-4, respectively. The data showed that the adsorption energies of the protons were ~ 2 eV, and the protonation was preferable to form at position 2 (lowest energy).

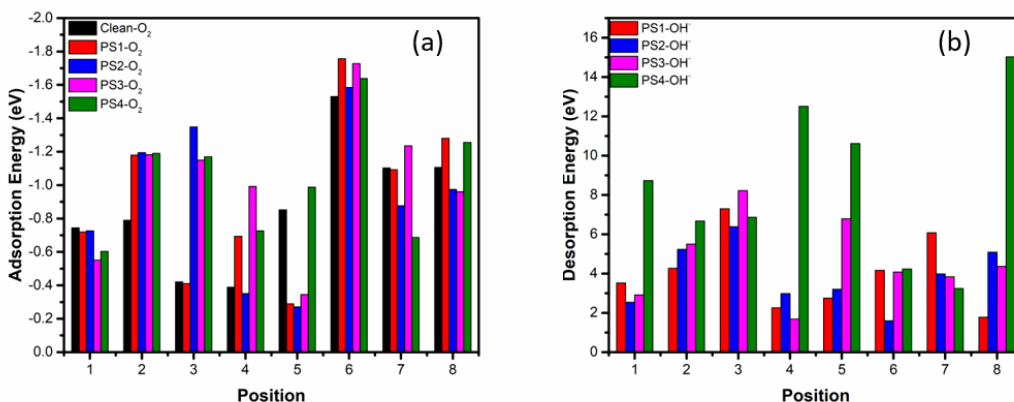


Figure 50. (a) The adsorption energies of oxygen and (b) desorption energies of hydroxyl ion on clean surface (black), position 1 PS (red), position 2 PS (blue), position 3 PS (pink) and position 4 PS (green).

Figure 50a shows all the adsorption energy of clean surface and PS. Figure 50b shows the desorption energy of all four PS (clean surfaces were not modeled in this case due to lack of H on the surface). In the ORR activity volcano plot (Figure 5), the peak ORR activities were located at ~ 1.55 - 1.95 eV and 0.98 - 1.45 eV for adsorption of oxygen and desorption energy of hydroxyl ion, respectively. In the oxygen position 1 (Figure 47), the oxygen molecule was close to the two oxygen atoms O42 and O33. The adsorption energies were -0.744 , -0.719 , -0.725 , -0.550 and -0.602 eV for the clean surface and the surface protonated at positions 1-4, respectively. In this case, the oxygen adsorption energies were far below the optimized 1.8 eV, with protonation, the adsorption was lower in all four cases (in this study, the absolute energy levels were used; when adsorption energy was lower, it means it was closer to zero). The OH⁻ desorption energies were 3.513 , 2.534 , 2.914 and 8.724 eV for PS 1-4, respectively, which were also out of suitable range. Further, the oxygen molecule was placed between Mn12 and Mn15 in oxygen position 2, and the

adsorption energies were -0.789, -1.179, -1.193, -1.182 and -1.189 eV for the clean surface and the surface protonated at the position 1-4, respectively. In this case, the oxygen was mostly influenced by the Mn d electronic structures, and all the adsorption energies were improved with protonation. The OH⁻ desorption energies were 4.264, 5.224, 5.497 and 6.667 eV for PS 1-4, respectively. In this situation, the desorption energy was out of the range as well. When the oxygen molecule was located between O42 and O36 in oxygen position 3, the adsorption energies were -0.420, -0.410, -1.348, -1.149 and -1.169 eV for the clean surface and the surface protonated at positions 1-4, respectively. In this situation, the adsorption energy of PS 1 was the same as the clean surface and the rest of the PS surfaces were all improved, especially the PS 2. The OH⁻ desorption energies were 7.292, 6.379, 8.215 and 6.859 eV for PS 1-4, respectively. In this case, the desorption energies were way above the optimized range. In the situation of where the oxygen molecule was held between O33 and O45 in oxygen position 4, the adsorption energies were -0.389, -0.693, -0.351, -0.991 and -0.726 eV for the clean surface and the surface protonated at positions 1-4, respectively. The adsorption of PS 1, 3 and 4 were improved with introducing a proton. The OH⁻ desorption energies were 2.253, 2.978, 1.676 and 12.505 eV for PS 1-4, respectively. Only PS 3 was in a suitable range for ORR. Next, when the oxygen molecule was sitting between O45 and O12 in oxygen position 5, the adsorption energies were -0.852, -0.289, -0.272, -0.345 and -0.987 eV, for the clean surface and the surface protonated at positions 1-4, respectively. In this situation, only PS 4 improved the adsorption energy. Interestingly, the adsorption energy of PS 1, 2 and 3 decreased when compared to the clean surface. The OH⁻ desorption energies were 2.747, 3.203, 6.783 and 10.609 eV for PS 1-4, respectively. All the desorption energies were too high especially in

the PS 4. Further, the oxygen molecule was placed between Mn12 and Mn9 in oxygen position 6; the adsorption energies were -1.530, -1.757, -1.585, -1.727 and -1.637 eV for the clean surface and the surface protonated at positions 1-4, respectively. In this case, the clean surface had adsorption with a good range. Furthermore, with protonation, all four cases have been improved. The OH⁻ desorption energies were 4.162, 1.595, 4.073 and 4.230 eV for PS 1-4, respectively. Only PS 3 gave the good desorption energy, and PS 1, 2 and 4 were out of suitable range. When the oxygen molecule was between Mn9 and Mn18 in oxygen position 7, the adsorption energies were -1.103, -1.092, -0.877, -1.235 and -0.686 eV for the clean surface and the surface protonated at positions 1-4, respectively. In this situation, only PS 3 adsorption increased, but others were decreased. The OH⁻ desorption energies were 6.075, 3.980, 3.831, 3.241 eV for PS 1-4, respectively, in which the ORR was restricted by the desorption. The oxygen molecule was between Mn9 and O42 in oxygen position 8, the adsorption energies were -1.106, -1.280, -0.974, -0.960 and -1.256 eV for the clean surface and the surface protonated at positions 1-4, respectively. This situation presented that PS 2 and 4 adsorption energy were improved and PS 1 and 3 were weakened when compared to the clean surface. The OH⁻ desorption energies were 1.778, 5.087, 4.361 and 15.026 eV for PS 1-4, respectively, only PS 1 was in the suitable range. The observation concluded that the protonation increased the adsorption energy of oxygen at position 2-4 and 6 for most cases. The introduced proton changed the electronic structure of adsorption sites and brought more electron affinity to the surface, resulting in strong oxygen-catalyst interaction. Furthermore, the PS 1-8, PS 2-6, and PS 3-4 showed decreases in hydroxyl ion desorption energies, which were in the good range compared to the values reported by Nørskov et al. [22]. The direct coordinates of protons in c direction

were 0.382, 0.384, 0.383 and 0.408 for protons 1 to 4, respectively. Similar c coordinates explained the PS 1-3 resulted in suitable desorption energies due to similar surface electronic structure modifications.

4.4 Conclusion

The simple ORR process in the alkaline media was simulated through three steps: (1) surface protonation, (2) oxygen adsorption and (3) hydroxyl ion desorption. The α -MnO₂ (211) planes were simulated by building supercells by cleaving the DFT optimized unit cell. On the top layer of the supercell, four possible proton insertion places and eight possible oxygen adsorption sites were defined based on the symmetry. Overall, because the protonation brought more electron affinity to the surface, the oxygen adsorptions were enhanced at the positions 2-4 and 6 for most cases. Furthermore, for the desorption energy, only PS 1-8, PS 2-6, and PS 3-4 were in the good range compared to the values reported by Nørskov et al. The possible reason was proper protonation coordinates (especially in c direction) modified the electronic structure of surface, leading decrease in desorption energies. Interestingly, the PS 4 resulted in a huge magnification in desorption energies of OH⁻ for most cases. Based on the analysis from Figure 49, PS 2 was most likely to form in nature as it had the lowest energy. This suggests that ORR would be more likely to happen on α -MnO₂ (211) plane with protonation at position 2 and oxygen adsorption at position 6 compared to other cases due to proper proton surface interaction and the Mn d orbital electronic structure influence.

CHAPTER 5

CONCLUSION

In Chapter 2, the PtCo/NC and PtNiCo/NC were prepared towards ORR in PEMFC. The PtCo/NC derived from Co-ZIF showed stable ORR performance, with ~ 6% RDE limiting current loss at 0.6 V vs. RHE compared to ~15% loss for the commercial 46 wt.% Pt/C. The LSV evaluation showed the same performance that compared to the Pt/C but with only one-third of Pt loading. The MEA with PtCo/NC as cathode showed a 10.5% increase in its peak power density at 630 mW.cm^{-2} when compared to Pt/C at 570 mW.cm^{-2} with the same amount of Pt loading on both anode and cathode. As for PtNiCo/NC, a highly efficient and durable catalyst was prepared, derived from NiCo-ZIF by improving the previous method. In XRD observations, the NiCo-ZIF was successfully synthesized. When Pt precursor was introduced in the pyrolyzed sample, a higher carbon crystallinity and the Pt alloy were confirmed. In SEM, the sizes of NiCo-ZIF were reduced compared to those of Co-ZIF. When the Pt precursor was introduced in the pyrolyzed NiCo-ZIF sample, the size of the particles was further reduced compared to the one without Pt. The PtNiCo/NC showed CNTs free surface, due to the fact that the CNTs growth was inhibited by the forming of Pt alloy. The 2-3 nm Pt/Pt alloys and single Pt atoms were anchored on defects rich carbon support which was confirmed by STEM and XPS. The LSV for PtNiCo/NC at 1600 rpm showed an onset potential of 0.95V which was 40mV more positive compared to that of Pt/C. The half-wave potential of PtNiCo/NC was only negatively shifted 15mV at 1600 rpm compared to 30mV for the commercial Pt/C after the durability test. In PEMFC

testing, the MEA with PtNiCo/NC cathode showed 700 mW.cm^{-2} peak power density which was 16.7% higher than Pt/C cathode with identical testing condition.

Pristine $\alpha\text{-MnO}_2$ nanorods were synthesized with the hydrothermal method then under various calcination temperatures (300, 400 and 500 °C). A series of $\alpha\text{-MnO}_x$ with different Mn valences and OV content were generated from the pristine $\alpha\text{-MnO}_2$ nanorods. As the temperature increases, the $\alpha\text{-MnO}_2$ nanorods tended to become longer and thinner. XRD showed the presence of Mn_2O_3 impurity in 500 °C treated $\alpha\text{-MnO}_2$. Furthermore, the quantification of the EELS spectrum and $I(L3)/I(L2)$ methods indicated that the Mn state was decreased when the temperature was increased. The XPS also showed decreasing oxygen content when heating temperatures were increased. The ORR onset potential and limiting current were both improved by increasing the heating temperature up to 400 °C. However, the performance decreased under 500 °C treatment due to excessively high OV content and Mn_2O_3 impurity in MO500 sample. The methanol tolerance testing indicated that the MO400 was highly ORR selective. In the stability analysis, MO400 showed higher durability after 500 cycles CV and 14 h chronoamperometry than commercial Pt/C. The catalytic activity of the $\alpha\text{-MnO}_x$ towards ORR depended on the Mn valent state, OV content, and crystal structure. Further, the MO400 nanorods were evaluated in the AMFC. Because the OCV was only controlled by the catalyst type, all MO400 MEAs exhibited similar OCVs, which were lower than that of the Pt/C MEA. The optimized catalyst loading, carbon support and ionomer ratio for $\alpha\text{-MnO}_2$ MEAs were 2 mg.cm^{-2} , 30 and 16 wt.%, respectively. The FE of the catalyst loading, carbon and ionomer are 8.0%, 24.2%, and 67.8%, respectively. The ionomer had more influence on the AMFC peak power

performance than the carbon content and the loading. If the ionomer was less than 16 wt.% in the catalyst layer, the reduced OH^- could not be efficiently transported to the anode, restricting the overall fuel cell performance. Also, when the ionomer was more than 16 wt.%, it blocked the porous electrode and introduced more electrical resistance, thus lowering the total power. For the MEA with more than 30 wt.% carbon content, the catalyst active sites were blocked. Less than 30 wt.% of carbon content brought more resistance in the catalyst layer and decreased the QPB for ORR. The catalyst loading had a minor effect on the AMFC performance. When the loading was above 2 mg.cm^{-2} , more electrical and diffusion resistant were introduced into the catalyst layer. When it was less than 2 mg.cm^{-2} , the active QPB limited the overall cell performance.

The simple ORR process in the alkaline media were simulated through three steps: (1) surface protonation, (2) oxygen adsorption and (3) hydroxyl ion desorption. The $\alpha\text{-MnO}_2$ (211) planes were simulated by building supercells by cleaving a DFT optimized unit cell. On the top layer of the supercell, four possible proton insertion sites and eight possible oxygen adsorption sites are defined based on symmetry. Overall, because the protonation brought more electron affinity to the surface, the oxygen adsorptions were enhanced at the positions 2-4 and 6 for most cases. Furthermore, for the desorption energy, only PS 1-8, PS 2-6, and PS 3-4 were within the good range. The possible reason was proper protonation sites (especially in c direction) modified the electronic structure of surface, leading decrease in desorption energies. Interestingly, the protonation at position 4 resulted in a huge magnification in the desorption of OH^- for most cases. Based on the analysis from proton insertion energies, PS 2 was most likely to form in nature as it had the lowest energy.

It can be concluded that the ORR will be more likely to happen on α -MnO₂ (211) plane with protonation at position 2 and oxygen adsorption at position 6 compared to other cases due to proper protonation and the Mn d orbital electronic structure influence.

In future work, both experimental and theoretical methods are crucial towards developing a new generation of electrocatalysts. Using experimental methods, Pt can also be alloyed with Fe and Co by pyrolyzing the FeCo-ZIFs, due to the close electronic properties among Fe, Co, and Ni. The results will give more insightful information to understand how Pt-Me alloy towards ORR. Also, the MeN₄ in pyrolyzed ZIFs were proposed to be the active sites for ORR. A magnetic field can separate the active sites from inert carbon support to boost fuel cell performance. Furthermore, by using theoretical methods, DFT calculations can be a supplementary tool for studying and understanding ORR on the α -MnO₂ surface. The ORR for OV imbedded α -MnO₂ can be simulated at different sites for ORR mechanism exploration.

REFERENCES

- [1] Birol F. World Energy Outlook 2018. <https://www.iea.org/weo2018/> (accessed June 25, 2019).
- [2] Energy density https://en.wikipedia.org/wiki/Energy_density (accessed June 25, 2019).
- [3] Storing Hydrogen <https://energies.airliquide.com/resources-planet-hydrogen/how-hydrogen-stored> (accessed June 25, 2019).
- [4] Birol F. World Energy Outlook 2018. <https://www.iea.org/weo/> (accessed June 25, 2019).
- [5] Wang M, Wang Z, Gong X, Guo Z. The intensification technologies to water electrolysis for hydrogen production - A review. *Renew Sustain Energy Rev* 2014;29:573–588.
- [6] Cortright RD, Davda RR, Dumesic JA. Hydrogen from catalytic reforming of biomass-derived hydrocarbons in liquid water. *Nature* 2002;418, 964–967
- [7] Hulteberg PC, Karlsson HT. A study of combined biomass gasification and electrolysis for hydrogen production. *Int J Hydrogen Energy* 2009;34:772–782.
- [8] Orfila M, Linares M, Molina R, Botas JÁ, Sanz R, Marugán J. Perovskite materials for hydrogen production by thermochemical water splitting. *Int J Hydrogen Energy* 2016;41:19329–19338.
- [9] Joy J, Mathew J, George SC. Nanomaterials for photoelectrochemical water splitting—review. *Int J Hydrogen Energy* 2018;43:4804–4817.
- [10] Dasgupta CN, Gilbert JJ, Lindblad P, Heidorn T, Borgvang SA, Skjanes K. Recent trends on the development of photobiological processes and photobioreactors for the improvement of hydrogen production. *Int J Hydrogen Energy* 2010;35:10218–10238.
- [11] Pugazhendhi A, Kumar G, Sivagurunathan P. Microbiome involved in anaerobic hydrogen producing granules: A mini review. *Biotechnol Reports* 2019;20:1-9.
- [12] FUEL CELL TECHNOLOGIES OFFICE. Hydrogen Production. <https://www.energy.gov/eere/fuelcells/hydrogen-production> (accessed June 25, 2019).
- [13] Larminie J, Dicks A, McDonald MS. Fuel cell systems explained. Chichester, UK: J. Wiley; 2003 Apr 21. p14-16.

- [14] Ahmed M, Dincer I. A review on methanol crossover in direct methanol fuel cells: challenges and achievements. *Int J Energy Res* 2011;35:1213–1228.
- [15] Ge X, Sumboja A, Wu D, An T, Li B, Goh FWT. Oxygen reduction in alkaline media: from mechanisms to recent advances of catalysts. *ACS Catal* 2015;5:4643–4667.
- [16] Cindrella L, Kannan AM, Lin JF, Saminathan K, Ho Y, Lin CW. Gas diffusion layer for proton exchange membrane fuel cells-A review. *J Power Sources* 2009;194:146–160.
- [17] James B. 2018 Cost Projections of PEM Fuel Cell Systems for Automobiles and Medium-Duty Vehicles 2018. <https://www.energy.gov/eere/fuelcells/downloads/2018-cost-projections-pem-fuel-cell-systems-automobiles-and-medium-duty> (accessed June 25, 2019).
- [18] Song C, Zhang J. Electrocatalytic oxygen reduction reaction. In *PEM fuel cell electrocatalysts and catalyst layers 2008* (pp. 89-134). Springer, London.
- [19] Sui S, Wang X, Zhou X, Su Y, Riffat S, Liu C. A comprehensive review of Pt electrocatalysts for the oxygen reduction reaction: Nanostructure, activity, mechanism and carbon support in PEM fuel cells. *J Mater Chem A* 2017;5:1808–1825.
- [20] Keith JA, Jerkiewicz G, Jacob T. Theoretical investigations of the oxygen reduction reaction on Pt (111). *ChemPhysChem* 2010;11:2779–2794.
- [21] Hyman MP, Medlin JW. Theoretical study of the adsorption and dissociation of oxygen on Pt (111) in the presence of homogeneous electric fields. *J Phys Chem B* 2005;109:6304–6310.
- [22] Nørskov JK, Rossmeisl J, Logadottir A, Lindqvist L, Lyngby D, Jo H. Origin of the Overpotential for Oxygen Reduction at a Fuel-Cell Cathode. *J Phys Chem B* 2004:17886–17892.
- [23] Liu J. Catalysis by Supported Single Metal Atoms. *ACS Catal* 2017;7:34–59.
- [24] Shao M, Peles A, Shoemaker K. Electrocatalysis on platinum nanoparticles: particle size effect on oxygen reduction reaction activity. *Nano letters*. 2011;11:3714-9.
- [25] Chen J, Lim B, Lee EP, Xia Y. Shape-controlled synthesis of platinum nanocrystals for catalytic and electrocatalytic applications. *Nano Today*. 2009;4:81-95.

- [26] Lim B, Lu X, Jiang M, Camargo PHC, Cho EC, Lee EP. Facile synthesis of highly faceted multioctahedral Pt nanocrystals through controlled overgrowth. *Nano Lett* 2008;8:4043–4047.
- [27] Fontana M, Mercier-guyon B. A Review on Recent Developments and Prospects for the Oxygen Reduction Reaction on Hollow Pt-alloy Nanoparticles. *ChemPubsoc Eur* 2018;19:1552–1567.
- [28] Pedersen AF, Ulrikkeholm ET, Escudero-Escribano M, Johansson TP, Malacrida P, Pedersen CM. Probing the nanoscale structure of the catalytically active overlayer on Pt alloys with rare earths. *Nano Energy* 2016;29:249–260.
- [29] Paulus UA, Wokaun A, Scherer GG, Schmidt TJ, Stamenkovic V, Markovic N. Oxygen reduction on high surface area Pt-based alloy catalysts in comparison to well defined smooth bulk alloy electrodes. *Electrochim Acta* 2002;47:3787–3798.
- [30] Wang C, van der Vliet D, Chang K-C, You H, Strmcnik D, Schlueter JA. Monodisperse Pt₃Co nanoparticles as a catalyst for the oxygen reduction reaction: Size-dependent activity. *J Phys Chem C* 2009;113:19365–19368.
- [31] Strasser P, Koh S, Anniyev T, Greeley J, More K, Yu C, et al. Lattice-strain control of the activity in dealloyed core–shell fuel cell catalysts. *Nat Chem* 2010;442:454.
- [32] Suo Y, Zhuang L, Lu J. First-principles considerations in the design of Pd-Alloy catalysts for oxygen reduction. *Angew Chemie* 2007;119:2920–2932.
- [33] Rudi S, Tuaeov X, Strasser P. Electrocatalytic oxygen reduction on dealloyed Pt_{1-x}Ni_x alloy nanoparticle electrocatalysts. *Electrocatalysis* 2012;3:265–273.
- [34] Gan L, Heggen M, Rudi S, Strasser P. Core–Shell Compositional Fine Structures of Dealloyed Pt_xNi_{1-x} Nanoparticles and Their Impact on Oxygen Reduction Catalysis. *Nano Lett* 2012;12:5423–5430.
- [35] Welfare H. Manganese oxide minerals: Crystal structures and economic and environmental significance. *Proc Natl Acad Sci* 1999;96:3447–3454.
- [36] Pargoletti E, Cappelletti G, Minguzzi A, Rondinini S, Leoni M. High-performance of bare and Ti-doped α -MnO₂ nanoparticles in catalyzing the Oxygen Reduction Reaction. *J Power Sources* 2016;325:116–128.
- [37] Li Y, Cao S, Fan L, Han J, Wang M, Guo R. Hybrid shells of MnO₂ nanosheets encapsulated by N-doped carbon towards nonprecious oxygen reduction reaction catalysts. *J Colloid Interface Sci* 2018;527:241–250.
- [38] Hang Y, Zhang C, Luo X, Xie Y, Xin S, Li Y. α -MnO₂ nanorods supported on

porous graphitic carbon nitride as efficient electrocatalysts for lithium-air batteries. *J Power Sources* 2018;392:15–22.

- [39] Zhang T, Neng N, Liu Z, Fisher A, Yang J. Electrochimica Acta Promotion of the bifunctional electrocatalytic oxygen activity of manganese oxides with dual-affinity phosphate. *Electrochim Acta* 2018;277:143–150.
- [40] Stoerzinger KA, Risch M, Han B, Shao-horn Y. Recent Insights into Manganese Oxides in Catalyzing Oxygen Reduction Kinetics. *ACS Catal* 2015;10:6021–6031.
- [41] Song C, Zhang J. Electrocatalytic Oxygen Reduction Reaction. PEM Fuel Cell Electrocatal. Catal. Layers, London: Springer London; 2008, p. 89–134.
- [42] Choi CH, Kwon HC, Yook S, Shin H, Kim H, Choi M. Hydrogen peroxide synthesis via enhanced two-electron oxygen reduction pathway on carbon-coated Pt surface. *J Phys Chem C* 2014;118:30063–30070.
- [43] Liu Y, Sun Q, Li W, Adair KR, Li J, Sun X. A comprehensive review on recent progress in aluminum–air batteries. *Green Energy Environ* 2017;2:246–277.
- [44] Liu J, Jiao M, Lu L, Barkholtz HM, Li Y, Wang Y, Jiang L, Wu Z, Liu DJ, Zhuang L, Ma C. High performance platinum single atom electrocatalyst for oxygen reduction reaction. *Nature communications*. 2017;8:1-9.
- [45] Schneider A, Colmenares L, Seidel YE, Jusys Z, Wickman B, Kasemo B. Transport effects in the oxygen reduction reaction on nanostructured, planar glassy carbon supported Pt/GC model electrodes. *Phys Chem Chem Phys* 2008;10:1931–1943.
- [46] Cheng F, Su Y, Liang J, Tao Z, Chen J. MnO₂-based nanostructures as catalysts for electrochemical oxygen reduction in alkaline media. *Chem Mater* 2010;22:898–905.
- [47] Mao L, Zhang D, Sotomura T, Nakatsu K, Koshiha N, Ohsaka T. Mechanistic study of the reduction of oxygen in air electrode with manganese oxides as electrocatalysts. *Electrochim Acta* 2003;48:1015–1021.
- [48] Mao L, Sotomura T, Nakatsu K, Koshiha N, Zhang D, Ohsaka T. Electrochemical characterization of catalytic activities of manganese oxides to oxygen reduction in alkaline aqueous solution. *J Electrochem Soc* 2002;149:504–517.
- [49] Roche I, Chaînet E, Chatenet M, Vondrák J. Carbon-supported manganese oxide nanoparticles as electrocatalysts for the oxygen reduction reaction (ORR) in alkaline medium: physical characterizations and ORR mechanism. *J Phys Chem C* 2007;111:1434–1443.

- [50] Cao YL, Yang HX, Ai XP, Xiao LF. The mechanism of oxygen reduction on MnO₂-catalyzed air cathode in alkaline solution. *Electroanalytical Chemistry* 2003;557:127–134.
- [51] Li L, Feng X, Nie Y, Chen S, Shi F, Xiong K. Insight into the Effect of Oxygen Vacancy Concentration on the Catalytic Performance of MnO₂. *ACS Catal* 2015;5:4825–4832.
- [52] Lee S, Nam G, Sun J, Lee JS, Lee HW, Chen W. Enhanced Intrinsic Catalytic Activity of λ -MnO₂ by Electrochemical Tuning and Oxygen Vacancy Generation. *Angew Chemie* 2016;55:8599–8604.
- [53] Ma Y, Wang R, Wang H, Key J, Ji S. Control of MnO₂ nanocrystal shape from tremella to nanobelt for enhancement of the oxygen reduction reaction activity. *J Power Sources* 2015;280:526–532.
- [54] JASINSKI R. A New Fuel Cell Cathode Catalyst. *Nature* 1964;201:1212–1223.
- [55] Wiesener K, Ohms D, Neumann V, Franke R. N₄ macrocycles as electrocatalysts for the cathodic reduction of oxygen. *Mater Chem Phys* 1989;22:457–475.
- [56] Alt H, Binder H, Sandstede G. Mechanism of the electrocatalytic reduction of oxygen on metal chelates. *J Catal* 1973;28:8–19.
- [57] Zhang L, Wilkinson DP, Liu Y, Zhang J. Progress in nanostructured (Fe or Co)/N/C non-noble metal electrocatalysts for fuel cell oxygen reduction reaction. *Electrochim Acta* 2018;262:326–336.
- [58] Van Veen JAR, van Baar JF, Kroese KJ. Effect of heat treatment on the performance of carbon-supported transition-metal chelates in the electrochemical reduction of oxygen. *J Chem Soc* 1981;77:2827–2843.
- [59] Bouwkamp-Wijnoltz AL, Visscher W, Van Veen JAR, Boellaard E, Van der Kraan AM, Tang SC. On active-site heterogeneity in pyrolyzed carbon-supported iron porphyrin catalysts for the electrochemical reduction of oxygen: an in situ Mössbauer study. *J Phys Chem B* 2002;106:12993–13001.
- [60] Yeager E. Electrocatalysts for O₂ reduction. *Electrochim Acta* 1984;29:1527–1537.
- [61] Scherson D, Tanaka AA, Gupta SL, Tryk D, Fierro C, Holze R. Transition metal macrocycles supported on high area carbon: Pyrolysis—mass spectrometry studies. *Electrochim Acta* 1986;31:1247–1258.
- [62] Scherson DA, Gupta SL, Fierro C, Yeager EB, Kordesch ME, Eldridge J. Cobalt tetramethoxyphenyl porphyrin—emission Mossbauer spectroscopy and O₂

- reduction electrochemical studies. *Electrochim Acta* 1983;28:1205–1209.
- [63] Wiesener K. N₄-chelates as electrocatalyst for cathodic oxygen reduction. *Electrochim Acta* 1986;31:1073–1078.
- [64] Franke R, Ohms D, Wiesener K. Investigation of the influence of thermal treatment on the properties of carbon materials modified by N₄-chelates for the reduction of oxygen in acidic media. *J Electroanal Chem Interfacial Electrochem* 1989;260:63–73.
- [65] Gouerec P, Biloul A, Contamin O, Scarbeck G, Savy M, Riga J. Oxygen reduction in acid media catalyzed by heat treated cobalt tetraazaannulene supported on an active charcoal: correlations between the performances after longevity tests and the active site configuration as seen by XPS and ToF-SIMS. *J Electroanal Chem* 1997;422:61–75.
- [66] Gouerec P, Bilou A, Contamin O, Scarbeck G, Savy M, Barbe JM. Dioxygen reduction electrocatalysis in acidic media: effect of peripheral ligand substitution on cobalt tetraphenylporphyrin. *J Electroanal Chem* 1995;398:67–75.
- [67] Charreteur F, Jaouen F, Ruggeri S, Dodelet J-P. Fe/N/C non-precious catalysts for PEM fuel cells: Influence of the structural parameters of pristine commercial carbon blacks on their activity for oxygen reduction. *Electrochim Acta* 2008;53:2925–2938.
- [68] Lefevre M, Dodelet JP, Bertrand P. O₂ reduction in PEM fuel cells: activity and active site structural information for catalysts obtained by the pyrolysis at high temperature of Fe precursors. *J Phys Chem B* 2000;104:11238–11247.
- [69] Lefèvre M, Dodelet JP, Bertrand P. Molecular oxygen reduction in PEM fuel cells: evidence for the simultaneous presence of two active sites in Fe-based catalysts. *J Phys Chem B* 2002;106:8705–8713.
- [70] Proietti E, Jaouen F, Lefèvre M, Larouche N, Tian J, Herranz J. Iron-based cathode catalyst with enhanced power density in polymer electrolyte membrane fuel cells. *Nat Commun* 2011;2:416–425.
- [71] Chokai M, Daidou T, Nabae Y. Development of Pt-Free Carbon-Based Catalyst for PEFC Cathode Prepared from Polyacrylonitrile. *ECS Trans* 2014;64:261–270.
- [72] Wang Y-C, Lai Y-J, Song L, Zhou Z-Y, Liu J-G, Wang Q. S-Doping of an Fe/N/C ORR Catalyst for Polymer Electrolyte Membrane Fuel Cells with High Power Density. *Angew Chemie Int Ed* 2015;54:9907–9910.
- [73] Macauley N, Lujan RW, Spornjak D, Hussey DS, Jacobson DL, More K. Durability of Polymer Electrolyte Membrane Fuel Cells Operated at Subfreezing

- Temperatures. *J Electrochem Soc* 2016;163:1317–1329.
- [74] Singh SK, Takeyasu K, Nakamura J. Active Sites and Mechanism of Oxygen Reduction Reaction Electrocatalysis on Nitrogen-Doped Carbon Materials. *Adv Mater* 2018;1804297:1–17.
- [75] Parr RG. Density functional theory of atoms and molecules. In *Horizons of Quantum Chemistry*, Springer, Dordrecht. 1980:5-15.
- [76] Jones RO, Gunnarsson O. The density functional formalism, its applications and prospects. *Reviews of Modern Physics*. 1989;61:689-746.
- [77] Perdew JP, Chevary JA, Vosko SH, Jackson KA, Pederson MR, Singh DJ. Atoms, molecules, solids, and surfaces: Applications of the generalized gradient approximation for exchange and correlation. *Phys Rev B* 1992;46:6671-6679.
- [78] Perdew JP, Wang Y. Pair-distribution function and its coupling-constant average for the spin-polarized electron gas. *Phys Rev B* 1997;56:7018-7025.
- [79] Liu B, Shioyama H, Akita T, Xu Q. Metal-organic framework as a template for porous carbon synthesis. *J Am Chem Soc* 2008;130:5390–5401.
- [80] Wang C, Liu D, Lin W. Metal-organic frameworks as a tunable platform for designing functional molecular materials. *J Am Chem Soc* 2013;135:13222–13234.
- [81] Mainar AR, Colmenares LC, Leonet O, Alcaide F, Iruiñ JJ, Weinberger S. Manganese oxide catalysts for secondary zinc air batteries: from electrocatalytic activity to bifunctional air electrode performance. *Electrochim Acta* 2016;217:80–91.
- [82] Yu P, Pemberton M, Plasse P. PtCo/C cathode catalyst for improved durability in PEMFCs. *J Power Sources* 2005;144:11–20.
- [83] Ulrikkeholm ET, Pedersen AF, Vej-Hansen UG, Escudero-Escribano M, Stephens IEL, Friebel D. Pt_xGd alloy formation on Pt (111): Preparation and structural characterization. *Surf Sci* 2016;652:114–122.
- [84] Yaghi OM, O’keeffe M, Ockwig NW, Chae HK, Eddaoudi M, Kim J. Reticular synthesis and the design of new materials. *Nature* 2003;423:705.
- [85] Xia BY, Yan Y, Li N, Wu H Bin, Lou XWD, Wang X. A metal–organic framework-derived bifunctional oxygen electrocatalyst. *Nat Energy* 2016;1:1-8.
- [86] Shinozaki K, Zack JW, Richards RM, Pivovar BS, Kocha SS. Oxygen reduction reaction measurements on platinum electrocatalysts utilizing rotating disk

- electrode technique. Impact of impurities, measurement protocols and applied corrections. *J Electrochem Soc* 2015;162:1144–1158.
- [87] Butler IB, Schoonen MAA, Rickard DT. Removal of dissolved oxygen from water: a comparison of four common techniques. *Talanta* 1994;41:211–225.
- [88] Yurekli K, Mitchell CA, Krishnamoorti R. Small-angle neutron scattering from surfactant-assisted aqueous dispersions of carbon nanotubes. *J Am Chem Soc* 2004;126:9902–9913.
- [89] Yu J, Grossiord N, Koning CE, Loos J. Controlling the dispersion of multi-wall carbon nanotubes in aqueous surfactant solution. *Carbon* 2007;45:618–623.
- [90] Lin JF, Liu X, Adame A, Villacorta R, Wertz J, Ahmad R. Development of gas diffusion layer using water based carbon slurry for proton exchange membrane fuel cells. *Electrochim Acta* 2011;56:1591–1606.
- [91] Xia BY, Yan Y, Li N, Wu H Bin, Lou XW (David), Wang X. A metal–organic framework-derived bifunctional oxygen electrocatalyst. *Nat Energy* 2016;1:1-9.
- [92] Wang D, Xin HL, Hovden R, Wang H, Yu Y, Muller DA. Structurally ordered intermetallic platinum–cobalt core–shell nanoparticles with enhanced activity and stability as oxygen reduction electrocatalysts. *Nat Mater* 2013;12:81-92.
- [93] Wang G-H, Hilgert J, Richter FH, Wang F, Bongard H-J, Spliethoff B. Platinum–cobalt bimetallic nanoparticles in hollow carbon nanospheres for hydrogenolysis of 5-hydroxymethylfurfural. *Nat Mater* 2014;13:293-302.
- [94] Kocha SS, Zack J, Neyerlin KC, Pivovar BS. Influence of nafion on the Electrochemical Activity of Pt-based Electrocatalysts. *The Electrochemical Society*; 2012;13:1269-1276.
- [95] Hu M, Reboul J, Furukawa S, Torad NL, Ji Q, Srinivasu P. Direct carbonization of Al-based porous coordination polymer for synthesis of nanoporous carbon. *J Am Chem Soc* 2012;134:2864–2867.
- [96] Sun JK, Xu Q. Functional materials derived from open framework templates/precursors: Synthesis and applications. *Energy Environ Sci* 2014;7:2071–2100.
- [97] Xia BY, Yan Y, Li N, Wu H Bin, Lou XWD, Wang X. A metal-organic framework-derived bifunctional oxygen electrocatalyst. *Nat Energy* 2016;1:1-9.
- [98] Keun J, Jung H, Lee J, Yong S, Jin J, Seok W. Metal-free CNTs grown on glass substrate by microwave PECVD. *Current Applied Physics* 2010;10:447–450.

- [99] Ferreira PJ, Shao-Horn Y, Morgan D, Holby EF, Sheng WC, Chen S. Instability of Supported Platinum Nanoparticles in Low-Temperature Fuel Cells. *Top Catal* 2007;46:285–305.
- [100] Su C, Cheng H, Li W, Liu Z, Li N, Hou Z. Atomic Modulation of FeCo–Nitrogen–Carbon Bifunctional Oxygen Electrodes for Rechargeable and Flexible All-Solid-State Zinc –Air Battery. *Advanced Energy Materials* 2017;13:1–12.
- [101] Shchukarev A, Korolkov D. XPS study of group IA carbonates. *Open Chem* 2004;2:347–362.
- [102] Pietrzak R. XPS study and physico-chemical properties of nitrogen-enriched microporous activated carbon from high volatile bituminous coal 2009;88:1871–1877.
- [103] Luo E, Xiao M, Ge J, Liu C, Xing W. Selectively doping pyridinic and pyrrolic nitrogen into a 3D porous carbon matrix through template-induced edge engineering: enhanced catalytic activity towards the oxygen reduction reaction. *Journal of Materials Chemistry A*. 2017;41: 21709–21714.
- [104] Liu J, Song P, Xu W. Structure-activity relationship of doped-nitrogen (N)-based metal-free active sites on carbon for oxygen reduction reaction. *Carbon* 2017;115:763–772.
- [105] Ejaz A, Jeon S. The individual role of pyrrolic, pyridinic and graphitic nitrogen in the growth kinetics of Pd NPs on N-rGO followed by a comprehensive study. *Int J Hydrogen Energy* 2018;43:5690–5702.
- [106] Liu J, Jiao M, Mei B, Tong Y, Li Y, Ruan M, Song P, Sun G, Jiang L, Wang Y, Jiang Z. Carbon-Supported Divacancy-Anchored Platinum Single-Atom Electrocatalysts with Superhigh Pt Utilization for the Oxygen Reduction Reaction. *Angewandte Chemie*. 2019;131:1175-1189.
- [107] Zhou Y, Pasquarelli R, Holme T, Berry J, Ginley D, O’Hayre R. Improving PEM fuel cell catalyst activity and durability using nitrogen-doped carbon supports: observations from model Pt/HOPG systems. *J Mater Chem* 2009;19:7830-7841.
- [108] Zitolo A, Ranjbar-sahraie N, Mineva T, Li J, Jia Q, Stamatina S. Carbon materials for the oxygen reduction reaction. *Nat Commun* 2017;351:1–10.
- [109] Ramaprabhu BPV and S. Platinum-TM (TM = Fe, Co) alloy nanoparticles dispersed nitrogen doped (reduced graphene oxide-multiwalled carbon nanotube) hybrid structure cathode electrocatalysts for high performance PEMFC applications. *Nanoscale* 2013;5:5109–5118.
- [110] Jung WS, Popov BN. Effect of Pretreatment on Durability of fct-Structured Pt-

Based Alloy Catalyst for the Oxygen Reduction Reaction under Operating Conditions in Polymer Electrolyte Membrane Fuel Cells. *ACS Sustain Chem Eng* 2017;5:9809–9817.

- [111] Zeng J, Lee JY. Effects of preparation conditions on performance of carbon-supported nanosize Pt-Co catalysts for methanol electro-oxidation under acidic conditions. *J Power Sources* 2005;140:268–273.
- [112] Xu J, Liu X, Chen Y, Zhou Y, Lu T, Tang Y. Platinum–cobalt alloy networks for methanol oxidation electrocatalysis. *J Mater Chem* 2012;22:23659–23667.
- [113] Dubau L, Asset T, Chattot R, Bonnaud C, Vanpeene V, Nelayah J. Tuning the Performance and the Stability of Porous Hollow PtNi/C Nanostructures for the Oxygen Reduction Reaction. *ACS Catal* 2015;5:5333–5341.
- [114] Liu J, Jiao M, Lu L, Barkholtz HM, Li Y, Jiang L. High performance platinum single atom electrocatalyst for oxygen reduction reaction. *Nat Commun* 2017;8:1–9.
- [115] Mani P, Srivastava R, Strasser P. Dealloyed binary PtM₃ (M = Cu, Co, Ni) and ternary PtNi₃M (M = Cu, Co, Fe, Cr) electrocatalysts for the oxygen reduction reaction: Performance in polymer electrolyte membrane fuel cells. *J Power Sources* 2011;196:666–673.
- [116] Wang XX, Cullen DA, Pan Y, Hwang S, Wang M, Feng Z. Nitrogen-Coordinated Single Cobalt Atom Catalysts for Oxygen Reduction in Proton Exchange Membrane Fuel Cells 2018;17:1–11.
- [117] Zhou R, Zheng Y, Jaroniec M, Qiao SZ. Determination of the electron transfer number for the oxygen reduction reaction: from theory to experiment. *ACS Catalysis*. 2016;6:4720-4728.
- [118] Lin L, Zhu Q, Xu AW. Noble-metal-free Fe-N/C catalyst for highly efficient oxygen reduction reaction under both alkaline and acidic conditions. *J Am Chem Soc* 2014;136:11027–11033.
- [119] Dhanasekaran P, Williams SR, Kalpana D, Bhat SD. Boosting efficiency and stability using zirconia nanosphere-held carbon for proton exchange membrane fuel cells. *RSC Adv* 2018;8:472–480.
- [120] Liu J, Li Y, Wu Z, Ruan M, Song P, Jiang L. Pt_{0.61}Ni/C for High-Efficiency Cathode of Fuel Cells with Superhigh Platinum Utilization. *J Phys Chem C* 2018;122:14691–14697.
- [121] Choi J, Jang JH, Roh CW, Yang S, Kim J, Lim J. Gram-scale synthesis of highly active and durable octahedral PtNi nanoparticle catalysts for proton exchange

- membrane fuel cell. *Appl Catal B Environ* 2018;225:530–537.
- [122] Pan ZF, An L, Zhao TS, Tang ZK. Advances and challenges in alkaline anion exchange membrane fuel cells. *Prog Energy Combust Sci* 2018;66:141–175.
- [123] Gülzow E, Schulze M. Long-term operation of AFC electrodes with CO₂ containing gases. *J Power Sources* 2004;127:243–251.
- [124] Gülzow E. Alkaline fuel cells: a critical view. *J Power Sources* 1996;61:99–104.
- [125] Agel E, Bouet J, Fauvarque J-F. Characterization and use of anionic membranes for alkaline fuel cells. *J Power Sources* 2001;101:267–274.
- [126] Xua T, Liub Z, Yanga W. Fundamental studies of a new series of anion exchange membranes: membrane prepared from poly (2, 6-dimethyl-1, 4-phenylene oxide)(PPO) and triethylamine. *J Memb Sci* 2005;249:183–191.
- [127] Osmieri L, Zafferoni C, Wang L, Monteverde Videla AHA, Lavacchi A, Specchia S. Polypyrrole-Derived Fe–Co–N–C Catalyst for the Oxygen Reduction Reaction: Performance in Alkaline Hydrogen and Ethanol Fuel Cells. 2018;14:1954-1965.
- [128] Liu P, Liu X, Dong F, Lin Q, Tong Y, Li Y. Science of the Total Environment Electricity generation from banana peels in an alkaline fuel cell with a Cu₂O-Cu modified activated carbon cathode. *Sci Total Environ* 2018;631:849–856.
- [129] Saranya D, Selvaraj V. Double metal oxide based nickel hybrid nanocatalyst for electrooxidation and alkaline fuel cell device fabrication. *Int J Hydrogen Energy* 2018;43:13450–13461.
- [130] Mainar AR, Colmenares LC, Leonet O, Alcaide F, Iruin JJ, Weinberger S. Manganese oxide catalysts for secondary zinc air batteries: from electrocatalytic activity to bifunctional air electrode performance. *Electrochim Acta* 2016;217:80–91.
- [131] Cheng F, Zhao J, Song W, Li C, Ma H, Chen J. Facile controlled synthesis of MnO₂ nanostructures of novel shapes and their application in batteries. *Inorg Chem* 2006;45:2038–2044.
- [132] Shinozaki K, Zack JW, Richards RM, Pivovar BS, Kocha SS. Oxygen Reduction Reaction Measurements on Platinum Electrocatalysts Utilizing Rotating Disk Electrode Technique. *J Electrochem Soc* 2015;162:1144–1158.
- [133] Shi X, Iqbal N, Kunwar SS, Wahab G, Kasat HA, Kannan AM. Pt Co@NCNTs cathode catalyst using ZIF-67 for proton exchange membrane fuel cell. *Int J Hydrogen Energy* 2017:1–7.

- [134] Britton B, Holdcroft S. The Control and Effect of Pore Size Distribution in AEMFC Catalyst Layers. *J Electrochem Soc* 2016;163:353–358.
- [135] Prakash J, K Ghosh S, Sathiyamoorthy D, Venugopalan R, Paul B. Taguchi method optimization of parameters for growth of nano dimensional SiC wires by chemical vapor deposition technique. *Curr Nanosci* 2012;8:161–169.
- [136] Stock S, Cullity B. *Elements of X-RAY Diffraction*. New York: Prentice-Hall; 1956:125-169.
- [137] Iakoubovskii K, Mitsuishi K, Nakayama Y, Furuya K. Mean free path of inelastic electron scattering in elemental solids and oxides using transmission electron microscopy: Atomic number dependent oscillatory behavior. *Phys Rev B - Condens Matter Mater Phys* 2008;77:1–7.
- [138] Rask JH, Miner BA, Buseck PR. Determination of manganese oxidation states in solids by electron energy-loss spectroscopy. *Ultramicroscopy* 1987;21:321–326.
- [139] Cramer SP, Ma Y, Chen CT, Sette F, Libby E, Christou G. Ligand Field Strengths and Oxidation States from Manganese L-Edge Spectroscopy. *J Am Chem Soc* 1991;113:7937–7940.
- [140] Paterson JH, Krivanek OL. Elms of 3d transition-metal oxides. *Ultramicroscopy* 1990;32:319–325.
- [141] Rao CR, Sparrow TG, Thomas JM, Williams BG. Electronic structures of solids by electron-energy-loss spectroscopy carried out using an electron microscope: oxygen-K and metal-L edges of transition metal oxides. *Journal of the Chemical Society, Chemical Communications* 1984;18:1238-40.
- [142] Olszta MJ, Wang J, Dickey EC. Stoichiometry and valence measurements of niobium oxides using electron energy-loss spectroscopy. *J Microsc* 2006;224:233–241.
- [143] Kurata H, Colliex C. Electron-energy-loss core-edge structures in manganese oxides. *Phys Rev B* 1993;48:2102–2108.
- [144] Zhang T, Cheng F, Du J, Hu Y, Chen J. Efficiently Enhancing Oxygen Reduction Electrocatalytic Activity of MnO₂ Using Facile Hydrogenation 2015;5:1–9.
- [145] Cheng G, Xie S, Lan B, Zheng X, Ye F, Sun M, Lu X, Yu L. Phase controllable synthesis of three-dimensional star-like MnO₂ hierarchical architectures as highly efficient and stable oxygen reduction electrocatalysts. *Journal of Materials Chemistry A*. 2016;4:16462-16468.
- [146] Biesinger MC, Payne BP, Grosvenor AP, Lau LWM, Gerson AR, Smart RSC.

Resolving surface chemical states in XPS analysis of first row transition metals, oxides and hydroxides: Cr, Mn, Fe, Co and Ni. *Appl Surf Sci* 2011;257:2717–2730.

- [147] Zhang Y, Wang X, Hu D, Xue C, Wang W, Yang H. Monodisperse Ultrasmall Manganese-Doped Multimetallic Oxysulfide Nanoparticles as Highly Efficient Oxygen Reduction Electrocatalyst. *ACS Appl Mater Interfaces* 2018;10:13413–13424.
- [148] Cao YL, Yang HX, Ai XP, Xiao LF. The mechanism of oxygen reduction on MnO₂-catalyzed air cathode in alkaline solution. *J Electroanal Chem* 2003;557:127–34.
- [149] Hasan MA, Zaki MI, Pasupulety L, Kumari K. Promotion of the hydrogen peroxide decomposition activity of manganese oxide catalysts. *Appl Catal A Gen* 1999;181:171–179.
- [150] Furthmüller GK and J. Efficient iterative schemes for ab initio total-energy calculations using a plane-wave basis set. *Phys Rev B* 1996;54:11169-11186.
- [151] Kresse G, Furthmüller J. Efficiency of ab-initio total energy calculations for metals and semiconductors using a plane-wave basis set. *Comput Mater Sci* 1996;6:15–50.
- [152] Sun C, Wang Y, Zou J, Smith SC. A formation mechanism of oxygen vacancies in a MnO₂ monolayer: a DFT+ U study. *Phys Chem Chem Phys* 2011;13:11325–11338.
- [153] Krcha MD, Janik MJ. Examination of oxygen vacancy formation in Mn-doped CeO₂ (111) using DFT+ U and the hybrid functional HSE06. *Langmuir* 2013;29:10120–10131.

APPENDIX A

[EXCEL VBA CODE FOR CORRECT LSV OXYGEN DATA WITH NITROGEN
CURRENT ALONG WITH ELECTRODE NORMALIZATION TO RHE]



1.Get O-N
current.xlsm

Potential vs SCE (V) Current (mA)

	A	B	C	D	E	F	G	H	I	J	K	L	M	N	O	P
1	0.855	0.018	0.018	0.018	0.018											
2	0.854	0.016	0.016	0.016	0.016											
3	0.853	0.014	0.014	0.014	0.014											
4	0.852	0.013	0.013	0.013	0.013											
5	0.851	0.011	0.011	0.011	0.011											
6	0.850	0.009	0.009	0.009	0.009											
7	0.849	0.008	0.008	0.008	0.008											
8	0.848	0.006	0.006	0.006	0.006											
9	0.847	0.005	0.005	0.005	0.005											
10	0.846	0.003	0.003	0.003	0.003											
11	0.844	0.002	0.002	0.002	0.002											
12	0.843	0.000	0.000	0.000	0.000											
13	0.842	-0.001	-0.001	-0.001	-0.001											
14	0.842	-0.002	-0.002	-0.002	-0.002											
15	0.840	-0.003	-0.003	-0.003	-0.003											
16	0.839	-0.004	-0.004	-0.004	-0.004											
17	0.838	-0.005	-0.005	-0.005	-0.005											
18	0.838	-0.006	-0.006	-0.006	-0.006											
19	0.836	-0.007	-0.007	-0.007	-0.007											
20	0.835	-0.008	-0.008	-0.008	-0.008											
21	0.834	-0.009	-0.009	-0.009	-0.009											
22	0.833	-0.009	-0.009	-0.009	-0.009											
23	0.832	-0.010	-0.010	-0.010	-0.010											
24	0.831	-0.011	-0.011	-0.011	-0.011											

Figure 51. Nitrogen data in the “N₂” sheet.

Potential vs SCE (V) Current (mA)

	A	B	C	D	E	F	G	H	I	J	K	L	M	N
1	0.856	-0.004	-0.004	-0.003	-0.003									
2	0.855	-0.006	-0.005	-0.004	-0.004									
3	0.854	-0.007	-0.006	-0.005	-0.005									
4	0.853	-0.008	-0.007	-0.006	-0.006									
5	0.852	-0.009	-0.008	-0.007	-0.007									
6	0.850	-0.010	-0.009	-0.008	-0.008									
7	0.849	-0.010	-0.010	-0.009	-0.009									
8	0.848	-0.012	-0.011	-0.010	-0.010									
9	0.847	-0.013	-0.012	-0.011	-0.011									
10	0.846	-0.013	-0.012	-0.012	-0.012									
11	0.845	-0.014	-0.013	-0.013	-0.013									
12	0.844	-0.015	-0.014	-0.013	-0.013									
13	0.843	-0.015	-0.015	-0.014	-0.014									
14	0.842	-0.016	-0.015	-0.015	-0.015									
15	0.841	-0.017	-0.016	-0.015	-0.015									
16	0.840	-0.018	-0.017	-0.016	-0.016									
17	0.839	-0.018	-0.017	-0.017	-0.017									
18	0.838	-0.019	-0.018	-0.017	-0.017									

Figure 52. Oxygen data in the “O₂” sheet.

				Potential vs RHE (V)		Current density (mA. cm ⁻²)							
	A	B	C	D	E	F	G	H	I	J	K	L	M
1	Electrode diameter (mm)				1.155	-0.114	-0.110	-0.107	-0.109				
2		5			1.154	-0.110	-0.106	-0.103	-0.104				
3	SCE(1) Ag/AgCl(2)				1.153	-0.106	-0.103	-0.099	-0.100				
4		1			1.152	-0.103	-0.099	-0.095	-0.097				
5	pH				1.151	-0.099	-0.095	-0.091	-0.093				
6		1			1.150	-0.097	-0.093	-0.090	-0.091				
7	A(1000)/mA(1)				1.149	-0.093	-0.089	-0.086	-0.087				
8		1			1.148	-0.091	-0.086	-0.082	-0.082				
9				Calculate	1.147	-0.089	-0.085	-0.081	-0.081				
10					1.146	-0.084	-0.080	-0.076	-0.077				
11					1.144	-0.080	-0.076	-0.072	-0.072				
12					1.143	-0.077	-0.073	-0.069	-0.069				
13					1.142	-0.075	-0.071	-0.067	-0.067				
14				Clear O and N	1.142	-0.072	-0.067	-0.064	-0.064				
15					1.140	-0.070	-0.066	-0.062	-0.062				
16					1.139	-0.069	-0.064	-0.061	-0.061				
17					1.138	-0.067	-0.062	-0.059	-0.058				
18					1.138	-0.065	-0.061	-0.057	-0.057				

Figure 53. The outputs “O-N” sheet page. Fill the information on the top left (blue) and press the “calculate” button, the output data is shown on the right. The potential vs. RHE is shown in yellow and the N₂ corrected data is shown in green.

				Potential (V vs RHE)		Current density(mA.cm ⁻²)							
	A	B	C	D	E	F	G	H	I	J	K	L	M
2					0.704	-0.244	-0.234	-0.229	-0.223				
3					0.704	-0.252	-0.235	-0.236	-0.231				
4					0.702	-0.255	-0.246	-0.241	-0.235				
5					0.702	-0.264	-0.248	-0.248	-0.242				
6					0.701	-0.271	-0.261	-0.255	-0.249				
7					0.604	-1.218	-1.294	-1.353	-1.380				
8					0.604	-1.229	-1.316	-1.369	-1.399				
9					0.602	-1.232	-1.321	-1.382	-1.412				
10					0.602	-1.245	-1.346	-1.396	-1.428				
11					0.601	-1.255	-1.356	-1.411	-1.445				
12					0.504	-1.614	-2.073	-2.352	-2.592				
13					0.503	-1.618	-2.067	-2.361	-2.605				
14					0.502	-1.615	-2.087	-2.368	-2.609				
15					0.501	-1.623	-2.079	-2.374	-2.617				
16					0.500	-1.621	-2.093	-2.383	-2.626				
17					0.404	-1.762	-2.334	-2.742	-3.092				
18					0.403	-1.763	-2.339	-2.749	-3.098				

Figure 54. The outputs “n” sheet page. Those data are corrected RDE LSV data at a different potential and used to calculate the charge transfer number in APPENDIX B.

SUB O_N()

'MADE BY XUAN SHI, ANY PROBLEM CONTACT SXUAN2@ASU.EDU'

DIM ENDRPM AS INTEGER

DIM ENDDATA AS INTEGER

DIM ENDRPMO AS INTEGER

DIM ENDDATAO AS INTEGER

WITH APPLICATION

.CALCULATION = XLCALCULATIONMANUAL

.SCREENUPDATING = FALSE

.DISPLAYSTATUSBAR = FALSE

.ENABLEEVENTS = FALSE

END WITH

ENDDATA = WORKSHEETS("N2").CELLS(ROWS.COUNT, 1).END(XLUP).ROW

ENDRPM = WORKSHEETS("N2").CELLS(1,
COLUMNS.COUNT).END(XLTOLEFT).COLUMN

ENDDATAO = WORKSHEETS("O2").CELLS(ROWS.COUNT, 1).END(XLUP).ROW

ENDRPMO = WORKSHEETS("O2").CELLS(1,
COLUMNS.COUNT).END(XLTOLEFT).COLUMN

WORKSHEETS("O-N").COLUMNS(5).CLEARCONTENTS

WORKSHEETS("O-N").COLUMNS(6).CLEARCONTENTS

WORKSHEETS("O-N").COLUMNS(7).CLEARCONTENTS

WORKSHEETS("O-N").COLUMNS(8).CLEARCONTENTS

WORKSHEETS("O-N").COLUMNS(9).CLEARCONTENTS

WORKSHEETS("O-N").COLUMNS(10).CLEARCONTENTS

WORKSHEETS("O-N").COLUMNS(11).CLEARCONTENTS

WORKSHEETS("O-N").COLUMNS(12).CLEARCONTENTS

WORKSHEETS("O-N").COLUMNS(13).CLEARCONTENTS

IF ENDDATA = ENDDATAO AND ENDRPM = ENDRPMO THEN

'ELECTRODE CONVERSION-----

IF WORKSHEETS("O-N").CELLS(4, 1) = 1 THEN

FOR I2 = 1 TO ENDDATA

WORKSHEETS("O-N").CELLS(I2, 5) = WORKSHEETS("N2").CELLS(I2, 1) +
0.241 + 0.059 * WORKSHEETS("O-N").CELLS(6, 1)

WORKSHEETS("O-N").CELLS(I2, 5).INTERIOR.COLORINDEX = 6

NEXT I2

ELSEIF WORKSHEETS("O-N").CELLS(4, 1) = 2 THEN

FOR I2 = 1 TO ENDDATA

WORKSHEETS("O-N").CELLS(I2, 5) = WORKSHEETS("N2").CELLS(I2, 1) +
0.197 + 0.059 * WORKSHEETS("O-N").CELLS(6, 1)

```

    WORKSHEETS("O-N").CELLS(I2, 5).INTERIOR.COLORINDEX = 6
    NEXT I2
ELSE
    MSGBOX "PLEASE SPECIFY THE REFERENCE ELECTRODE 1 FOR SCE, 2
    FOR AG/AGCL"

END IF

```

'O2-N2-----

```

-----
    FOR I = 1 TO ENDRPM - 1
        FOR J = 1 TO ENDDATA
            WORKSHEETS("O-N").CELLS(J, 5 + I) = (WORKSHEETS("O2").CELLS(J, I +
1) - WORKSHEETS("N2").CELLS(J, I + 1)) * (1 / ((WORKSHEETS("O-N").CELLS(2,
1) / 20) ^ 2 * 3.1415926)) * (WORKSHEETS("O-N").CELLS(8, 1))
            WORKSHEETS("O-N").CELLS(J, 5 + I).INTERIOR.COLORINDEX = 4
        NEXT J

```

```

    NEXT I
ELSE
    MSGBOX "N2 AND O2 DATA SIZES ARE NOT EQUAL"

END IF

```

'O2-N2-FOR N-----

```

-----
SHEETS("N").CELLS.CLEAR

FOR I9 = 1 TO ENDDATA

    IF WORKSHEETS("O-N").CELLS(I9, 5) < 0.705 AND WORKSHEETS("O-
N").CELLS(I9, 5) > 0.7 THEN
        WORKSHEETS("O-N").ROWS(I9).COPY
        WORKSHEETS("N").ACTIVATE
        K4 = WORKSHEETS("N").CELLS(ROWS.COUNT, 5).END(XLUP).ROW
        WORKSHEETS("N").CELLS(K4 + 1, 1).SELECT
        ACTIVESHHEET.PASTE
        WORKSHEETS("O-N").ACTIVATE
    END IF
NEXT I9

FOR I8 = 1 TO ENDDATA

```

```

IF WORKSHEETS("O-N").CELLS(I8, 5) < 0.605 AND WORKSHEETS("O-
N").CELLS(I8, 5) > 0.6 THEN
WORKSHEETS("O-N").ROWS(I8).COPY
WORKSHEETS("N").ACTIVATE
K4 = WORKSHEETS("N").CELLS(ROWS.COUNT, 5).END(XLUP).ROW
WORKSHEETS("N").CELLS(K4 + 1, 1).SELECT
ACTIVESHEET.PASTE
WORKSHEETS("O-N").ACTIVATE
END IF
NEXT I8

```

```

FOR I7 = 1 TO ENDDATA

```

```

IF WORKSHEETS("O-N").CELLS(I7, 5) < 0.505 AND WORKSHEETS("O-
N").CELLS(I7, 5) > 0.5 THEN
WORKSHEETS("O-N").ROWS(I7).COPY
WORKSHEETS("N").ACTIVATE
K4 = WORKSHEETS("N").CELLS(ROWS.COUNT, 5).END(XLUP).ROW
WORKSHEETS("N").CELLS(K4 + 1, 1).SELECT
ACTIVESHEET.PASTE
WORKSHEETS("O-N").ACTIVATE
END IF
NEXT I7

```

```

FOR I3 = 1 TO ENDDATA

```

```

IF WORKSHEETS("O-N").CELLS(I3, 5) < 0.405 AND WORKSHEETS("O-
N").CELLS(I3, 5) > 0.4 THEN
WORKSHEETS("O-N").ROWS(I3).COPY
WORKSHEETS("N").ACTIVATE
K = WORKSHEETS("N").CELLS(ROWS.COUNT, 5).END(XLUP).ROW
WORKSHEETS("N").CELLS(K + 1, 1).SELECT
ACTIVESHEET.PASTE
WORKSHEETS("O-N").ACTIVATE
END IF
NEXT I3

```

```

FOR I4 = 1 TO ENDDATA

```

```

IF WORKSHEETS("O-N").CELLS(I4, 5) < 0.305 AND WORKSHEETS("O-
N").CELLS(I4, 5) > 0.3 THEN
WORKSHEETS("O-N").ROWS(I4).COPY
WORKSHEETS("N").ACTIVATE
K1 = WORKSHEETS("N").CELLS(ROWS.COUNT, 5).END(XLUP).ROW

```

```
WORKSHEETS("N").CELLS(K1 + 1, 1).SELECT
ACTIVESHEET.PASTE
WORKSHEETS("O-N").ACTIVATE
END IF
NEXT I4
```

```
FOR I5 = 1 TO ENDDATA
```

```
IF WORKSHEETS("O-N").CELLS(I5, 5) < 0.205 AND WORKSHEETS("O-
N").CELLS(I5, 5) > 0.2 THEN
WORKSHEETS("O-N").ROWS(I5).COPY
WORKSHEETS("N").ACTIVATE
K2 = WORKSHEETS("N").CELLS(ROWS.COUNT, 5).END(XLUP).ROW
WORKSHEETS("N").CELLS(K2 + 1, 1).SELECT
ACTIVESHEET.PASTE
WORKSHEETS("O-N").ACTIVATE
END IF
NEXT I5
```

```
FOR I6 = 1 TO ENDDATA
```

```
IF WORKSHEETS("O-N").CELLS(I6, 5) < 0.105 AND WORKSHEETS("O-
N").CELLS(I6, 5) > 0.1 THEN
WORKSHEETS("O-N").ROWS(I6).COPY
WORKSHEETS("N").ACTIVATE
K3 = WORKSHEETS("N").CELLS(ROWS.COUNT, 5).END(XLUP).ROW
WORKSHEETS("N").CELLS(K3 + 1, 1).SELECT
ACTIVESHEET.PASTE
WORKSHEETS("O-N").ACTIVATE
END IF
NEXT I6
```

```
WITH APPLICATION
```

```
.CALCULATION = XLCALCULATIONAUTOMATIC
.SCREENUPDATING = TRUE
.DISPLAYSTATUSBAR = TRUE
.ENABLEEVENTS = TRUE
```

```
END WITH
```

```
MSGBOX "DONE!"
```

```
END SUB
```

APPENDIX B

[EXCEL VBA CODE FOR CALCULATING CHARGE TRANSFER NUMBER]



2.Charge transfer n V2.xlsm

Potential vs SCE (V) Current density (mA. cm⁻²)

	A	B	C	D	E	F	G	H	I	J	K	L	M	
1		400	800	1200	1600	Rotating speed (RPM)								
2	0.704	-0.244	-0.234	-0.229	-0.223									
3	0.704	-0.252	-0.235	-0.236	-0.231									
4	0.702	-0.255	-0.246	-0.241	-0.235									
5	0.702	-0.264	-0.248	-0.248	-0.242									
6	0.701	-0.271	-0.261	-0.255	-0.249									
7	0.604	-1.218	-1.294	-1.353	-1.380									
8	0.604	-1.229	-1.316	-1.369	-1.399									
9	0.602	-1.232	-1.321	-1.382	-1.412									
10	0.602	-1.245	-1.346	-1.396	-1.428									
11	0.601	-1.255	-1.356	-1.411	-1.445									
12	0.504	-1.614	-2.073	-2.352	-2.592									
13	0.503	-1.618	-2.067	-2.361	-2.605									
14	0.502	-1.615	-2.087	-2.368	-2.609									
15	0.501	-1.623	-2.079	-2.374	-2.617									
16	0.500	-1.621	-2.093	-2.383	-2.626									
17	0.404	-1.762	-2.334	-2.742	-3.092									
18	0.403	-1.763	-2.339	-2.749	-3.098									

Clear data

Figure 55. The input data in “Sheet1”, rpm in the first row, the potential in the first column and current density in the light green part. The data must be corrected with N₂ current and that can be found in APPENDIX A.

Potential vs SCE (V) n

	A	B	C	D	E	F	G	H	I	J	K	L
1	diffusion coefficient cm ² s ⁻¹	viscosity cm ² s ⁻¹	O ₂ concentration (mol cm ⁻³)					0.500	2.979			
2	1.90E-05	8.93E-03	1.18E-06					0.404	2.885			
3								0.403	2.878			
4								0.402	2.867			
5								0.401	2.890			
6								0.400	2.882			
7								0.305	3.085			
8								0.304	3.119			
9								0.303	3.115			
10								0.302	3.096			
11								0.301	3.135			
12								0.205	3.351			
13								0.204	3.414			
14								0.203	3.437			
15								0.202	3.439			
16								0.201	3.478			
17								0.105	3.700			
18								0.104	3.695			
19								0.103	3.719			
20								0.102	3.728			
21								0.101	3.731			
22								0.100	3.740			

Calculate

Figure 56. The inputs in “Sheet4”, diffusion coefficient, viscosity, and oxygen concentration are being inputted in the second row. Once click the button, the potential (green) vs. charge transfer number (yellow) are shown on the right.

The screenshot shows an Excel spreadsheet with the following content:

Row 1: 9.3 Rotating Disk Electrode - 339

Row 2: The current is the flux at the electrode surface, that is,

Row 3: $i = nFA D_0 \left(\frac{C_0}{\delta} \right) \left(\frac{v}{D_0} \right)^{1/2}$ (9.3.21)

Row 4: Electrochemical method Allen Bard pg 339

Row 5: where, under the chosen current conditions, $\delta = \delta_L$. From (9.3.20) and (9.3.21), we obtain

Row 6: the Levich equation:

Row 7: $i_L = 0.62 n F A D_0^{1/2} v^{1/2} C_0$ (9.3.22)

Row 11: D v C

Row 12: 0.1M KOH

Row 13: 1.90E-05 0.01 1.20E-06 <http://www.rsc.org/suppdata/im/c1/c1jm10845i/c1jm10845i.pdf>

Row 14: 1.93E-05 0.01 1.26E-06 20C <http://www.rsc.org/suppdata/cp/c4/c4cp01337a/c4cp01337a1.pdf>

Row 15: 1.99E-05 0.01 1.20E-06 http://binarystore.wiley.com/store/10.1002/anie.201400358/asset/supinfo/anie_201400358_sm_miscellaneous_information.pdf?v=1&s=9839d23096b7d764f5932a0fe9490abc3ccd6a89

Row 16: 1.90E-05 0.01 1.20E-06 <https://pdfs.semanticscholar.org/17d7/692bb5d01f9411b30cde58934562f0c48ab.pdf>

Row 17: 1.60E-05 1.16E-02 1.31E-06 16C <http://dx.doi.org/10.1016/j.ijhydene.2014.10.088>

Row 18: 1.73E-05 0.01 1.14E-06

Row 22: D v C

Row 23: 0.5 M KOH

Row 24: 1.90E-05 0.01 0.000001 Davis R. E. et al. Electrochimica Acta. The solubility and diffusion coefficient of oxygen in KOH solutions. 1967 Vol. 12 pp. 287

Row 28: 1M KOH

Row 29: 1.40E-05 0.01 8.43E-07 25C

Row 30: 1.80E-05 0.01 7.80E-07

Row 32: 0.1M HClO4

Row 33: 1.90E-05 8.93E-03 1.18E-06 <https://pdfs.semanticscholar.org/1111/eceseeb7644a56996b7157077bc1f8bbc03.pdf>

Row 34: 1.93E-05 0.01 1.20E-06 http://binarystore.wiley.com/store/10.1002/anie.201400358/asset/supinfo/anie_201400358_sm_miscellaneous_information.pdf?v=1&s=9839d23096b7d764f5932a0fe9490abc3ccd6a89

Row 35: 2.00E-05 0.01 1.20E-06 <http://www.rsc.org/suppdata/ta/c2/c2ta01351g/c2ta01351g.pdf>

Row 36: 1.93E-05 9.87E-03 1.18E-06 <http://chen.chemistry.ucsc.edu/cs400114s.pdf>

Row 39: Table with columns: KOH Concentration (M), C_{O_2} (mol cm⁻³), D_{O_2} (cm² s⁻¹), ν (cm² s⁻¹)

KOH Concentration (M)	C_{O_2} (mol cm ⁻³)	D_{O_2} (cm ² s ⁻¹)	ν (cm ² s ⁻¹)
0.05	1.2×10^{-6}	2.0×10^{-5}	1.0×10^{-7}
0.1	1.1×10^{-6}	1.9×10^{-5}	1.0×10^{-7}
1.0	7.8×10^{-7}	1.8×10^{-5}	1.0×10^{-7}
3.0	3.0×10^{-7}	1.3×10^{-5}	1.2×10^{-7}
6.0	1.7×10^{-7}	7.5×10^{-6}	1.6×10^{-7}

Row 40: room T <http://www.electrochemsci.org/papers/vol8/80101189.pdf>

Row 45: C_{O_2} , O_2 solubility; D_{O_2} , O_2 diffusion coefficient; ν , Viscosity

Figure 57. The screenshot of showing the table of the diffusion coefficient, viscosity and oxygen concentration in the “Constant data” sheet for the different electrolyte, temperature, and concentration along with the references.

	$\omega^{-0.5}$ (rad ^{-0.5} s ^{0.5})				Inverse of current density (mA ⁻¹ cm ²)					B slope			
	A	B	C	D	E	F	G	H	I	J	K	L	M
1	0.155	0.109	0.089	0.077		4.09	4.27	4.37	4.48		-4.81		
2	0.155	0.109	0.089	0.077		3.97	4.25	4.24	4.34		-4.51		
3	0.155	0.109	0.089	0.077		3.92	4.07	4.15	4.25		-4.00		
4	0.155	0.109	0.089	0.077		3.79	4.03	4.04	4.14		-4.18		
5	0.155	0.109	0.089	0.077		3.69	3.83	3.92	4.01		-3.96		
6	0.155	0.109	0.089	0.077		0.82	0.77	0.74	0.72		1.26		
7	0.155	0.109	0.089	0.077		0.81	0.76	0.73	0.71		1.28		
8	0.155	0.109	0.089	0.077		0.81	0.76	0.72	0.71		1.34		
9	0.155	0.109	0.089	0.077		0.80	0.74	0.72	0.70		1.33		
10	0.155	0.109	0.089	0.077		0.80	0.74	0.71	0.69		1.36		
11	0.155	0.109	0.089	0.077		0.62	0.48	0.43	0.39		3.01		
12	0.155	0.109	0.089	0.077		0.62	0.48	0.42	0.38		3.01		
13	0.155	0.109	0.089	0.077		0.62	0.48	0.42	0.38		3.04		
14	0.155	0.109	0.089	0.077		0.62	0.48	0.42	0.38		3.01		
15	0.155	0.109	0.089	0.077		0.62	0.48	0.42	0.38		3.04		
16	0.155	0.109	0.089	0.077		0.57	0.43	0.36	0.32		3.14		
17	0.155	0.109	0.089	0.077		0.57	0.43	0.36	0.32		3.15		

Figure 58. The screenshot of the “Sheet2”. The $\omega^{-1/2}$ (red), the inverse of current density $1/j$ (blue) and slope (green) data can be used to do K-L plotting.

```
Sub charge_transfer_n()
'Made by Xuan Shi, if there is any problem contact sxuan2@asu.edu'
Dim endrpm As Integer
Dim enddata As Integer
Dim F As Integer
Dim T As Integer
Dim S As String
```

```
With Application
    .Calculation = xlCalculationManual
    .ScreenUpdating = False
    .DisplayStatusBar = False
    .EnableEvents = False
End With
```

```
ThisWorkbook.Sheets("Sheet2").Cells.ClearContents
Worksheets("Sheet4").Columns(8).ClearContents
Worksheets("Sheet4").Columns(9).ClearContents
Worksheets("Sheet4").Columns(10).ClearContents
Worksheets("Sheet4").Columns(11).ClearContents
Worksheets("Sheet4").Columns(12).ClearContents
Worksheets("Sheet4").Columns(13).ClearContents
```

```
Worksheets("Sheet4").Columns(14).ClearContents
```

```
enddata = Worksheets("Sheet1").Cells(Rows.Count, 1).End(xlUp).Row  
endrpm = Worksheets("Sheet1").Cells(1, Columns.Count).End(xlToLeft).Column
```

```
Worksheets("Sheet3").Cells(1, 1) = enddata 'numbers of RDE data'  
Worksheets("Sheet3").Cells(1, 2) = endrpm 'numbers of different RPM'  
i = 1  
j = 1  
k = 1  
F = 0
```

```
For k = 1 To endrpm - 1  
  If Worksheets("Sheet1").Cells(1, k + 1) = 0 Then ' Index to find if there is 0 in the  
rpm'  
    F = F - 1  
  Else: F = F + 1  
  End If  
Next k  
' calculating  $w^{-1/2}$ 
```

```
-----  
Worksheets("Sheet3").Cells(1, 3) = F
```

```
  If F <> endrpm - 1 Then  
    MsgBox "RPM contains 0"  
  Else  
    For j = 1 To enddata - 1  
      For i = 1 To endrpm - 1  
        Worksheets("Sheet2").Cells(j, i) = 1 / Sqr(Worksheets("Sheet1").Cells(1, i + 1) *  
3.1415926 * 2 / 60) 'calculate  $w^{-1/2}$ '  
      Next i  
    Next j
```

```
  End If  
' calculating 1/j
```

```
-----  
For jj = 1 To enddata - 1  
  For ii = 1 To endrpm - 1  
    If Worksheets("Sheet1").Cells(jj + 1, ii + 1) <> 0 Then  
      Worksheets("Sheet2").Cells(jj, endrpm + ii) = -1 / Worksheets("Sheet1").Cells(jj + 1,  
ii + 1) 'calculate 1/j'  
    End If  
  Next ii
```

```

Next jj
' calculating slope
'-----
-----
For jjj = 1 To enddata - 1

    X = Sheets("Sheet2").Range(Sheets("Sheet2").Cells(jjj, 1),
Sheets("Sheet2").Cells(jjj, endrpm - 1))
    Y = Sheets("Sheet2").Range(Sheets("Sheet2").Cells(jjj, endrpm + 1),
Sheets("Sheet2").Cells(jjj, endrpm + endrpm - 1))
    Worksheets("Sheet2").Cells(jjj, endrpm + endrpm + 1) =
Application.WorksheetFunction.slope(Y, X)

Next jjj
' calculating charge transfer number n
'-----
-----
For jjjj = 1 To enddata - 1

    Worksheets("Sheet3").Cells(jjjj, endrpm + endrpm + 3) = (0.62 * 1000 * 96485
* Worksheets("Sheet2").Cells(jjjj, endrpm + endrpm + 1) *
(Worksheets("Sheet4").Cells(2, 1)) ^ (2 / 3) * (Worksheets("Sheet4").Cells(2, 2)) ^ (-1 /
6) * (Worksheets("Sheet4").Cells(2, 3)

Next jjjj
Sheet4.Cells.Interior.Color = xlNone
For jjjjj = 1 To enddata - 1

    If Worksheets("Sheet3").Cells(jjjjj, endrpm + endrpm + 3) <> 0 Then
        Worksheets("Sheet4").Cells(jjjjj, endrpm + 4) = 1 / Worksheets("Sheet3").Cells(jjjjj,
endrpm + endrpm + 3)
        Worksheets("Sheet4").Cells(jjjjj, endrpm + 4).Interior.ColorIndex = 6

    End If

For j6 = 1 To enddata - 1
    Worksheets("Sheet4").Cells(j6, endrpm + 3) = Worksheets("Sheet1").Cells(j6 + 1,
1)
    Worksheets("Sheet4").Cells(j6, endrpm + 3).Interior.ColorIndex = 4

Next j6
Next jjjjj
With Application
    .Calculation = xlCalculationAutomatic
    .ScreenUpdating = True
    .DisplayStatusBar = True

```

```
.EnableEvents = True  
End With
```

```
MsgBox "done"  
End Sub
```

APPENDIX C

[EXCEL VBA CODE FOR ORGANIZING FUEL CELL DATA FOR PLOTTING]



3.Extract data for FC.xlsm

Unit	ac_hfr	fre	active	are	anode	inl	anode	sto	cathode	ir	cathode	s	current	dt	temp	ano	temp	catl	temp	catl	stack	pow	stack	voltage
Hz	cm^2	%	\$\$\$	%	\$\$\$	mAmp/cm	C	C	W	V														
0	#####	22:39.9		0	0	5	98.734	0.000	100	0.000	0	72.8	70.5	26.5	0	0.945								
10	#####	22:49.9		0	0	5	99.154	0.000	100	0.000	0	72.8	70.5	26.5	0	0.945								
20	#####	22:59.9		0	0	5	100	0.000	100	0.000	0	72.6	70.5	26.5	0	0.945								
30	#####	23:09.9		0	0	5	100	0.000	100	0.000	0	72.5	70.5	26.5	0	0.920								
40	#####	23:19.9		0	0	5	100	147.066	100	92.524	39	72.3	70.5	26.5	0.171	0.876								
50	#####	23:29.9		0	0	5	100	82.897	100	52.148	68.8	72.2	70.5	26.5	0.243	0.852								
60	#####	23:39.9		0	0	5	100	57.971	100	36.050	99	72	70.5	26.5	0.419	0.847								
70	#####	23:49.9		0	0	5	100	41.055	100	26.115	139.4	71.9	70.5	26.5	0.508	0.828								
80	#####	23:59.9		0	0	5	100	36.062	100	22.600	159	71.8	70.4	26.5	0.653	0.823								

Figure 59. The screenshot of the data (highlighted) collected from Greenlight G40 fuel cell testing machine.

Unit	ac_hfr	fre	active	are	anode	inl	anode	sto	cathode	ir	cathode	s	current	dt	temp	ano	temp	catl	temp	catl	stack	pow	stack	voltage
Hz	cm^2	%	\$\$\$	%	\$\$\$	mAmp/cm	C	C	W	V														
0	#####	29:51.4		0	0	5	100	0.0	100	0.00	0	69.7	70.2	26.5	0.000	0.945								
10	#####	30:01.4		0	0	5	100	0.0	100	0.00	0	69.8	70.2	26.5	0.000	0.945								
20	#####	30:11.4		0	0	5	100	0.0	100	0.00	0	69.7	70.1	26.5	0.000	0.945								
30	#####	30:21.4		0	0	5	100	0.0	100	0.00	0	69.8	70.1	26.5	0.000	0.940								
40	#####	30:31.4		0	0	5	100	147.7	100	92.67	39	69.8	70.1	26.5	0.171	0.876								
50	#####	30:41.4		0	0	5	100	81.6	100	51.58	70	69.8	70	26.5	0.247	0.852								
60	#####	30:51.4		0	0	5	100	57.9	100	36.33	99	69.8	70.1	26.5	0.419	0.847								
70	#####	31:01.4		0	0	5	100	41.0	100	25.75	140.2	69.8	70.1	26.5	0.490	0.833								
80	#####	31:11.4		0	0	5	100	36.1	100	22.71	159	69.7	70.1	26.5	0.658	0.828								
90	#####	31:21.4		0	0	5	100	29.0	100	18.18	198	69.6	70.1	26.5	0.800	0.808								
100	#####	31:31.4		0	0	5	100	23.4	100	14.67	246	69.8	70.1	26.5	0.976	0.793								
110	#####	31:41.4		0	0	5	100	19.3	100	12.05	297	69.8	70.2	26.5	1.164	0.784								
120	#####	31:51.4		0	0	5	100	18.0	100	11.20	319.2	69.8	70.2	26.5	1.220	0.769								
130	#####	32:01.4		0	0	5	100	16.5	100	10.30	348	69.8	70.2	26.5	1.338	0.769								
140	#####	32:11.4		0	0	5	100	14.3	100	9.08	399	69.9	70.3	26.6	1.515	0.759								
150	#####	32:21.4		0	0	5	100	12.8	100	8.07	447	69.8	70.3	26.5	1.664	0.745								
160	#####	32:31.4		0	0	5	100	11.5	100	7.27	498	69.8	70.3	26.5	1.830	0.735								
170	#####	32:41.4		0	0	5	100	10.5	100	6.63	546	69.8	70.4	26.5	1.980	0.725								
180	#####	32:51.4		0	0	5	100	9.6	100	6.07	597	69.9	70.4	26.5	2.092	0.701								
190	#####	33:01.4		0	0	5	100	8.9	100	5.59	648	70	70.5	26.5	2.223	0.686								
200	#####	33:11.4		0	0	5	100	8.8	100	5.58	648	70	70.4	26.5	2.223	0.681								
210	#####	33:21.4		0	0	5	100	8.3	100	5.14	696	69.9	70.4	26.5	2.353	0.676								
220	#####	33:31.4		0	0	5	100	7.7	100	4.82	747	69.9	70.4	26.5	2.489	0.667								
230	#####	33:41.4		0	0	5	100	7.2	100	4.53	798	69.9	70.3	26.5	2.601	0.652								
240	#####	33:51.4		0	0	5	100	6.8	100	4.25	846	70	70.3	26.5	2.716	0.642								

Figure 60. The screenshot of the data in the file “Sheet1”.

	Current density (mA.cm ⁻²)	Voltage (V)	Power density (mW.cm ⁻²)				
	A	B	C	D	E	F	G
1	0.00	0.94	0.00				
2	0.00	0.94	0.00				
3	0.00	0.94	0.00				
4	0.00	0.94	0.00				
5	39.00	0.88	34.18				
6	70.00	0.85	59.65				
7	99.00	0.85	83.87				
8	140.20	0.83	116.72				
9	159.00	0.83	131.60				
10	198.00	0.81	160.01				
11	246.00	0.79	195.20				
12	297.00	0.78	232.76				
13	319.20	0.77	245.49				
14	348.00	0.77	267.63				
15	399.00	0.76	302.96				
16	447.00	0.74	332.86				
17	498.00	0.73	365.97				
18	546.00	0.73	395.92				

Figure 61. The screenshot of the “Sheet2”. The current density, voltage and the power density are shown in yellow, green and blue, respectively.

```
Sub extract_FC_data()
```

```
Dim dataL As Integer
```

```
ThisWorkbook.Sheets("Sheet2").Cells.ClearContents
```

```
Sheet2.Cells.Interior.Color = xlNone
```

```
dataL = Worksheets("Sheet1").Cells(Rows.Count, 1).End(xlUp).Row
```

```
For i = 1 To dataL - 4
```

```
Worksheets("Sheet2").Cells(i, 1) = Worksheets("Sheet1").Cells(i + 4, 13)
```

```
Worksheets("Sheet2").Cells(i, 1).Interior.ColorIndex = 6
```

```
Next i
```

```
For i2 = 1 To dataL - 4
```

```
Worksheets("Sheet2").Cells(i2, 2) = Worksheets("Sheet1").Cells(i2 + 4, 19)
```

```
Worksheets("Sheet2").Cells(i2, 2).Interior.ColorIndex = 6
```

```
Next i2
```

```
For i3 = 1 To dataL - 4
```

```
Worksheets("Sheet2").Cells(i3, 3) = Worksheets("Sheet1").Cells(i3 + 4, 19) *
```

```
Worksheets("Sheet1").Cells(i3 + 4, 13)
```

```
Worksheets("Sheet2").Cells(i3, 3).Interior.ColorIndex = 6
```

```
Next i3
```

```
End Sub
```

APPENDIX D

[EXCEL VBA CODE FOR CALCULATING LATTICE PARAMETER FROM XRD
DATA]


 7.XRD to
 abc.xlsm

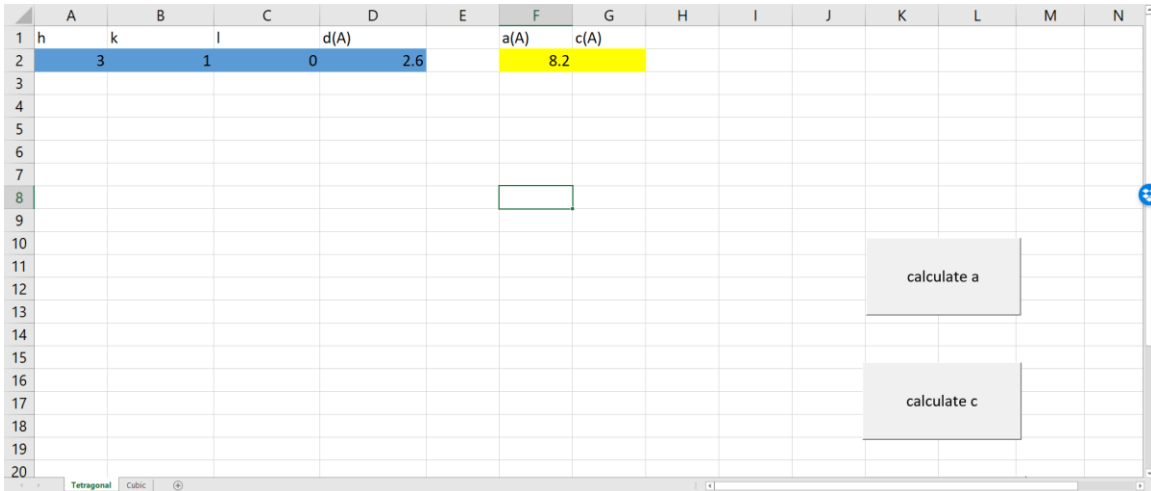


Figure 62. The screenshot of the (hkl) (with $l = 0$) plane and the d spacing information in the blue box in “Tetragonal” sheet (the information can be found in any XRD analysis software). Then press “calculate a” button to get lattice parameter a in yellow.

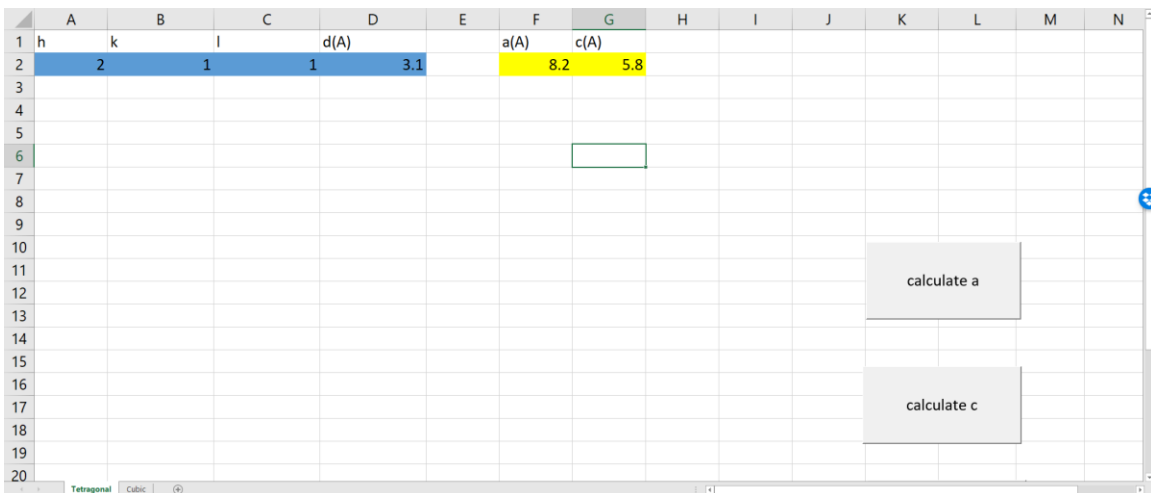


Figure 63. The screenshot of the (hkl) (with l not in 0) plane and the d spacing information in the blue box in “Tetragonal” sheet, (the information can be found in any

XRD analysis software). Then press “calculate c” button to get lattice parameter c in yellow.

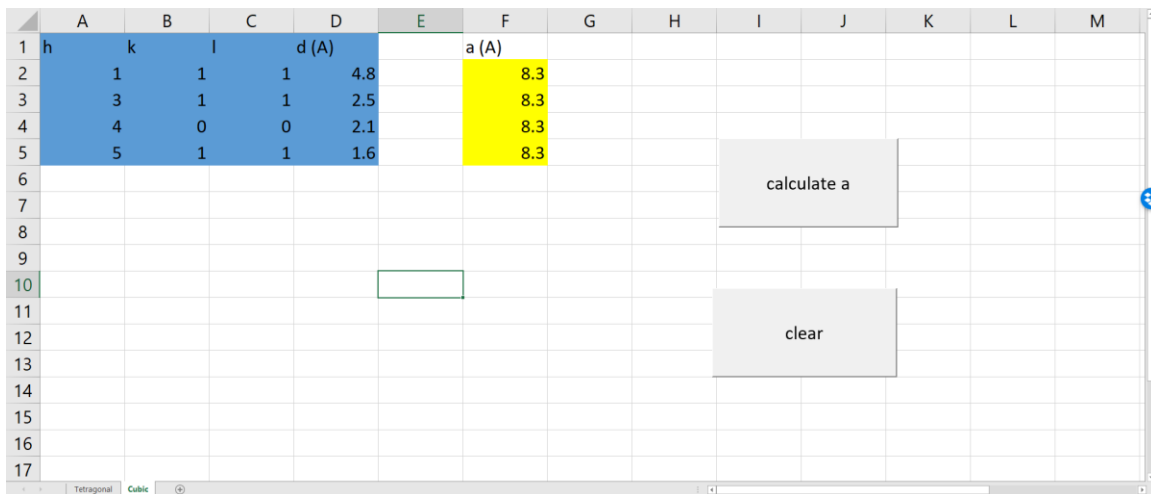


Figure 64. The screenshot of the (hkl) plane and the d spacing information in the blue box in “Cubic” sheet. Then press “calculate a” button to get lattice parameter a in yellow.

```
Sub geta()
```

```
Cells(2, 6) = Sqr((Cells(2, 1) ^ 2 + Cells(2, 2) ^ 2) * Cells(2, 4) ^ 2)
```

```
End Sub
```

```
Sub getc()
```

```
Cells(2, 7) = Sqr(1 / (1 / Cells(2, 4) ^ 2 - (Cells(2, 1) ^ 2 + Cells(2, 2) ^ 2) / Cells(2, 6) ^ 2))
```

```
End Sub
```

```
Sub a_cubic()
```

```
Dim enddata As Integer
```

```
enddata = Worksheets("Cubic").Cells(Rows.Count, 1).End(xlUp).Row
```

```
Worksheets("Cubic").Cells(1, 20) = enddata
```

```
For k = 1 To enddata - 1
```

```
Worksheets("Cubic").Cells(k + 1, 6) = Worksheets("Cubic").Cells(k + 1, 4) *
```

```
Sqr(Worksheets("Cubic").Cells(k + 1, 1) ^ 2 + Worksheets("Cubic").Cells(k + 1, 2) ^ 2 +  
Worksheets("Cubic").Cells(k + 1, 3) ^ 2)
```

```
Next k
```

End Sub

APPENDIX E

[EXCEL VBA CODE FOR CONVERSION DIFFRACTION ANGLE BETWEEN CO
AND CU X-RAY SOURCE]



8.XRD Co source to Cu source.xlsm

A	B	C	D	E	F	G	H	I	J
1	Diffraction Angle (Degrees)	Intensities (Percentage to the max)	Diffraction Angle (Degrees)	Intensities (Percentage to the max)	d(Å)				
2	50	100	58.84	100	1.8				
3									
4									
5									
6									
7									
8									
9									
10									
11									
12									
13									
14									
15									
16									
17									
18									
19									
20									
21									
22									
23									
24									

Figure 65. The screenshot of the diffraction angle and intensity from Cu α X-ray source in the file. Then press the “From Cu α to Co α ” button to get the diffraction angle, intensity and d spacing (Å) in yellow.

A	B	C	D	E	F	G	H	I	J
1	Diffraction Angle (Degrees)	Intensities (Percentage to the max)	Diffraction Angle (Degrees)	Intensities (Percentage to the max)	d(Å)				
2	58.84	100	50.00	100	1.8				
3									
4									
5									
6									
7									
8									
9									
10									
11									
12									
13									
14									
15									
16									
17									
18									
19									
20									
21									
22									
23									
24									

Figure 66. The screenshot of the diffraction angle and intensity from Co $\kappa\alpha$ X-ray source in the file. Then press the “From Co $\kappa\alpha$ to Cu $\kappa\alpha$ ” button to get the diffraction angle, intensity and d spacing (Å) in yellow.

```
Sub Co_to_Cu()
```

```
Dim enddata As Integer
```

```
enddata = Cells(Rows.Count, 1).End(xlUp).Row
```

```
For i = 1 To enddata - 1
```

```
Cells(i + 1, 6) = 1.79 / (2 * Sin(Cells(i + 1, 1) * 3.1415926 / (2 * 180)))
```

```
Cells(i + 1, 5) = Cells(i + 1, 2)
```

```
Cells(i + 1, 4) = (WorksheetFunction.Asin(1.54 / (2 * Cells(i + 1, 6))) * 180 * 2) /  
(3.1415926)
```

```
Next i
```

```
End Sub
```

```
Sub Cu_to_Co()
```

```
Dim enddata As Integer
```

```
enddata = Cells(Rows.Count, 1).End(xlUp).Row
```

```
For i = 1 To enddata - 1
```

```
Cells(i + 1, 6) = 1.54 / (2 * Sin(Cells(i + 1, 1) * 3.1415926 / (2 * 180)))
```

```
Cells(i + 1, 5) = Cells(i + 1, 2)
```

```
Cells(i + 1, 4) = (WorksheetFunction.Asin(1.79 / (2 * Cells(i + 1, 6))) * 180 * 2) /  
(3.1415926)
```

```
Next i
```

```
End Sub
```

APPENDIX F

[EXCEL VBA CODE FOR CALCULATING THE ALLOY COMPOSITION BY
VEGARD'S LAW FROM XRD DATA]



9.XRD Vegard's law.xlsm

	A	B	C	D	E	F	G	H
1	AxB(1-x) (ANGLE)	A (ANGLE)	B (ANGLE)	Cu(1) Co(2)	AxB(1-x) (d)	A (d)	B (d)	x
2	55.68	54.25	60.62	2	1.9	2.0	1.8	0.8
3	47.6	46.51	51.83		2.2	2.3	2.0	0.8
4								
5								
6								
7								
8				Calculate				
9								
10								
11								
12								
13								
14								
15								
16								
17								

Figure 67. The screenshot of the diffraction angle (2 theta degree) of $A_xB_{(1-x)}$, A and B, and X-ray source in the blue part. After clicking the “Calculate” button, the d spacing of $A_xB_{(1-x)}$, A and B, and the x percentage value are shown in the yellow box.

Sub Vegards_law()

Dim e As Integer

ee = Worksheets("Vegard's law").Cells(Rows.Count, 1).End(xlUp).Row

For k = 2 To ee

If Worksheets("Vegard's law").Cells(2, 4) = 1 Then
 Worksheets("Vegard's law").Cells(k, 5) = 1.54 / (2 * Sin(Worksheets("Vegard's law").Cells(k, 1) * 3.1415926 / (2 * 180)))
 Worksheets("Vegard's law").Cells(k, 6) = 1.54 / (2 * Sin(Worksheets("Vegard's law").Cells(k, 2) * 3.1415926 / (2 * 180)))
 Worksheets("Vegard's law").Cells(k, 7) = 1.54 / (2 * Sin(Worksheets("Vegard's law").Cells(k, 3) * 3.1415926 / (2 * 180)))


```

Worksheets("Vegard's law").Cells(k, 8) = (Worksheets("Vegard's law").Cells(k, 5) -
Worksheets("Vegard's law").Cells(k, 7)) / (Worksheets("Vegard's law").Cells(k, 6) -
Worksheets("Vegard's law").Cells(k, 7))
  ElseIf Worksheets("Vegard's law").Cells(2, 4) = 2 Then
    Worksheets("Vegard's law").Cells(k, 5) = 1.79 / (2 * Sin(Worksheets("Vegard's
law").Cells(k, 1) * 3.1415926 / (2 * 180)))
    Worksheets("Vegard's law").Cells(k, 6) = 1.79 / (2 * Sin(Worksheets("Vegard's
law").Cells(k, 2) * 3.1415926 / (2 * 180)))
    Worksheets("Vegard's law").Cells(k, 7) = 1.79 / (2 * Sin(Worksheets("Vegard's
law").Cells(k, 3) * 3.1415926 / (2 * 180)))
    Worksheets("Vegard's law").Cells(k, 8) = (Worksheets("Vegard's law").Cells(k, 5) -
Worksheets("Vegard's law").Cells(k, 7)) / (Worksheets("Vegard's law").Cells(k, 6) -
Worksheets("Vegard's law").Cells(k, 7))

  End If
Next k

End Sub

```

APPENDIX G

[EXCEL VBA CODE FOR CALCULATING THE SCHERRER CRYSTALLITE
SIZE FROM XRD DATA]



10.Scherrer.xlsm

	A	B	C	D	E	F	G	H
1	Cu(1)/Co(2)	FWHM (2 theta degrees)	Crystall size (nm)					
2	2	3.09	3.1					
3		3.69	2.6					
4		2.67	3.6					
5		2.72	3.5					
6								
7								
8								
9								
10								
11								
12								
13								
14								
15								

calculate

Figure 68. The screenshot of the X-ray source and FWHM into the blue part. After clicking the “calculate” button, the crystal sizes are shown in the yellow.

```
SUB GETPARTICLE()
```

```
  DIM ENDDATA AS INTEGER
```

```
  ENDDATA = WORKSHEETS("SIZE").CELLS(ROWS.COUNT, 2).END(XLUP).ROW
```

```
  WORKSHEETS("SIZE").CELLS(2, 6) = ENDDATA
```

```
  IF WORKSHEETS("SIZE").CELLS(2, 1) = 1 THEN
```

```
    FOR K = 1 TO ENDDATA - 1
```

```
      WORKSHEETS("SIZE").CELLS(K + 1, 3) = 0.0935 * 1.54 /  
      ((WORKSHEETS("SIZE").CELLS(K + 1, 2) * 3.1415926 / 180) *  
      COS((WORKSHEETS("SIZE").CELLS(K + 1, 2) * PI) / 360))  
    NEXT K
```

```
  ELSEIF WORKSHEETS("SIZE").CELLS(2, 1) = 2 THEN
```

```
    FOR K1 = 1 TO ENDDATA - 1
```

```
      WORKSHEETS("SIZE").CELLS(K1 + 1, 3) = 0.0935 * 1.79 /  
      ((WORKSHEETS("SIZE").CELLS(K1 + 1, 2) * 3.1415926 / 180) *  
      COS((WORKSHEETS("SIZE").CELLS(K1 + 1, 2) * PI) / 360))
```

NEXT K1

END IF

END SUB

APPENDIX H

[EXCEL VBA CODE FOR MODIFYING POSCAR FOR DFT SELECTIVE
DYNAMICS CALCULATIONS]


 5.Selective
 dynamics.xlsm

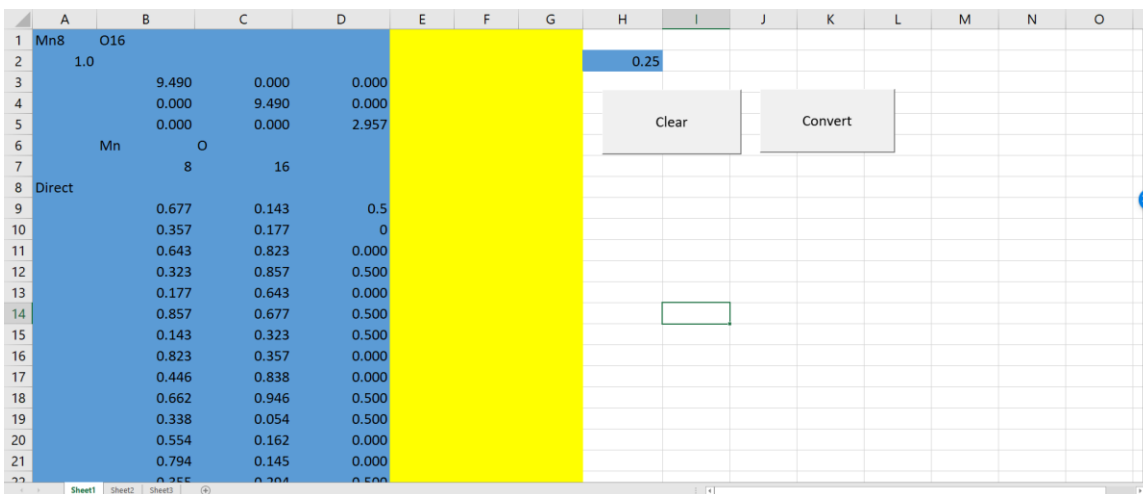


Figure 69. The screenshot of the POSCAR and threshold value in the blue part, by clicking “Convert” to process the data.

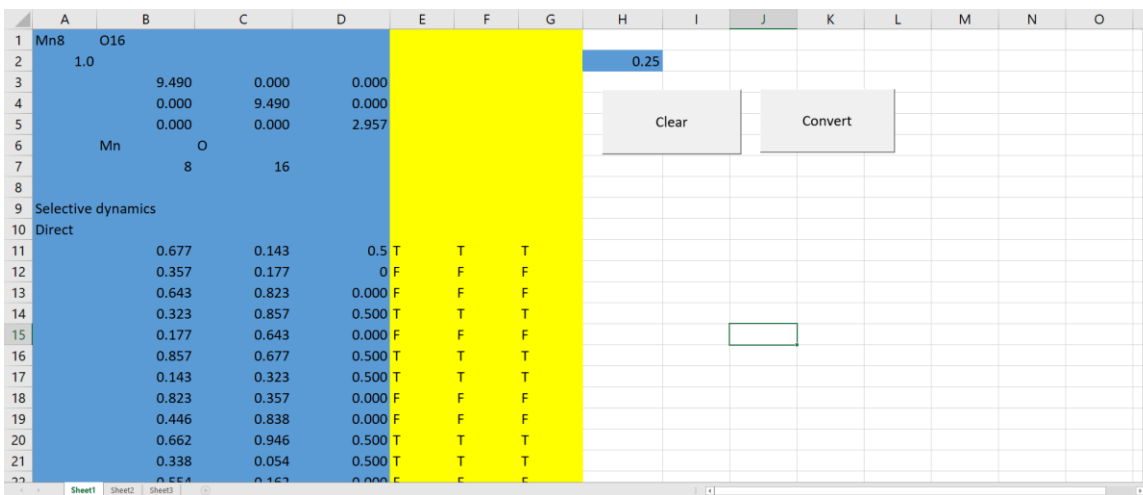


Figure 70. The screenshot of data after processed, the “selective dynamics” and the atom translatable or fixed are added. The data threshold means the set point of Z value, if the $Z > \text{threshold}$, it will be able to translate, as a label of “T”, if the $Z < \text{threshold}$, the atom will be fixed, as a label of “F”.

```

SUB SELECTIVE_DYNAMICS()

RANGE("A8:A9").ENTIREROW.INSERT
DIM LASTROW AS INTEGER
DIM HEIGHT AS INTEGER
DIM F AS STRING
DIM T AS STRING
DIM S AS STRING

'H = INPUTBOX("INPUT THE ATOM THICKNESS YOU WANT TO FIX", "ADD
HEIGHT", "TYPE IN HERE")
'HEIGHT = 0.63
'RANGE("Z1").VALUE = HEIGHT
F = "F"
T = "T"
S = "SELECTIVE DYNAMICS"
LASTROW = CELLS(ROWS.COUNT, "B").END(XLUP).ROW

FOR I = 11 TO LASTROW
IF CELLS(I, 4) < CELLS(2, 8) THEN
CELLS(I, 5) = F
CELLS(I, 6) = F
CELLS(I, 7) = F
ELSE
CELLS(I, 5) = T
CELLS(I, 6) = T
CELLS(I, 7) = T
END IF
NEXT I

CELLS(9, 1) = S

END SUB

```

APPENDIX I

[PYTHON CODE FOR BAND STRUCTURE INFORMATION FROM EIGENVAL
WITH SPIN-POLARIZED CALCULATION]


readband_spin_x
uan.py

/home/sxuan2/aMnO2/4.DOSBG_2/test_readband/				
Name	Size	Changed	Rights	Owner
..		10/26/2018 00:56:54	rxwxrwxr-x	sxuan2
EIGENVAL	437 KB	8/20/2018 11:07:01	rw-rw-r--	sxuan2
OUTCAR	948 KB	8/20/2018 11:07:02	rw-rw-r--	sxuan2
readband_xuan.py	3 KB	10/26/2018 14:36:48	rw-rw-r--	sxuan2

Figure 71. The screenshot of EIGENVAL, OUTCAR and readband_xuan.py.

```
[sxuan2@agave2:~/aMnO2/4.DOSBG_2/test_readband]$ python2 readband_xuan.py
```

Figure 72. The screenshot of the command “python2 readband_xuan.py”.

Name	Size	Changed	Rights	Owner
..		10/26/2018 00:56:54	rxwxrwxr-x	sxuan2
bandsdown.txt	124 KB	3/29/2019 12:02:15	rw-rw-r--	sxuan2
bandsup.txt	126 KB	3/29/2019 12:02:15	rw-rw-r--	sxuan2
EIGENVAL	437 KB	8/20/2018 11:07:01	rw-rw-r--	sxuan2
OUTCAR	948 KB	8/20/2018 11:07:02	rw-rw-r--	sxuan2
readband_xuan.py	3 KB	10/26/2018 14:36:48	rw-rw-r--	sxuan2

Figure 73. The screenshot of the band structure data.

```
# Xuan Modify based on Ryan Valenza's script
https://github.com/ryval/VASP/blob/master/readEIGENVAL.py
```

```
import sys
import re
import math
import numpy as np
```

```
try:
    eigenval = open("EIGENVAL", "r")
    outcar = open("OUTCAR", "r")
except IOError:
```

```

        sys.exit("Could not open EIGENVAL")

eigenval.readline() # Skip line
eigenval.readline() # N/A
eigenval.readline() # N/A
eigenval.readline() # Cartesian/Direct

# System name w/ stripped newline character
name = eigenval.readline().rstrip()
# print("System:      " + name)

first = eigenval.readline() # Possibly interesting information
(nelect, nkpts, nbands) = first.split()

#Regular expressions are used to distinguish between a k-point,
eigenvalue and fermi energy
regexs = {'kpt':
"\s+(\.d+\.\.d+E[+-]\d+)\s+(\.d+\.\.d+E[+-]\d+)\s+(\.d+\.\.d+E[+-]\d+)\s+"
,
        'enval': "\s+(\d+)\s+(-?.\d+\.\.d+)\s+(-?.\d+\.\.d+)",
        'fermi': "\s+E-fermi\s\:\s+(\d+\.\.d+)"}

#get the fermi energy from outcar
for line in outcar:
    E = re.match(regexs['fermi'], line)
    if E!= None:
        Ef=E.group(1)

kpts = []
bandsup = []
bandsdown = []
point = []
kp=[]
kp.append([0,0,0])# give the first line 0 0 0
k=0

for i in range(int(nbands)):
    bandsup.append([])
j = 0 # mark band number

for ii in range(int(nbands)):
    bandsdown.append([])
jj = 0 # mark band number
j1=0

for line in eigenval:
    kpt = re.match(regexs['kpt'], line)
    enval = re.match(regexs['enval'], line)

```

```

# print(enval)
if kpt != None:
    (kx, ky, kz) = kpt.groups(0)
    kp.append([kx,ky,kz])

if enval != None:
    e = float(enval.groups(0)[1])
    bandsup[j % int(nbands)].append([e])
    j += 1

if enval != None:
    ee = float(enval.groups(0)[2])
    bandsdown[jj % int(nbands)].append([ee])
    jj += 1

for i1 in range(int(nkpts)):
    dk=math.sqrt((float(kp[i1+1][0])-
float(kp[i1][0]))**2+(float(kp[i1+1][1])-
float(kp[i1][1]))**2+(float(kp[i1+1][2])-float(kp[i1][2]))**2)
    k=k+dk
    point.append(k)

#creat 2 matrices
up=np.zeros((int(nkpts),int(nbands)+1))
down=np.zeros((int(nkpts),int(nbands)+1))

#Convert list to array and correct Ef
uparray=np.array(bandsup)-float(Ef)
downarray=np.array(bandsdown)-float(Ef)

[up[:,0]]=[point]
[down[:,0]]=[point]

for i in range(int(nbands)):
    [up[:, i+1]]=np.transpose(uparray[i])

for ii in range(int(nbands)):
    [down[:, ii+1]]=np.transpose(downarray[ii])

with open('bandsup.txt','wb') as f_up:
    np.savetxt(f_up,up,fmt='%.6f')

with open('bandsdown.txt','wb') as f_down:
    np.savetxt(f_down,down,fmt='%.6f')

```


APPENDIX J

[PYTHON CODE FOR EXTRACT THE PROJECTED DENSITY OF STATES FROM
THE DOSCAR FILE]


**DOS_element_re
ad_Xuan.py**



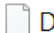
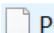
/home/sxuan2/BiVO4/5. Li static/BG_cases/2Licase_BG12_repeat/test DOS/				
Name	Size	Changed	Rights	Owner
		3/29/2019 12:07:26	rwxrwxr-x	sxuan2
 DOS_element_read_Xu...	3 KB	2/4/2019 00:14:29	rw-rw-r--	sxuan2
 DOSCAR	5,271 KB	2/11/2019 02:33:31	rw-rw-r--	sxuan2
 POSCAR	4 KB	2/11/2019 02:13:13	rw-rw-r--	sxuan2

Figure 74. The screenshot of DOS_element_read_Xuan.py, DOSCAR and POSCAR.

```
python2 DOS_element_read_Xuan.py
```

Figure 75. The screenshot of the command “python2 DOS_element_read_xuan.py” in the Putty software within the correct directory.


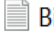
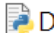
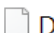
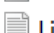

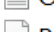
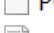
Name	Size	Changed	Rights	Owner
		3/29/2019 12:07:26	rwxrwxr-x	sxuan2
 Bi.txt	18 KB	3/29/2019 12:12:21	rw-rw-r--	sxuan2
 DOS_element_read_Xu...	3 KB	2/4/2019 00:14:29	rw-rw-r--	sxuan2
 DOSCAR	5,271 KB	2/11/2019 02:33:31	rw-rw-r--	sxuan2
 Li.txt	18 KB	3/29/2019 12:12:21	rw-rw-r--	sxuan2
 O.txt	18 KB	3/29/2019 12:12:21	rw-rw-r--	sxuan2
 POSCAR	4 KB	2/11/2019 02:13:13	rw-rw-r--	sxuan2
 V.txt	18 KB	3/29/2019 12:12:21	rw-rw-r--	sxuan2

Figure 76. The screenshot of the projected density of states.

```
# Made by Xuan 2/3/2019, this file works up to d spin orbital.
# The input files are DOSCAR and POSCAR, the output will be several
files contains integrated DOS
import sys
```

```

import re
import math
import numpy as np

try:
    doscar = open("DOSCAR", "r",)
    poscar = open("POSCAR", "r",)
except IOError:
    sys.exit("Could not open")

info5=doscar.readline() # Skip line
(Nion1, Nion2, NpDOS,NpDOS2) =info5.split()
doscar.readline() # N/A
doscar.readline() # N/A
doscar.readline() # N/A
doscar.readline() # N/A
info1=doscar.readline() # N/A
(Emax, Emin, NEDOS, Efermi, one) = info1.split()
#print(Efermi)

poscar.readline() # Skip line
poscar.readline() # Skip line
poscar.readline() # Skip line
poscar.readline() # Skip line
poscar.readline() # Skip line

info2=poscar.readline() # Skip line
info3=info2.split()
info4=poscar.readline()
info6=info4.split()

numelement=len(info3)
first=info3[0]
elename={}
elenum={}

# Separate each element and numbers of them, creat a dictionary for
future
for x in range(int(numelement)):
    elename["ele{0}".format(x)]=info3[x]
for x5 in range(int(numelement)):
    elenum["ele{0}".format(x5)]=info6[x5]

for x2 in range(int(NEDOS)+1):
    doscar.readline()

```

```

#creating empty matrix for each element, full for all the DOS data and
sum is after summation
Lfull=[]
Lsum=[]
Lfinal=[]
x9=0
for x5 in range(int(numelement)): #4element
    for x6 in range(int(elenum["ele{0}".format(x5)])): # 4 4 16 1
        Lfull.append(np.zeros((int(NEDOS), 19))) #25 full arrays and
25 sum arrays
        Lsum.append((np.zeros((int(NEDOS), 2))))
        for x7 in range(int(NEDOS)): # do 901 line by line find
information
            line1 = doscar.readline().split()
            for x8 in range(len(line1)):
                Lfull[x9][x7, x8] = float(line1[x8])
                Lsum[x9][x7, 0] = Lfull[x9][x7, 0]
                Lsum[x9][x7, 1] = np.sum(Lfull[x9][x7]) - Lfull[x9][x7, 0]
            x9+=1
            doscar.readline()

# creat a list contain all the info, x energy y integrated DOS
x12=0
for x10 in range(int(numelement)): # element 4
    Lfinal.append((np.zeros((int(NEDOS), 2))))
    for x11 in range(int(elenum["ele{0}".format(x10)])): # 4 4 16 1
        Lfinal[x10]=Lfinal[x10]+Lsum[x12]
        x12+=1

#fix the x axis value
for x13 in range(int(numelement)): # element 4
    for x14 in range(int(NEDOS)): # do 901 line by line find
information
        Lfinal[x13][x14,0]=Lsum[0][x14,0]-float(Efermi)

x15=0
#creat files for each elements
for x1 in elename:
    with open(elename[x1]+".txt",'wb') as file:
        np.savetxt(file, Lfinal[x15], fmt='%.6f')
        x15+=1

# print(elename)

```